Feary, D.A., Hine, A.C., Malone, M.J., et al., 2000
Proceedings of the Ocean Drilling Program, Initial Reports Volume 182

5. Site 1127[1]

Shipboard Scientific Party[2]

BACKGROUND AND OBJECTIVES

Site 1127 is located on the upper slope adjacent to the Eucla Shelf in 479.3 m of water (Fig. F1). It was the deepest site of a depth transect of three sites (Sites 1127, 1129, and 1131) designed to sample an impressive set of progradational sigmoidal clinoforms constituting Sequence 2 as defined by Feary and James (1998, reprinted as Chap. 2) and projected to be Pliocene–Pleistocene in age (Fig. F2). This seismic sequence forms a thin succession over the outer shelf (70–90 m), reaches peak thickness at the present shelf edge (350–550 m), and thins as a wedge farther seaward beneath the modern slope. The sequence occurs across the entire width of the Eucla Basin (~350 km), and reaches its thickest extent in the vicinity of Site 1127. This site, in conjunction with Sites 1129 and 1131, offers the opportunity to develop an in-depth understanding of shelf edge and upper slope depositional and progradational processes and to understand the extent to which complex reflection onlap and erosional truncation patterns within the clinoform package reflect hiatal or erosional episodes. Site 1127 intersected the lowest, most condensed portion of this clinoform facies as well as an expanded record of the youngest clinoforms.

Such clinoforms seem to be a signature of cool-water carbonate platforms and ramps and are undoubtedly a product of shelf-to-slope transport. However, little is known about the accumulation dynamics in relation to storm events and sea-level fluctuations. Additionally, little is known about the composition of these deposits. How much material is produced in place as compared to that transported in? Is sediment produced by enhanced biogenic production along the shelf edge, or are these clinoforms simply made up of fine-grained material produced on the shelf and swept offshore and downslope to accumulate below wave base?

F1. Map showing Site 1127 in relation to other Leg 182 sites and the AGSO169 site-survey seismic lines, p. 31.

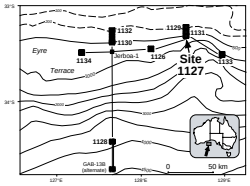

F2. Portion of seismic Line AGSO169/05a showing seismic stratigraphic sequences at Site 1127, p. 32.

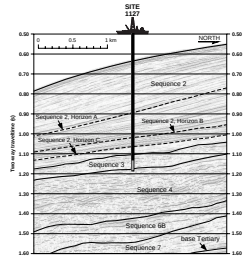

[1]Examples of how to reference the whole or part of this volume.
[2]Shipboard Scientific Party addresses.

Ms 182IR-105

In addition, seismic data indicated the presence of mounded seismic facies that have been interpreted as possible deep-water biogenic features. Although Site 1127 does not intersect any of these mound features, possible biogenic mounds located upslope may have acted as a nearby source of sediment shed downslope to Site 1127.

The principal objective along this transect of sites was to collect a detailed, high-resolution profile through an upper Neogene shelf edge (high energy) to upper slope (low energy) succession deposited within a cool-water carbonate environment to determine the response of such a depositional system to Pliocene–Pleistocene sea-level fluctuations.

Additional objectives were to

1. Obtain a high-resolution record of upper Neogene paleoceanographic variation within a middle–upper slope setting as a component of the shelf-to-basin paleoceanographic transect; and
2. Evaluate the diagenetic history of calcitic sediments deposited within a low-energy environment below storm wave base for comparison with the higher energy environments at Sites 1129 and 1131.

In addition to providing a detailed understanding of seismic Sequence 2 depositional dynamics, we also sought to recover an incomplete Sequence 3 record at Site 1127 before drilling to target depth in the upper Miocene Sequence 4.

OPERATIONS

Transit to Site 1127

The 23-nmi transit to Site 1127 was completed in 2.5 hr at 9.2 kt. A beacon was deployed at 1800 hr on 30 October, initiating operations at Site 1127. A second beacon was dropped to provide another working beacon for shallow-water operations, but it produced an erratic signal and was subsequently observed floating away, apparently self-released. A third beacon was deployed and the ship was stabilized on position.

Hole 1127A

An advanced hydraulic piston core (APC)/extended core barrel (XCB) bottom-hole assembly was run to the seafloor, and Hole 1127A was spudded at 2110 hr on 30 October, recovering 9.68 m. Core 1H was curated, but the hole was terminated because recovery was inappropriate for establishment of a good mudline. The bit was repositioned for another mudline core, ending Hole 1127A at 2130 hr on 30 October.

Hole 1127B

The ship was not moved, and Hole 1127B was spudded at 2130 hr on 30 October. The bit was positioned at 487 meters below rig floor (mbrf), and Core 1H recovered 5.86 m, which indicated a water depth of 479.3 meters below sea level (mbsl). The APC coring advanced to 148.4 meters below seafloor (mbsf), orienting Cores 3H–16H (Table T1). A noticeable odor of H_2S was detected in Core 1H. H_2S concentrations were first measured with a handheld device on Core 4H, which reached the maximum capability (2000 ppm) of the instrument. Core 6H (46.9

T1. Site 1127 coring summary, p. 69.

mbsf) had H_2S concentrations of 94,953 ppm (gas chromatography) measured from a gas void in the core (vacutainer). Coring operations were suspended for 2.5 hr while H_2S safety procedures were implemented. These procedures included prepping crews, deploying safety equipment (e.g., Scott air packs), posting notices, installing curtains and a suction hose in the laboratory cutting room, deploying fans and fixed sensors, and increasing interior laboratory ventilation. The ship heading was rotated to maintain maximum air flow over the core handling area.

Once a section was judged safe to enter the laboratories (Foss and Julson, 1993), it was run through the multisensor track (MST), split, and allowed to degas under the vacuum in the splitting room. Ten more cores were taken with little entry of cores into the laboratories. Coring was suspended again to determine an improved method for more rapid degassing of the cores. Sections were run through the MST, split, carried out to the catwalk, and opened there to allow safer and more rapid venting. When the super saw was required to cut cores, sections were split and dressed out in the splitting room and then carried outside for continued venting. The APC coring continued thereafter on a core-by-core basis. The coring rate had to be slowed to maintain proper handling and racking of the core, recharging of air packs, and cleaning and airing of core to reduce the ambient H_2S level.

Core 16H had 60 kilopounds overpull with high H_2S concentrations. Therefore, coring was switched to the XCB system for the potential reduction in gas volumes typically observed in switching to XCB coring. Cores 17X and 18X were cut from 148.4 to 164.5 mbsf with good recovery; however, H_2S readings remained ~10^5 ppm. Coring continued with the XCB from 164.5 to 510.7 mbsf (Cores 19X–55X; Table **T1**) on a core-by-core basis. Experience proved that coring more rapidly than ~45–50 min/core exceeded our capacity to process the core on the catwalk while wearing full protective gear.

The hole was prepared for logging with a wiper trip to 100 mbsf, and the bottom was tagged at 510.7 mbsf with no fill. The hole was filled with 180 bbl of sepiolite mud to protect logging tools from potential H_2S exposure, and the logging cable was coated with a 50/50 mixture of Marvel Mystery Oil and diesel. The bit was pulled up to the logging depth at 87 mbsf. The triple combination logging tool (triple combo) (without radioactive sources), Formation MicroScanner (FMS)/sonic, and geologic high-resolution magnetic tool (GHMT) logs were run to 510.7 mbsf. The well seismic tool (WST) was not required because in this thick, uniform sequence the sonic log proved to be adequate. The hole was plugged with 40 bbl of 10.5-ppg mud, and the pipe was pulled. The rig was secured for transit at 0230 hr on 3 November, ending Site 1127.

LITHOSTRATIGRAPHY

Introduction

Site 1127 is located in a water depth of 479.3 m on the eastern Eyre Terrace. The Pleistocene–Miocene (see **"Biostratigraphy,"** p. 9) succession was deposited in a prograding upper slope depositional setting. The succession is a continuation of the transect described by James et al. (1994) and part of the prograding wedge described by James and von der Borch (1991). The sequence stratigraphic framework is described in

"Seismic Stratigraphy," p. 26, and in Feary and James (1998, reprinted as Chap. 2).

Holes 1127A and 1127B intersect a 510.7-m-thick succession dominated by very fine to fine-grained, heavily bioturbated, unlithified to partially lithified, greenish gray wackestone to packstone. Three units are defined on the basis of sediment type and the presence of coarser grained beds (Figs. F3, F4).

The top part of the succession is unlithified. Partial lithification starts at 119 mbsf, and thin lithified beds occur between 170 and 200 mbsf. The beginning of lithification corresponds to a change in amplitude of seismic reflectors, from low-amplitude in the unconsolidated upper strata to high-amplitude reflectors in the partially lithified lower strata. Core recovery was good, but deformation caused by gas expansion (including extrusion of sediment from the liner on the rig floor) was common throughout the core, making it difficult to recognize fine-scale features and to identify the exact position of some depositional boundaries.

F3. Lithostratigraphic summary log, p. 33.

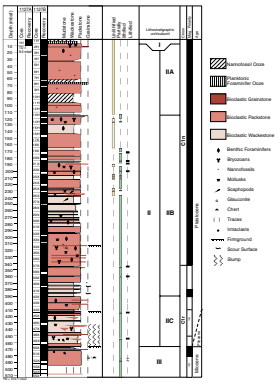

F4. High-frequency sequences showing textural and grain-size changes, p. 34.

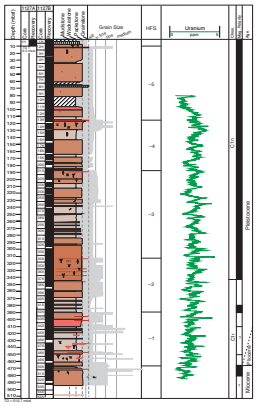

Lithostratigraphic Units

Unit I

Interval: Core 182-1127A-1H; Core 182-1127B-1H through Section 2H-3, 70 cm
Depth: 0–9.68 mbsf (Hole 1127A); 0–9.60 mbsf (Hole 1127B)
Age: Pleistocene

Unit I consists of calcareous ooze with varying amounts of nannofossils and planktonic foraminifers. It is divided into two packages: an upper nannofossil ooze and a lower foraminiferal ooze. The packages have wackestone and packstone texture, respectively, and are bioturbated and massive. The contact between packages is bioturbated and gradational, and it is associated with a downward darkening from light olive gray to pale olive.

The matrix of the unlithified nannofossil ooze package is dominated by calcareous nannofossils, mainly coccoliths, with accessory tunicate spicules, bioclasts, and sponge spicules. Components in the >63-µm fraction include abundant large planktonic foraminifers and sponge spicules, abundant bioclasts, pteropods, and rare ostracodes. Macrofossils are rare and consist of centimeter-sized pteropods. The deposits are bioturbated throughout, shown by a lighter to darker gray mottling. Burrows include *Thalassinoides* traces. Faint planar lamination is present in Section 182-1127A-1H-1, 70 cm.

The planktonic foraminiferal ooze package has a very fine to fine-grained sand size, and the color varies between pale olive gray, light gray, and olive. Color contacts are gradational. Sediments in this package are bioturbated throughout, as shown by diffuse color mottling. Calcareous nannofossils and planktonic foraminifers are common, and there are traces of quartz. Components in the >63-µm fraction are abundant planktonic foraminifers, pteropod fragments, and sponge spicules, and rare benthic foraminifers and ostracodes. Macrofossils are scarce and include gastropods, bivalves, pteropods, and bryozoans. Macrofossil abundance increases downward toward the base of the package, where there are also glauconite traces.

Unit II

Interval: Sections 182-1127B-2H-3, 70 cm, through 50X-4, 20 cm
Depth: 9.60–467.20 mbsf
Age: Pliocene–Pleistocene

Unit II is the thickest unit at Site 1127 (458.7 m), consisting of alternating bioclastic wackestone- and packstone-dominated sediment interbedded with thin grainstone beds. The contact between Units I and II is a textural and compositional boundary. Across the boundary, from Unit II to Unit I, the grain size and relative abundance of bioclasts decreases and the abundance of carbonate mud increases. The lower boundary of Unit II corresponds to a major hiatus (see "Biostratigraphy," p. 9), and the unit contact is marked by the base of a slump.

Unit II is organized into three subunits (IIA through IIC). Subunit IIA consists of nannofossil and minor foraminiferal wackestone that grades upward into bioclastic wackestone, packstone, and grainstone. Nannofossils are common throughout. Subunit IIB is characterized by alternating bioclast-rich wackestone, packstone, and grainstone. Subunit IIC has a base characterized by synsedimentary deformation, interpreted as slumps, with abundant bioclasts including bryozoans.

Subunit IIA

Interval: Sections 182-1127B-1H-3, 70 cm, through 13H-4, 76 cm
Depth: 9.60–115.59 mbsf
Age: Pleistocene

Subunit IIA consists of unlithified bioclastic packstone with minor wackestone and unlithified nannofossil wackestone with subordinate foraminiferal grainstone. The contacts between different lithologies are gradual and bioturbated. Unlithified packstone is uniformly burrowed and massive, and the overall grain size is very fine. The color is light gray to light olive gray, with gradual color transitions. The proportion of mud varies, with packstones containing less mud generally found near the top of the succession where components are coarser (fine sand size with rare grains of medium sand size). Gastropod, serpulid, other shell fragments, and benthic foraminifers constitute the dominant macrofauna. The fraction coarser than 63 µm contains dominant bioclasts and abundant benthic foraminifers. Planktonic foraminifers are common to abundant, and sponge spicules, pteropods, pollen, ostracodes, and echinoid spines are present. The mud matrix (<63 µm) consists of abundant to dominant bioclasts and nannofossils, common to present sponge and tunicate spicules and planktonic foraminifers, and rare quartz grains.

Unlithified to partially lithified bioclastic wackestone is a minor lithology that occurs near the base of the subunit. Lithification is more common in wackestone near the base of the unit. Colors are gray to light olive gray, with gradational contacts. The sediment is burrowed throughout. Burrowing is enhanced in areas of color transition by the color contrast between burrow fill and substrate and, in some cases, by packstone infilling of the burrows. Macrofauna is rare, with the exception of shell fragments accumulated in burrows. The fraction coarser than 63 µm contains dominant bioclasts, abundant to common small foraminifers and sponge spicules, and traces of tunicate spicules and organic fragments. The matrix is dominated by nannofossils, bioclasts, and sponge and tunicate spicules, together with benthic and planktonic foraminifers.

Nannofossil ooze is light olive gray, bioturbated throughout, and has a wackestone texture. Some of the burrows are filled by coarse sand-sized shell fragments. The fraction coarser than 63 µm contains dominant bioclasts and common planktonic foraminifers and sponge spicules. The matrix consists of dominant nannofossils, common bioclasts, sponge spicules, and planktonic foraminifers, as well as traces of clay.

Foraminiferal ooze is light gray in color, composed of fine to medium sand-sized grains, and has a grainstone texture. The coarser than 63-µm fraction contains abundant planktonic foraminifers and bioclasts and abundant benthic foraminifers. Echinoid spines are present. The matrix consists of abundant bioclasts, common nannofossils, sponge spicules, and planktonic foraminifers and traces of quartz, tunicate spicules, and clay. The nannofossil and foraminiferal oozes occur in the middle of the subunit between the lower wackestone and upper packstone packages.

Subunit IIB

Interval: Sections 182-1127B-13H-4, 76 cm, through 42X-3, 125 cm
Depth: 115.59–389.85 mbsf
Age: Pleistocene

The abundance of nannofossils in Subunit IIB is lower than in Subunit IIA and Unit I (see **"Site 1127 Smear Slides,"** p. 56). Bioclasts are dominant in both the matrix and >63-µm fraction. The contact between Subunits IIA and IIB (Section 13H-4, 76 cm) corresponds to a textural boundary separating muddy sediments above from grainy sediments below. The uppermost part of Subunit IIB (Sections 13H-4, 72 cm, through 14H, 64 cm) consists of 1- to 8-cm-thick alternating layers of coarse-grained grainstone and fine- to very fine grained packstone. The compositional difference between grainstone and packstone layers is the presence of more sponge spicules and foraminifers (both planktonic and benthic) in the matrix of the packstone and the presence of echinoid spines and ostracodes in the >63-µm fraction of the grainstone. The grainstone is mainly light gray, and the packstone is light olive gray. Both lithologies are bioturbated throughout.

Most of Subunit IIB is unlithified to partially lithified bioclastic packstone and wackestone. The packstone is light olive gray in color, but light gray intervals are present. The wackestone has a light gray and occasionally pale olive color. Both textures alternate, although packstone is dominant at the base and top of the subunit, and wackestone in the middle of the subunit. Macrofauna, although rare, include benthic foraminifers, shell fragments, and gastropods. Packstone and wackestone have a similar composition in the >63-µm fraction, dominated by bioclasts, abundant benthic and planktonic foraminifers, sponge spicules, ostracodes, and echinoderm spines, as well as traces of glauconite. In addition, packstone beds contain blackened grains, bryozoan fragments, opaque minerals, and pteropod fragments. Packstone and wackestone matrix is similar, with abundant bioclasts and nannofossils, common sponge and tunicate spicules, and traces of echinoderm spines. Planktonic foraminifers are abundant in wackestone and rare in packstone.

Subunit IIC

Interval: Sections 182-1127B-42X-3, 125 cm, through 50X-4, 20 cm
Depth: 389.85–467.20 mbsf

Age: Pliocene?–Pleistocene

Subunit IIC is divided into an upper package consisting of alternating partially lithified packstone and wackestone with a capping grainstone, and a lower package characterized by slumped beds. The upper unit boundary corresponds to a textural change between fine-grained fossiliferous packstone and grainstone below and the very fine grained wackestone of Subunit IIB. The lower boundary corresponds to an unconformity separating Units II and III. The mineralogy of Subunit IIC is dominated by low-Mg calcite (LMC) (see **"Inorganic Geochemistry,"** p. 19).

The lower part of Subunit IIC (Sections 47X-1 through 50X-4, 20 cm) consists of partially lithified bioclastic wackestone and packstone with abundant macrofauna (benthic foraminifers including miliolids, shell fragments, bryozoans, and gastropods), blackened grains, rotated blocks of mudstone, deformed beds, and a chaotic mixture of fine-grained packstone, coarse-grained grainstone, and mudstone. This package is interpreted to be slumped.

The upper part of Subunit IIC (Sections 42X-3, 125 cm, through 47X-1) consists of alternating packstone and wackestone, with wackestone more abundant in the lower part of the package and packstone with thin grainstone in the upper part. Contacts between the two textural types are gradational and bioturbated. The packstone is light olive gray, light gray, to gray in color, burrowed throughout, and of fine- to very fine grained sand size. Coarse components are serpulids and benthic foraminifers. The >63-µm fraction contains abundant bioclasts, common planktonic and benthic foraminifers, and sponge spicules. There are traces of bryozoans, echinoderm spines, and pollen. Thin, medium-grained, normally graded grainstone layers are intercalated with the packstone beds. A firmground overlain by rip-up clasts occurs at Section 44X-CC, 11 cm.

The wackestone is light gray and burrowed, although thin dark gray laminae are preserved occasionally. Coarse components are shell fragments and benthic foraminifers. The matrix consists of abundant nannofossils and bioclasts, sponge spicules, benthic foraminifers, and planktonic foraminifers.

Unit III

Interval: Sections 182-1127B-50X-4, 20 cm, through 55X-CC
Depth: 467.20–510.70 mbsf
Age: Miocene

Unit III has an upper boundary marked by a sharp color contact between light gray nannofossil chalk below and light greenish gray bioclastic packstone above. The surface coincides with the contact between sediments of Miocene and Pliocene?–Pleistocene age, with a possible hiatus in the record of as much as 3 m.y. (see **"Biostratigraphy,"** p. 9). This unit extends down to 510.7 mbsf, the base of the drilled interval. Unit III is divided into an upper nannofossil chalk package and a lower bioclastic packstone package characterized by the presence of glauconite and minor grainstone beds with intraclasts.

The 1.3-m-thick nannofossil chalk package contains bioclasts and grades downward into partially lithified packstone. The sediment has a wackestone to mudstone texture, is light gray in color, and is bioturbated by *Planolites* and *Chondrites* throughout. The major components of the matrix are nannofossils. Sponge spicules and planktonic and

benthic foraminifers are common. The >63-µm fraction is dominated by bioclasts, abundant planktonic foraminifers, and sponge spicules.

The bioclastic packstone package is partially lithified and poorly sorted. The main characteristics of the package are the presence of rotated intraclasts near the top of the section (Section 50X-7, 30 cm) and blackened bioclastic grains and glauconite throughout the interval. Glauconite is abundant (>50%), forming bioclastic glauconitic packstone to grainstone beds (Sections 51X-CC through 52X-1, 130 cm, and intervals 52X-2, 95–140 cm, and 52X-3, 30–105 cm). The fine to medium sand-sized glauconite is dark green to black. One of the glauconite-rich layers (Sections 51X-CC through 52X-1, 130 cm) is partially silicified. The bioclastic packstone is burrowed throughout, and the >63-µm fraction (see **"Site 1127 Thin Sections,"** p. 58) contains bioclasts, disseminated glauconite, planktonic and benthic foraminifers, and sponge spicules. The matrix consists of bioclasts and very few nannofossils. Macrofossils are rare and are represented by a few small mollusks.

Discussion

Middle Miocene Carbonates (Unit III)

The lower part of Unit III was poorly recovered; therefore, the stratigraphic development of this unit is unclear. However, the presence of grain-supported textures, blackened grains, intraclasts, and glauconite at the base suggests reworking and concentration of the coarser fraction. Benthic foraminifer data indicate faunal reworking (see **"Biostratigraphy,"** p. 9), supporting the sedimentological observation. Upward, there is an increase in planktonic fauna, and the overall unit is interpreted to represent a deepening-upward succession. The interval is sharply overlain by slumped beds and grainy and bioclastic-rich deposits of the younger Unit II after a hiatus of ~3 m.y.

The middle Miocene and lower Pliocene carbonates are equivalent to the distal portion of seismic Sequence 3 and probably contain fauna reworked from Sequence 4 (sequences after Feary and James, 1998, reprinted as **Chap. 2**).

Pleistocene Prograding Wedge (Units I and II)

The slumped interval at the base of Subunit IIC is interpreted to represent erosion and mass wasting associated with formation of the unconformity separating Units II and III, and it probably represents the base of seismic Sequence 2 (James and von der Borch, 1991; Feary and James, 1998, reprinted as **Chap. 2**) (see **"Seismic Stratigraphy,"** p. 26). Unit II formed as a prograding wedge associated with an increased influx of neritic sediment into an upper slope setting. Seismic data show a vertically stacked succession of offlapping sigmoidal reflections overlying a major discontinuity surface (see **"Seismic Stratigraphy,"** p. 26). Site 1127 intersects the distal portion of the prograding wedge.

One of the most interesting aspects of Unit II is its grain size and bioclastic composition, suggesting allochthonous off-shelf transport. There is mud as well as fine to very fine sand-sized skeletal grains. The grains (e.g., mollusk fragments and benthic foraminifers) are abraded and derived from inner to middle neritic environments (see **"Biostratigraphy,"** p. 9). Most of the grains were probably produced on the shelf and subsequently transported to the slope environment. Overall sediment

accumulation rates for Unit II are high, ranging from 130 to 400 m/m.y. (see "Biostratigraphy," p. 9, and "Paleomagnetism," p. 14). The estimated accumulation rates are similar to modern shallow-water tropical carbonates (James, 1997), indicating that thick, fine-grained, and mud-rich successions can be produced in cool-water carbonate environments in a relatively short time interval. This observation also points toward a very effective offshore transport mechanism such as "wave sweeping" and downwelling (James, 1997). Sedimentation on the slope was probably continuous throughout changes in Pleistocene sea level because of the broad ramp morphology and constant sediment production.

Unit II is characterized by cyclic variations in lithology, gamma-ray values (especially uranium) (see "Downhole Measurements," p. 23), magnetic susceptibility (MS) (see "Physical Properties," p. 21), and mineralogy (both aragonite and LMC) (see "Inorganic Geochemistry," p. 19). Based on textural and grain-size variability, Unit II is divided into five high-frequency depositional sequences (HFSs), 1 through 5, from oldest to the youngest (Fig. F4). Superimposed on the HFSs are meter-scale (higher frequency) cycles recorded by downhole measurements, MS, and mineralogy. Future detailed sedimentologic analysis will clarify the relationship between high-frequency cycles and lithologic and faunal changes. The HFS-1 sequence encompasses Subunit IIC and the lower part of Subunit IIB. The HFS-2 to HFS-4 sequences occur within Subunit IIB, and HFS-5 is equivalent to Subunit IIA. Each HFS is composed of a wackestone to packstone base, a middle part made up of wackestone, and a top dominated by packstone with thin capping grainstone. The grain size and abundance of shallow-water fauna increase near the top of each high-frequency unit sequence. The high-frequency sequences are interpreted to represent deepening followed by a shallowing-upward succession.

The thin youngest Unit I forms a drape over the older, more progradational Unit II. At the base of Unit I there is an increase in macrofossils and glauconite, and the abrupt contact with Unit II suggests that there is a condensed section or hiatus at the base of Unit I. The boundary is interpreted to represent a change in depositional style, from a progradational system with neritic-dominated fauna below to a drape system with pelagic-dominated fauna above.

BIOSTRATIGRAPHY

Introduction

Calcareous nannofossils and planktonic foraminifers indicate an expanded Pleistocene section (>415 m thick) underlain conformably by a 52-m interval that could be either Pleistocene or upper Pliocene. The Pliocene–Pleistocene unit is underlain disconformably by a relatively thin Miocene section. The lowermost core from Hole 1127B yielded lower to middle Miocene nannofossils.

Benthic foraminifers registered two assemblage changes, at ~405 mbsf and at the Pleistocene/Miocene disconformity, but indicate upper bathyal paleodepths throughout. The youngest and oldest assemblages include a redeposited neritic component. A cool temperate Pleistocene planktonic foraminifer fauna is found accompanied by warm-water species at various intervals, probably reflecting global climatic fluctuations and regional paleoceanographic variations, especially in relation to the flow of the Leeuwin Current. In the three groups of microfossils stud-

ied, the Pleistocene assemblages are characterized by concentrations of smaller forms. In the case of benthic foraminifers, this indicates sediment transport and redeposition from the shallow shelf to the upper slope.

Calcareous Nannofossils

Sediments recovered at Site 1127 are generally rich in calcareous nannofossils, except for intervals at 289–296 mbsf, 328–337 mbsf, 441.7–453 mbsf, and at 501 mbsf, where the abundance of nannofossils is greatly reduced. Preservation is moderate to good but deteriorates rapidly below the Unit II/Unit III lithostratigraphic boundary at 467–468.5 mbsf (Core 182-1127B-50X). An expanded Pleistocene section (~460 m thick) is indicated by the calcareous nannofossil assemblages recovered from the first 50 cores. A mixed assemblage immediately below the sharp lithostratigraphic contact in Core 182-1127B-50X indicates a relatively thin Miocene section.

Pleistocene

Samples 182-1127B-1H-CC, 26–29 cm (5.83 mbsf), through 17X-CC, 23–26 cm (155.20 mbsf), yielded assemblages readily assignable to the combined Zones NN21–NN20. These assemblages contain *Gephyrocapsa caribbeanica, Helicosphaera carteri, Helicosphaera hyalina, Calcidiscus leptoporus,* and small *Gephyrocapsa* spp. *Emiliania huxleyi,* the key species for Zone NN21, was identified down to Sample 182-1127A-2H-CC, 12–15 cm (15.43 mbsf).

Zone NN19 assemblages occur in Samples 182-1127B-18X-CC, 29–32 cm (162.24 mbsf), through 50X-3, 144–146 cm (466.94 mbsf). In addition to the key species *Pseudoemiliania lacunosa,* these assemblages include *Braarudosphaera bigelowii, C. leptoporus, Coccolithus pelagicus, Dictyococcites productus, H. carteri, Scyphosphaera* spp., *Reticulofenestra minutula,* and *Reticulofenestra minuta*. At several levels, the assemblages are dominated by small taxa, such as *Gephyrocapsa* spp., *R. minuta,* and *D. productus*. Small taxa were also noted for the associated benthic and planktonic foraminifers (see relevant sections below). The highest occurrence of *Helicosphaera sellii* is recorded in Sample 182-1127B-17X-CC, 23–26 cm (155.20 mbsf), and that of *Calcidiscus macintyrei* in Sample 182-1127B-38X-CC, 31–34 cm (357.16 mbsf), a depth difference of ~202 m. These two events occur at the same level at Site 1126, where the Pleistocene section is relatively condensed. The downhole appearance of *C. macintyrei* occurs at 357.16 mbsf.

The Zone NN19 assemblages from Samples 182-1127B-49X-3, 64–68 cm (456.54 mbsf), and 49X-CC, 34–37 cm (459.62 mbsf), are dominated by *B. bigelowii,* suggesting a short event marking a drastic change in surface-water conditions. Other species present in these assemblages include small *Gephyrocapsa* spp., *C. macintyrei,* and *D. productus*.

Miocene

Mixed assemblages are recorded from the highly bioturbated Samples 182-1127B-50X-4, 54–56 cm (467.54 mbsf), through 53X-CC, 23–26 cm (493.69 mbsf). These mixed assemblages suggest a middle–late Miocene age. Sample 182-1127B-50X-4, 54–56 cm (467.54 mbsf), came from below the sharp Unit II/Unit III lithostratigraphic boundary between 467 and 468.5 mbsf (see **"Lithostratigraphy,"** p. 3). This sample contains

upper Miocene taxa (probably Zone NN10), including few *Scyphosphaera* spp. and *Sphenolithus neoabies,* and rare *Discoaster bellus, Discoaster brouweri, Discoaster variabilis, Minylitha convallis,* and *Reticulofenestra pseudoumbilicus,* as well as older species such as *Calcidiscus premacintyrei.* The Miocene taxa indicate that the lithostratigraphic boundary in Core 182-1127B-50X represents a major break in sedimentation, with much of the Pliocene and a part of the upper Miocene missing.

A few pieces of chert with a calcareous "rind" recovered in the core catcher of the lowest cores, Samples 182-1127B-54X-CC, 0–1 cm (501.10 mbsf), and 55X-CC, 5–6 cm (507.75 mbsf), yielded several age-diagnostic nannofossils. In Sample 182-1127B-54X-CC, 0–1 cm (501.10 mbsf), the presence of *C. macintyrei* suggests an age younger than Zone NN5. Sample 182-1127B-55X-CC, 5–6 cm (507.75 mbsf), contains *Sphenolithus heteromorphus, Coronocyclus nitiscens, Cyclicargolithus floridanus,* and *Sphenolithus moriformis*. These nannofossils indicate the presence of combined Zones NN4 and NN5.

Planktonic Foraminifers

Planktonic foraminifers in all core-catcher samples were studied from Holes 1127A (only one core recovered) and Hole 1127B, except for Samples 182-1127B-54X-CC, 0–1 cm, and 55X-CC, 5–6 cm, that were primarily taken for nannofossil analysis. Three additional samples from Cores 182-1127B-44X and 45X were also examined. Preliminary results indicate that an extremely expanded Pleistocene sequence was recovered from Hole 1127B, extending into the upper Pliocene. The sequence unconformably overlies a thin Miocene section that contains strongly mixed planktonic foraminifer assemblages.

Pleistocene–Upper Pliocene

Samples 182-1127A-1H-CC, 23–26 cm, and 182-1127B-1H-CC, 26–29 cm, through 8H-CC, 27–29 cm, contain numerous small ostracodes, bivalves, gastropods, and sponge spicules. Planktonic foraminifers are common, forming 5%–10% of the >63-µm residue, and are beautifully preserved. The low-diversity (~10 species) assemblage is mainly composed of *Globorotalia inflata, Globorotalia truncatulinoides, Globigerina bulloides,* and *Globigerinoides ruber.* In the 63- to 150-µm fractions, *Globigerina falconensis, Globigerina quinqueloba,* and *Neogloboquadrina pachyderma* are dominant. Minor constituents include *Globigerinoides rubescens, Globigerinoides tenellus, Orbulina universa,* and *Neogloboquadrina dutertrei.* Except for having mostly small specimens, this assemblage is similar in composition to those from recent sediments in southern mid-latitudes (Bé, 1977). The first occurrence of *Globorotalia hirsuta* was detected in Sample 182-1127B-7H-CC, 24–27 cm. In the southwest Atlantic, this datum level lies within the middle Brunhes, at marine oxygen isotope Stage 12 (Pujol and Duprat, 1983). Almond et al. (1993), however, found *G. hirsuta* from marine isotope Substage 5e and younger sediments in the Great Australian Bight, suggesting that this species may have arrived in this region much later.

From Cores 182-1127B-9H through 43X, the common planktonic foraminifers are moderately to poorly preserved, especially in samples from firmgrounds. The consistent occurrence of *G. truncatulinoides* down to 404.42 mbsf (Sample 182-1127B-43X-CC, 36–39 cm) indicates Pleistocene Zone Pt1 (Fig. F5). Within this interval, the last occurrence of *Globorotalia tosaensis* in Sample 182-1127B-26X-CC, 67–70 cm, can

F5. Calcareous nannofossil and planktonic foraminifer zones, and benthic foraminifer assemblages, p. 35.

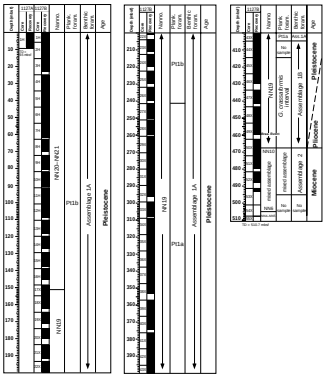

be used to define the top of Subzone Pt1a (Berggren et al., 1995). Pleistocene sediments in Hole 1127B exceed 400 mbsf.

Throughout this Pt1 interval, the planktonic foraminifer assemblage as a whole is of the southern temperate type, and only at a few levels did we observe rare specimens of (sub)tropical species. For example, *Globigerinoides sacculifer* s.l. was found in Samples 182-1127B-6H-CC, 2–4 cm; 12H-CC, 17–20 cm; and 28X-CC, 43–46 cm; and *Globorotalia tumida* in Samples 182-1127B-15H-CC, 9–12 cm; 18X-CC, 29–32 cm; 20X-CC, 12–15 cm; and 26X-CC, 67–70 cm. Samples 182-1127B-28X-CC, 43–46 cm, and 39X-CC, 22–25 cm, contain *Sphaeroidinella dehiscens* and *Pulleniatina finalis,* respectively. These typical low-latitude species signal warmer climatic conditions and/or stronger flows of the Leeuwin Current (Almond et al., 1993). The timing and duration of these events are believed to reflect global climatic cycles. A high-resolution post-cruise study of this much-expanded section will contribute to a more accurate dating of the Pleistocene cycles, as well as providing an improved understanding of regional climatic variations in the Great Australian Bight.

The occurrence of numerous small (mainly 100–180 µm) specimens from this expanded Pleistocene sequence could have resulted from preferential sorting during sediment redeposition events, so that only small specimens accumulated on this gentle slope setting. Mixing between the warmer-water dwellers, such as *G. falconensis* and *Globigerinoides rubesens,* and subantarctic representatives, especially *G. quinqueloba* and *N. pachyderma,* argues also for different sources for these sediment particles: warm species from the west via the Leeuwin Current and cold species from the southwest via the West Wind Drift. During the sorting process, a relatively cooler part of the strongly mixed upper water column may have developed, perhaps caused by upwelling, in which small tests flourished (Li et al., 1999).

In Cores 182-1127B-44X through 49X, planktonic foraminifers are characterized by many poorly preserved globorotaliids (*Globorotalia crassaformis, Globorotalia crassula,* and *Globorotalia puncticulata*), together with species that are common also in cores above (*Globorotalia inflata, Globigerina bulloides,* and *G. ruber*). This assemblage is similar to the upper Pliocene fauna of New Zealand (Hornibrook et al., 1989), but the age conflicts with nannofossils from this interval (the "*G. crassaformis* interval" in Fig. **F5**) that are characteristic of Pleistocene Zone NN19 (see **"Calcareous Nannofossils,"** p. 10). Further study of nannofossil and foraminifer datum levels is necessary to clarify the age of this interval.

Miocene

The *G. crassaformis* biofacies was succeeded downhole at 472.25 mbsf (Samples 182-1127B-50X-CC, 32–35 cm) by a moderately preserved assemblage indicating probable latest Miocene age. If the *G. crassaformis* biofacies was indeed from the Pleistocene, this faunal change should indicate a hiatus of at least 3 m.y. within Core 182-1127B-50X, at a disconformity between lithostratigraphic Units II and III (see **"Lithostratigraphy,"** p. 3). The association of *Globorotalia menardii, Globorotalia plesiotumida, G. tumida,* and *Globigerina nepenthes* indicates Subzone Pl1a, which, according to Berggren et al. (1995), is a zone straddling the Pliocene/Miocene boundary. Further downhole, typical middle–lower Miocene species are found mixed together with upper Miocene taxa in Samples 182-1127B-51X-CC, 30–33 cm; 52X-CC, 20–

23 cm; and 53X-CC, 23–26 cm (479.94–493.69 mbsf). *Jenkinsella mayeri, Globoconella conoidea,* and *Globoquadrina dehiscens* represent the middle–late Miocene; *Zeaglobigerina connecta,* the early Miocene. Also occurring are species with ranges from the upper Miocene–Pliocene, such as *Zeaglobigerina nepenthes, Zeaglobigerina woodi,* and *G. falconensis*. This mixed biofacies from an interval of ~10 m apparently indicates reworking during the middle and upper Miocene, when the sedimentation rate was markedly low (Fig. F6).

F6. Sedimentation rate curve from Site 1127 datum levels, p. 36.

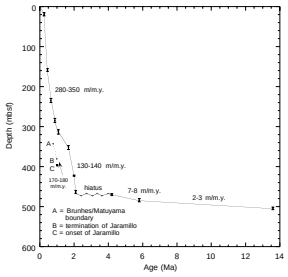

Benthic Foraminifers

Benthic foraminifers were studied from every fourth core-catcher sample at Hole 1127B. However, all core-catcher samples were studied in intervals where the benthic foraminifer assemblages showed major changes in composition (e.g., Cores 182-1127B-43X through 53X). Benthic foraminifers are generally abundant and well preserved, except toward the base of Hole 1127B (below Core 44X), where abundance fluctuates markedly and large numbers of abraded and corroded tests are found in some of the samples. Approximately 300 benthic foraminifers were picked from the >63-µm fraction, except in samples in which abundance was low. The benthic foraminifer assemblages studied include mainly calcareous taxa, and only few species and specimens of agglutinated taxa. Pleistocene, Pleistocene/Pliocene, and Miocene benthic foraminifer asssemblages are recognized in the Neogene succession of Hole 1127B.

Assemblage 1A (Pleistocene): Cores 182-1127B-1H through 44H

This Pleistocene assemblage is characterized by the common to abundant occurrence of small specimens of *Triloculina* spp., *Spiroloculina* spp., *Quinqueloculina* spp., *Elphidium* spp., *Patellina corrugata, Spirillina* spp., *Palliolatella* spp., and *Bolivina* spp. Also present as rare to few constituents of the assemblage are *Bulimina mexicana, Neolenticulina peregrina, Hoeglundina elegans, Uvigerina hispidocostata, Astrononion pusillum, Cancris* spp., *Rectuvigerina* spp., *Fissurina* spp., *Cibicides* spp., *Cibicidoides* spp., *Ehrenbergina* sp., and various nodosariids. The assemblage is strikingly dominated by small specimens of benthic foraminifers (63–150 µm). The uniformity in test size and the relative rarity of medium to large tests in many of the samples examined from this interval suggest grain-size sorting during downslope redeposition. The composition of the assemblage provides further evidence that the assemblage was partly derived from the shelf and redeposited downslope, as it includes a large proportion of shallow-water taxa (*Triloculina* spp., *Spiroloculina* spp., *Quinqueloculina* spp., *Elphidium* spp., and *Patellina* spp.), which are typically found in inner to middle neritic environments. Apparent fluctuations in the relative proportions of these neritic taxa and upper bathyal taxa such as *B. mexicana, N. peregrina, H. elegans, U. hispidocostata,* and *A. pusillum* indicate that the intensity of downslope influx probably varied in time. These fluctuations may be related to changes in climate and oceanic circulation patterns occurring on a global or regional scale during the Pleistocene (McGowran et al., 1997). Postcruise studies will be necessary to resolve the timing and scale of this cyclicity.

Assemblage 1B (Pleistocene/Pliocene): Cores 182-1127B-45H through 49X

This assemblage is characterized by occurrence of few to common *Heterolepa dutemplei, Stilostomella* spp., and *Loxostomum* spp. Also present are *B. mexicana, U. hispidocostata, Uvigerina proboscidea, Cibicidoides mundulus, Cibicidoides* spp., *Triloculina* spp., *Bolivina* spp., and various nodosariids. The composition of the assemblage indicates that the benthic foraminifers originated from an upper bathyal environment. Abundance fluctuates markedly within this assemblage, but remains generally low. There is no evidence of preferential test-size sorting within this interval. However, most samples contain a high proportion of abraded and corroded tests, suggesting extensive reworking or mixing. This is consistent with observations of slumped beds in Cores 48H to 49X and of disturbed beds in Cores 45X to 47X.

Assemblage 2 (Miocene): Cores 182-1127B-50X through 53X

This assemblage typically contains small specimens of *Bolivina* spp., *Elphidium* spp., *Loxostomum* spp., *Stilostomella* spp., *Loxostomoides* spp., *Uvigerina* spp., *Cibicidoides* spp., and *Patellina* spp., as well as various nodosariids. Abundance is generally low and preservation is poor. The uniformity in test size and the mixing of shallow-water indicators such as *Elphidium* spp. and *Patellina* spp. with upper bathyal taxa suggest that a large proportion of the tests within this assemblage originated from the shelf, before being sorted and reworked downslope. The nannofossil and planktonic foraminifer assemblages from this interval include mixed Miocene taxa, providing further evidence of reworking.

Sedimentation Rates

Sediment accumulation rates shown in Figure **F6** were calculated from preliminary biostratigraphic and paleomagnetic results from Site 1127 (see **"Paleomagnetism,"** p. 14). The biostratigraphic datum levels and relevant paleomagnetic data used to calculate sedimentation rates are listed in Table **T2.** Identification of the onset of the Jaramillo is regarded with some uncertainty (see **"Paleomagnetism,"** p. 14).

T2. Datum levels used for the graph of sedimentation rate, **p. 71.**

A very high sedimentation rate averaging 240 m/m.y. is recorded for the Pleistocene section. Paleomagnetic data indicate that accumulation in the 240–280 mbsf interval was significantly lower, at 170–180 m/m.y. Accordingly, microfossil datum levels recorded from 300 to 400 mbsf appear to be slightly displaced, probably by slumps and/or bioturbation. In contrast, the sedimentation rate for the underlying Miocene section was significantly lower, varying between 2 and 8 m/m.y. from poorly constrained datums. A major disconformity at the base of the Pleistocene section is indicated by this sharp change in sedimentation rate. Biostratigraphic data suggest that the lower Pliocene, perhaps the upper Pliocene, and part of the upper Miocene are missing. The duration of this hiatus is likely to be >3 m.y.

PALEOMAGNETISM

Shipboard paleomagnetic measurements for Holes 1127A and 1127B consisted of long-core measurements at 5-cm intervals of the natural re-

manent magnetization (NRM) and the remanence after alternating field (AF) demagnetization of 20 mT, as described in "Paleomagnetism," p. 12, in the "Explanatory Notes" chapter. Measurements were performed on archive halves of all APC and XCB cores, except for intervals affected by core disturbance consisting of reoriented biscuit and substantial interbiscuit reconstituted mud. Additional demagnetization steps up to 30 mT were applied to some cores. When orientation could be recovered, 10-cm^3 discrete samples were cut from lithified fragments from intervals where core disturbance precluded long-core measurements. Discrete samples were also collected from representative core material and were subjected to progressive AF and thermal demagnetization up to 50 mT and 250°C, respectively. These samples were also used for rock magnetic analysis.

Long-Core Measurements

The intensity of initial remanence ranges between 0.025 and 5 × 10^{-5} A/m, with a median of ~6 × 10^{-3} A/m. The highest values occur as anomalous spikes observed at the top of several cores. Unlithified packstones and wackestones that predominate above 250 mbsf are characterized by higher intensities than similar but more lithified materials below that depth. This difference is possibly caused by the interference between the magnetization of reconstituted mud and the remanence of lithified core segments in the deeper material. The NRM is of moderate to shallow negative inclination (Fig. F7), changing to shallow to moderate positive inclination at a depth of ~300 mbsf. Progressive AF demagnetization results in moderate changes in inclination and reduces considerably the scatter in both declination and inclination. Inductions of 20 mT isolate magnetizations of moderate to steep inclination from which we derived a magnetic polarity stratigraphy.

Below 250 mbsf, lower recovery and persistent core disturbance in partially lithified materials results in intervals where the measurements produce unrealistically rapid changes in inclination, with both normal and reverse polarity. This ambiguity was resolved using data from discrete samples that yield excellent data and unequivocal polarity interpretations.

Measurements on discrete samples reveal a characteristic magnetization that is isolated after removing a spurious overprint, which we interpreted as a drilling-induced remanence probably acquired during passage of the core up the drill string. Median destructive fields determined from demagnetization of discrete samples range between 25 and 30 mT, and most of the remanence (>70%) is removed after heating to 250°C. Results from Sample 182-1127B-25X-1, 135–137 cm (Fig. F8A), show a soft component with a steep downward inclination and univectorial decay to the origin above 10 mT. Thermal demagnetization of Sample 182-1127B-41X-3, 63–65 cm (Fig. F8B), shows a single-component characteristic magnetization of distributed laboratory unblocking temperatures between 90° and 250°C. Line fits were used to define the direction of the magnetization. These yield low maximum angular deviation values of <5°. The mean inclination obtained from principal component analysis of 25 samples (–51°) is indistinguishable from the overall mean determined for long-core measurements for the Brunhes epoch (–52.6°; 34 determinations from an equal number of cores). Typical standard values from averaged inclinations range from 10 to 20. The average excludes data from Core 182-1127B-11H, a pelagic ooze in which intensities varied rapidly and inclinations are anomalously low.

F7. Downhole inclination from NRM long-core measurements, Hole 1127B, p. 37.

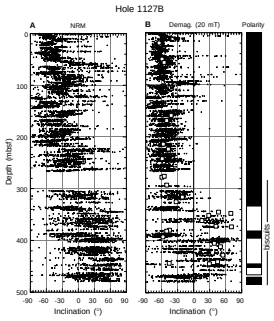

F8. Normalized intensity decay and demagnetization diagrams, p. 38.

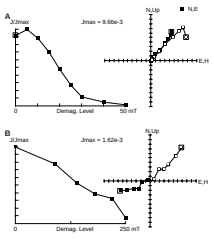

The magnetic Tensor tool was used in APC Cores 182-1127B-3H to 7H and 11H to 16H. Within-core declinations are relatively well grouped, although between-core declinations are generally scattered. After correcting azimuths using the Tensor tool, declinations center around the expected field direction. Interestingly, for XCB cores for which azimuthal orientation is not available, declinations are preferentially along the core fiducial line, an observation attributed in other paleomagnetic studies of ocean sediments to acquisition of a radially inward-directed moment during drilling (Curry et al., 1995).

Normal polarity magnetizations are persistent in Cores 182-1127B-1H through 37X. Within this normal polarity, we observed intensity fluctuations in NRM after 20-mT demagnetization, which appeared to follow the pattern of changes in relative geomagnetic field intensities determined from earlier ocean sediment records (e.g., Valet and Meynadier, 1993) (Fig. **F9**). Although these NRMs have not been normalized, there are no obvious features in the downhole susceptibility log that would account for the intensity fluctuations, and the sedimentary package is homogenous throughout the entire interval of interest except for a thin interval of pelagic ooze in part of Cores 182-1127B-10H and 11H. There are clear similarities between the virtual axial geodipole moment and NRM intensity waveforms, and a sedimentation rate of ~400 m/m.y. is generally consistent with the periodicity of the oscillations observed in the composite paleointensity record.

Moderately to steeply positive inclinations in Section 182-1127B-37X-4 (343.4 mbsf) are interpreted as reversed magnetizations. A magnetostratigraphy was based upon this reversal and extended downhole. Below 400 mbsf, data are of lesser quality, although polarity interpretations derived from discrete samples are unambiguous. The quality of the record improved toward the bottom of the hole, where a normal-to-reverse transition is recorded at 467.2 mbsf.

F9. Long-core measurements, **p. 39.**

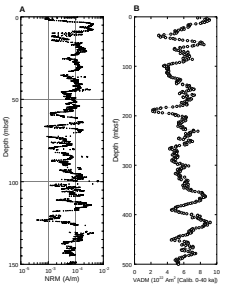

Rock Magnetism

Rock magnetism analysis consisted of measurements of weak-field susceptibility at two frequencies, progressive isothermal remanent magnetization (IRM) acquisition, and AF demagnetization of anhysteretic remanent magnetization (ARM). Decay of the NRM upon AF demagnetization is typical of single-domain magnetite, although laboratory unblocking temperatures are low (<300°C). This behavior, however, is typically observed in magnetic sulfides. Four representative samples were given a 300-mT IRM and subsequently measured over a period of three days. All samples displayed a systematic decrease in saturation isothermal remanent magnetization (SIRM). The SIRM decrease after 48 hr was ~30%, although one specimen from Core 182-1127B-18X lost as much as 60% of the initial IRM during that time. This decay is not associated with viscous decay of a magnetization in grains near the superparamagnetic single-domain threshold, because the same saturation field was used before each measurement. Furthermore, viscous decay at rapid time scales (10–10^4 s) was not observed, and susceptibility displayed only a weak frequency dependence. We attribute this "vanishing magnetization" to the oxidation of a metastable phase such as greigite, which is consistent with the low unblocking temperature and relatively high coercivity observed.

Rock magnetic results are presented in the form of modified Cisowski plots (Cisowski, 1981). In these plots (Fig. **F10**) the acquisition of IRM, and the demagnetization of NRM, ARM, and IRM are shown in absolute

F10. Plots of AF demagnetization of NRM, ARM, and IRM and of the acquisition of IRM, **p. 40.**

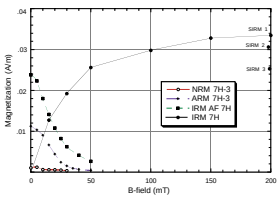

values. The NRM systematically demagnetizes above the noise level of the instrument; all samples display high ARM:IRM ratios that suggest a single-domain grain size.

Magnetostratigraphy

The normal polarity magnetizations persistent in Cores 182-1127B-1H through 37X are interpreted to be the Brunhes, with the top of the Matuyama epoch (Chron C1r1r) (Fig. F7) corresponding to the positive inclinations in Core 182-1127B-37X at 343.4 mbsf. The top of Chron C1r1n (Jaramillo) is observed at 380.7 mbsf, and the base lies between 393 and 395 mbsf. If the intensity variations within the Brunhes are correlated with the estimates of variation in the mean dipole moment of the geomagnetic field for the same period, a higher resolution magnetostratigraphy becomes possible for this period of time. The more obvious peaks in the record would then provide an approximate time–depth relationship. The low in the NRM record at 10–14 mbsf then corresponds to the low centered at ~20,000 yr (Mono Lake excursion) in the magnetic field record. Similarly, the double peak between 60 and 70 mbsf corresponds to 220,000 to 250,000 yr, and the broad high with three peaks at 90 to 120 mbsf then corresponds to the field intensity feature between 320,000 and 400,000 yr.

ORGANIC GEOCHEMISTRY

At Site 1127, in addition to routine monitoring of hydrocarbon and hydrogen sulfide (H_2S) gases for safety, analyses were conducted for inorganic carbon, total carbon, nitrogen, and sulfur. The analytical procedures are described in "Organic Geochemistry," p. 16, in the "Explanatory Notes" chapter.

Volatile Hydrocarbons and Hydrogen Sulfide

Concentrations of volatile hydrocarbons and H_2S were routinely determined from every core in Hole 1127B using standard ODP headspace or vacutainer sampling procedures. The striking results from Hole 1127B are the very high concentrations of methane (C_1) and H_2S throughout most of the section (Tables T3, T4). Gas pockets occurred commonly from 47 to 312 mbsf. These pockets were sampled directly through the core liner using a gas-tight syringe (vacutainer). Methane concentrations in these gas pockets range from 329,045 to 585,009 ppm (Fig. F11). Although concentrations of C_1 are high compared to those from most previous ODP sites, methane concentrations exceeding 880,000 ppm have been reported for Sites 892, 994, and 996 (Westbrook, Carson, Musgrave, et al., 1994; Paull, Matsumoto, Wallace, et al., 1996).

Methane occurs at lower and variable concentrations in the headspace samples, with the lowest values at the tops and bottoms of the sedimentary sections (Fig. F12). From 20 to 80 mbsf, methane increases to 46,234 ppm, the highest value observed, and then decreases sharply to values between 885 and 3254 ppm from 96 to 169 mbsf. Between 169 to 304 mbsf, methane increases to 18,328 ppm. Below 304 mbsf, methane shows a general but variable decrease to <400 ppm. The bimodal C_1 headspace profile vs. depth apparently tracks organic carbon

T3. Composition of gases, Hole 1127B, p. 72.

T4. Headspace gas composition, Hole 1127B, p. 73.

F11. Vacutainer gas concentrations from Hole 1127B, p. 41.

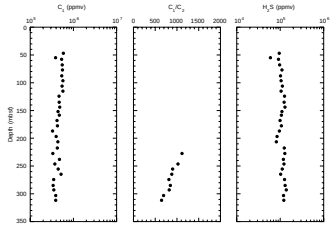

F12. Headspace gas concentrations from Hole 1127B, p. 42.

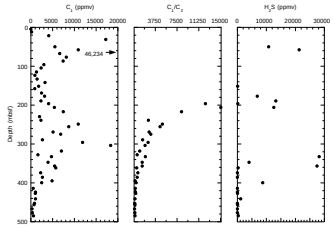

(C_{org}) values. Low C_1 concentrations between 100 and 200 mbsf and higher values from 200 to 350 mbsf correlate to comparable patterns of C_{org} concentration in the same depth intervals (see "Inorganic and Organic Carbon, Sulfur, and Nitrogen," p. 18).

Ethane (C_2) appears at depths below 227 mbsf at concentrations as high as 605 ppm in vacutainer samples and as high as 17.6 ppm in headspace samples (Figs. F11, F12). The C_1/C_2 ratio in vacutainer samples decrease from 1116 to 644; in headspace samples, the ratio decreases to a value of 82. Although the latter ratio is in the range indicative of thermogenic hydrocarbon sources, the concentrations of both C_1 and C_2 in the deeper section are too low to be of safety concern.

Heavier hydrocarbon gases (C_{3+}) were detected in the headspace samples from 124 mbsf down to the deepest gas pocket occurrence at 311.6 mbsf and from 196.4 mbsf down to the base of the hole (except for one shallow sample at 67.4 mbsf). In addition, three unknown peaks appeared at approximate concentrations of 50–100 ppmv on the flame ionization detector gas chromatogram at the following retention times: (1) peak 1–4.67 min, following *n*-C_4; (2) peak 2–6.07 min, between *i*-C_5 and *n*-C_5; and (3) peak 3–7.17 min, between *n*-C_5 and *i*-C_6. Reference standards were not available to ascertain the identity of these compounds.

Concentrations of H_2S in the gas pockets range from 60,000 to 138,000 ppm, possibly the highest level found at any ODP site (Fig. F11). The maximum H_2S concentration found at any previous site is ~100,000 ppm at Site 1005 (Eberli, Swart, Malone, et al., 1997). The concentrations of H_2S in headspace samples are much lower and highly variable, ranging from below detection in the deepest intervals to as high as 28,218 ppm at ~350 mbsf (Fig. F12).

Inorganic and Organic Carbon, Sulfur, and Nitrogen

Inorganic carbon concentrations were converted to calcium carbonate percentages (see "Organic Geochemistry," p. 16, in the "Explanatory Notes" chapter). Throughout Hole 1127B, carbonate values range primarily from 85 to 92 wt% (Table T5; Fig. F13). From the sediment surface to ~340 mbsf, except for sporadic lower values, the carbonate content is toward the higher end of the range (88–92 wt%). Below 340 mbsf, carbonate values are toward the lower end of the range (85–89 wt%).

Organic carbon reaches values as high as 1.15 wt% (Fig. F13). From the surface to a depth of ~240 mbsf, C_{org} values are primarily <0.5 wt%. In the interval from 240 to 360 mbsf, C_{org} ranges between 0.5 and 1.1 wt%. Concentrations of methane in this interval are also relatively high, apparently related to the higher C_{org} content. Below 360 mbsf, C_{org} values again are generally <0.5 wt%. Because of the generally low organic carbon content in Hole 1127B, no samples were analyzed for Rock-Eval parameters.

Nitrogen content reaches a maximum concentration of 0.14 wt%, although most samples have <0.1 wt%. Sulfur concentrations peak at 0.43 wt%, and most samples have no measurable sulfur. Sulfur concentrations are highest (0.1–0.43 wt%) between 250 and 320 mbsf, the same interval having the highest C_{org} content (Table T5).

T5. C, N, and S data, Hole 1127B, p. 74.

F13. $CaCO_3$ and C_{org} contents in samples from Hole 1127B, p. 43.

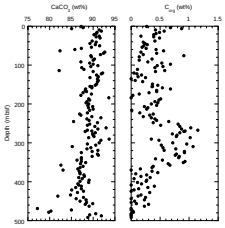

INORGANIC GEOCHEMISTRY

Interstitial Waters

Interstitial water samples of Hole 1127B were taken at a rate of two per core for the first five cores and one per core thereafter. Samples were analyzed according to the procedures outlined in "Inorganic Geochemistry," p. 18, in the "Explanatory Notes" chapter. The data are presented in Table T6 and Figures F14, F15, F16, F17, and F18.

T6. Interstitial water geochemistry measurements, p. 77.

Salinity and Chlorinity

Salinity shows a linear increase from 34, reaching 88 by 239.3 mbsf. From 239.3 to 335.5 mbsf, salinity values are variable; below 335.5 mbsf, the values become more stable and reach a maximum of 96 (Fig. F14). Despite procedures taken to eliminate H_2S from the samples (see "Inorganic Geochemistry," p. 18, in the "Explanatory Notes" chapter), determination of chlorinity at this site was hampered by the high concentration of H_2S, which interfered with the endpoint determination of the titration. However, as Cl^- was also determined using an ion chromatograph, we used the Cl^- data measured by ion chromatography for interpretative purposes.

F14. Concentration depth profiles of salinity and chlorinity at Hole 1127B, p. 44.

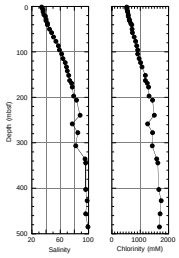

Calcium, Magnesium, Potassium, Lithium, Silica, and Strontium

Concentrations of Ca^{2+} and Mg^{2+} decrease with depth from 11.3 and 54.6 mM, respectively, to 3.5 and 26.4 mM at a depth of 114.7 mbsf (Fig. F15). Below this depth, both elements show a steady increase in concentration, reaching values of 41.2 and 105.0 mM at 484.6 mbsf. The values of K^+ show a steady increase, reaching a maximum at 427.4 mbsf. The concentrations of Li^+ increase steadily from 36 to 590 µM at 484.6 mbsf, although the increase appears to have three distinct slopes (0–40, 40–200, and 200–482 mbsf). Silica increases more than threefold from 191 to 672 µM within the first 12 m of Hole 1127B and thereafter increases slowly, reaching a maximum of 970 µM at 104.54 mbsf. Below this depth, the values remain almost constant at a level of 900 µM. The concentration of Sr^{2+} increases slowly from 73 to 200 µM at 151.8 mbsf. Below this depth, Sr^{2+} exhibits a marked increase to as much as 700 µM at 258.5 mbsf.

F15. Concentration depth profiles for Hole 1127B, p. 45.

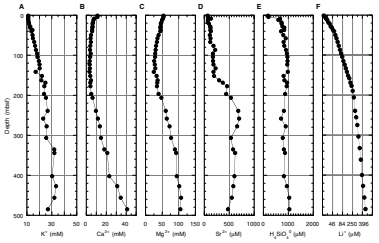

Ammonium, Phosphate, Sulfate, Alkalinity, and pH

The concentration of NH_4^+ increases in the upper part of Hole 1127B, from 0.5 mM to 18.5 mM at 67.3 mbsf, and then remains constant (with the exception of a distinct peak between 150 and 200 mbsf) until 280 mbsf (Fig. F16). Below this depth, the NH_4^+ concentration steadily decreases to 5 mM at 481.7 mbsf. The phosphate data are very erratic and could have become contaminated during sample handling. However, in general, there is a constant increase in phosphate concentration to a maximum of 134.0 µM at 104.5 mbsf, followed by a decrease in concentration to values averaging 22 µM between 300 and 460 mbsf. The concentration of SO_4^{2-} decreases from 30.4 mM to the detection limit within the upper 20 mbsf. Variable amounts of SO_4^{2-} evident between 21.4 and 168.9 mbsf are probably a result of core contamination

F16. Concentration depth profiles for Hole 1127B, p. 46.

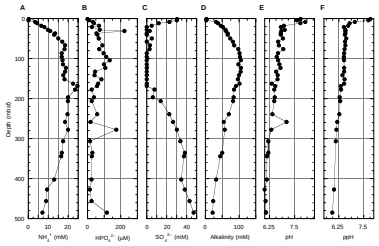

during retrieval by surface seawater circulated during drilling. Below 177.5 mbsf, the concentration of SO_4^{2-} increases again, reaching 47.1 mM at 484.6 mbsf. Alkalinity increases rapidly from 3.3 to 31.7 mM between 4.5 and 8.9 mbsf. Below this depth, alkalinity displays a linear increase to 100 mM at 100 mbsf. Below 160 mbsf, alkalinity slowly decreases to 22 mM at 484.6 mbsf. The pH measured using the punch-in electrode (ppH) shows a rapid initial decrease within the first 20 mbsf from 7.83 to 6.79. Below this depth, the values decrease linearly to a pH of 5.92 at 481.7 mbsf.

Discussion

Pore-water chemistry at Site 1127 is dominated by an extended sulfate reduction zone that produces large amounts of H_2S and HCO_3^-. As was the case with Site 1126 (see **"Inorganic Geochemistry,"** p. 30, in the "Site 1126" chapter), the interstitial waters at Site 1127 show a salinity increase of as much as ~100 in sediments of Pliocene age. However, as a result of the much thicker Pleistocene at Site 1127 (see **"Biostratigraphy,"** p. 9), the supplying brine occurs at greater depths; thus, the salinity values increase more slowly.

The presence of the brine affected the interstitial water chemistry of Site 1127 in several ways. The most readily perceivable effect was an intense smell of H_2S. Concentrations reached 138,026 ppm in gas voids sampled from Core 182-1127B-32X (see **"Organic Geochemistry,"** p. 17). H_2S originates as a by-product of the decomposition of organic matter under conditions in which sulfate is used as a terminal electron acceptor. Production of H_2S ceases with increasing depth as a result of the exhaustion of either SO_4^{2-} or organic material. Below the sulfate reduction zone, CO_2 is used as an oxidant and methanogenesis is the most common method of breakdown of organic material (see **"Organic Geochemistry,"** p. 17). At Site 1127, the extent of the sulfate reduction zone is enhanced by the presence of high-salinity pore fluids located in deeper strata that possess SO_4^{2-} concentrations higher than those of normal seawater (Fig. **F17**). As a result of the high SO_4^{2-} concentration in the underlying pore waters, the concentration gradient is larger than for normal seawater. Because of the relatively low iron content of the sediment, most of the H_2S does not react to form iron sulfides and freely diffuses out of the sulfate reduction zone.

The process of sulfate reduction produces two moles of alkalinity for every mole of sulfate reduced, and, simplistically, a 2:1 relationship could be expected between alkalinity and sulfate. Although this is approximately the relationship observed (Fig. **F18**), it does not take into consideration the ~40 mM of Mg^{2+} and 8 mM of Ca^{2+} lost from the pore fluids, which would consume 96 mM of alkalinity if precipitated as either LMC or dolomite according to the following equations:

$$Ca^{2+} + CO_3^{2-} \Leftrightarrow CaCO_3(s) \text{ and}$$

$$Ca^{2+} + Mg^{2+} + 2CO_3^{2-} \Leftrightarrow CaMg(CO_3)_2(s).$$

A possible explanation for the alkalinity anomaly is that part of the consumption of Mg^{2+} arises from the alteration of clay minerals, although this process usually increases the concentration of Ca^{2+}, which was not observed at Site 1127. However, alkalinity can also be produced

F17. Concentration depth profiles for Hole 1127B, **p. 47.**

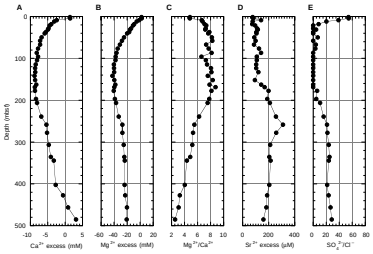

F18. Alkalinity vs. sulfate/chloride, **p. 48.**

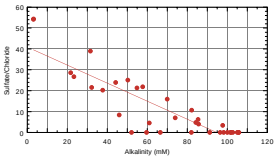

through the dissociation of H_2S, and this contribution makes the alkalinity deficit even greater than observed.

Carbonate recrystallization is evident not only from pore-water parameters, such as reduced Ca^{2+} and Mg^{2+} and enhanced Sr^{2+}, but also from cementation in the cores (see "Lithostratigraphy," p. 3). This is also reflected in the X-ray diffraction (XRD) results. X-ray diffraction analysis shows the presence of a small amount of dolomite throughout most of the core, with high concentrations at depths of 184.2, 247.99, and 305.8 mbsf (Table T7, also in ASCII format). It should be noted that the first major increase in the concentration of Sr^{2+}, as well as the maximum concentration of Sr^{2+}, coincides with the first and second dolomite peaks at 184.2 and 248.0 mbsf. The coincidence of the increase in Sr^{2+} with changes in mineralogy may suggest that the diagenetic changes are taking place at the present time.

X-Ray Mineralogy

The mineralogy at Site 1127 is dominated by variations between aragonite, LMC, and high-Mg calcite (HMC) (Table T7; Fig. F19). Quartz and dolomite show minor variations. Although the origin of these variations is not known at the present time, it is likely that the increase in the input of HMC occurs during sea-level highstands, whereas lowstands are dominated by higher concentrations of LMC (Droxler et al., 1983). Concentrations of dolomite appear to increase coincident with decreases in sea level. Toward the bottom of the cored section, the concentrations of both HMC and aragonite decrease, probably as a result of recrystallization of these metastable minerals. Notably, the first interval in which LMC is the dominant mineral occurs at 180 mbsf, coincident with increased lithification in the core (see "Lithostratigraphy," p. 3).

PHYSICAL PROPERTIES

Introduction

Measurements of physical properties at Site 1127 followed the procedures outlined in "Physical Properties," p. 19, in the "Explanatory Notes" chapter. These included nondestructive measurements of *P*-wave velocity (every 4 cm; Table T8, also in ASCII format), gamma-ray attenuation (GRA) bulk density (every 4 cm; Table T9), MS (every 8 cm; Table T10, also in ASCII format), and natural gamma radiation (NGR) (every 16 cm; Table T11, also in ASCII format) using the MST. The *P*-wave logger was activated only on APC cores. Thermal conductivity (Table T12, also in ASCII format) was measured in unconsolidated sediment at a frequency of one determination per core. A minimum of two discrete *P*-wave velocity measurements per section were made on the working half of the split cores (Table T13, also in ASCII format), although measurements could not be undertaken in lithified sediments because of the malfunction of the PWS3 contact probe system. Consequently, there are no determinations of *P*-wave velocity below 290 mbsf. Standard index properties (Table T14, also in ASCII format) and undrained shear strength (only in unconsolidated sediments) (Table T15, also in ASCII format) were measured at a frequency of one per section. No in situ measurements of formation temperature were made. Magnetic susceptibility data are discussed in "Paleomagnetism," p. 14.

T7. XRD data, p. 78.

F19. Variations in mineral concentrations, p. 49.

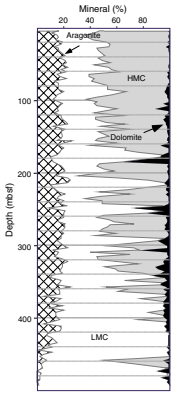

T8. *P*-wave velocity measurements, p. 81.

T9. GRA-densiometry measurements, p. 82.

T10. Magnetic susceptibility measurements, p. 83.

T11. Natural gamma-ray measurements, p. 84.

T12. Thermal conductivity measurements, p. 85.

T13. Discrete *P*-wave velocity, p. 86.

T14. Index properties measurements, p. 87.

T15. Undrained shear strength measurements, p. 88.

As described elsewhere (see "Operations," p. 2, and "Organic Geochemistry," p. 17), very high concentrations of H_2S were found through much of the cored interval. Exsolution of gas from recovered sediment, which in some cases caused expulsion of core onto the rig floor, greatly altered sediment physical properties. As NGR measurements are integrated over a larger depth interval than other measurements, these data proved to be the most useful for defining physical properties units (PP units).

Index Properties, *P*-wave Velocity, NGR, and GRA Densiometry

Three major PP units are recognized in the NGR data. Physical properties Unit 1 (0–135 mbsf) is characterized by the presence of three high-amplitude (>5 cps), ~50-m wavelength cycles in NGR superimposed on a rising downcore trend (Fig. F20). Gamma-ray attenuation bulk density (~1.6–1.8 g/cm³) and *P*-wave velocity (~1.7–1.4 km/s) decrease with depth in this unit (Fig. F20). Physical properties Unit 1 corresponds to lithostratigraphic Unit I and Subunit IIA and the upper part of seismic Sequence 2A.

Physical properties Unit 2 (135–466 mbsf) is characterized by lower amplitude (<4 cps) and higher frequency (~20-m wavelength) cyclicity in NGR activity, superimposed onto a slight rising trend with depth. The latter may be an artifact of the greater bulk density, which increases to 350 mbsf (Fig. F20). Thereafter, there is no significant change in GRA bulk density in this unit. *P*-wave velocity increases in parallel with GRA bulk density, although measurements at depth are limited to unlithified sediments and cannot be considered representative of the full range of in situ values (Fig. F20). Physical properties Unit 2 corresponds to lithostratigraphic Subunits IIB (lower part) to IIE and seismic Sequences 2A (lower part), 2B, and 2C.

The distinctive change from a predominantly ~50-m to a ~20-m cyclicity between PP Units 1 and 2 may represent the widely recognized mid-Pleistocene change in the response on the ocean/climate system to Milankovitch forcing (Prell et al., 1992; Imbrie et al., 1984). The 100-ka component, dominant in the upper Pleistocene, may correlate with the ~50-m cycle, whereas the ~20-m cycle lower in the core may correlate with the 41-ka obliquity signal.

Physical properties Unit 3 (466–508 mbsf) consists of Pliocene sediments that are correlated to lithostratigraphic Unit III. The upper boundary of this unit is marked by a decrease in NGR and an increase in GRA bulk density (Fig. F20). Inconsistencies in thermal conductivity data at Site 1127 as a result of gas disturbance of sediment physical properties make the data suspect.

The NGR data from the MST matches well with in situ wireline logging data, and there is an obvious correlation between specific peaks and the frequency of NGR cycles. However, log data show a decline in the amplitude of the ~20-m–wavelength cycles present in PP Unit 2 with depth, whereas the MST data show a trend to increasing amplitude (Fig. F20). Downhole logging spectral data suggest that the NGR signal is dominated by changes in uranium concentration (see "Downhole Measurements," p. 23). Although these changes are possibly driven by changes in the sedimentary aragonite, preliminary XRD data show no obvious association with NGR data (see "Inorganic Geochemistry," p. 19).

F20. *P*-wave velocity, uncorrected GRA and MAD bulk density, porosity, NGR, and MS, p. 50.

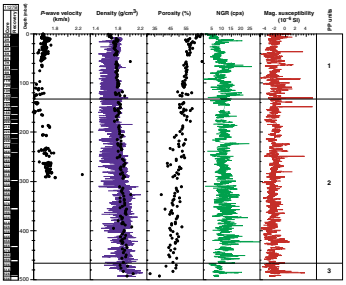

The effects of degassing on the physical properties of sediments at Site 1127 can be assessed by comparison of the mean and standard deviation of GRA bulk density per core with point measurements of bulk density from index properties determinations (Fig. F21). Between 0 and 86 mbsf, GRA bulk density decreases (Fig. F21) with a significant increase in the standard deviation from 0.04 to 0.07 g/cm³. Observations in sectioned cores suggest that this pattern was related to increasing delamination of the unlithified fine-grained sediment along primary bedding planes. Index properties samples from the same interval show a progressive increase of density with depth, as would normally be expected. Index properties bulk density more accurately reflects true sediment density, as it measures only the mass and volume of the solid and liquid phases and is not affected by artificial porosity resulting from gas disturbance. The difference between these two density measurements indicates a minimum core expansion of 12.5% at 100 mbsf, equivalent to 1 m for every 9 m cored. From 100 to 250 mbsf, the standard deviation of GRA bulk density readings increases (Fig. F21). This reflects the development of relatively widely spaced transverse cracks and some larger voids by degassing responding to the increased strength of the sediments in this interval (Fig. F22). Below 200 mbsf, GRA and moisture and density determinations increase and converge by a depth of 300 mbsf in response to increased lithification (Fig. F21). The higher strength of the lithified sediments precludes both delamination and cracking, and gas loss occurs predominantly by pore-scale exhalation.

F21. GRA bulk density and index properties sample bulk density, p. 51.

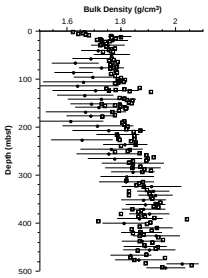

F22. Peak shear strength, p. 52.

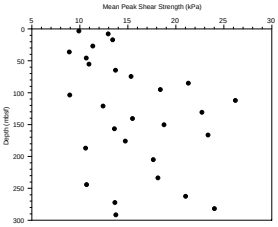

DOWNHOLE MEASUREMENTS

Logging Operations

After completion of drilling operations at Hole 1127B, the hole was prepared for logging (see "Operations," p. 2). As a result of high levels of H_2S in the recovered core (see "Organic Geochemistry," p. 17), sepiolite mud was added to the hole to reduce the chance of gas exsolution into the borehole. A corrosion inhibitor (Marvel Mystery Oil) was applied to the wireline cable to prevent chemical reactions between H_2S and steel, as this could result in stress cracking, reducing wireline cable ductility. Visual inspection of the wireline cable, tool casings, and tool joints during rig-down at the end of each tool run found no evidence to indicate that H_2S had affected the cable or tools.

Three tool strings were run in Hole 1127B in the following order: (1) a modified triple combo including the Lamont-Doherty Earth Observatory high-resolution temperature/acceleration/pressure tool, (2) FMS/sonic, and (3) GHMT/general-purpose inclinometer tool (GPIT) (Table T16, also in ASCII format). The pipe was placed at 87 mbsf and raised by 10 m during the first and third logging runs to extend the open-hole logged interval. The triple combo was run without the radioactive source in the density tool (hostile environment lithodensity sonde [HLDS]) because of the increased risk of losing the tool string during logging as a result of high H_2S concentrations. Thus, no density or photoelectric effect measurements were collected at this site with the HLDS, which essentially functioned as a caliper on this tool string. To reduce the exposure time of cable and tools to H_2S, no repeat section was measured and the downhole pass of the triple combo acted as a quality control run. A single main pass was made uphole at 550 m/hr (twice the normal logging speed) with the modified triple combo from 510.7 mbsf

T16. Tool strings, intervals logged, and logging speeds, Hole 1127B, p. 89.

to seafloor. Two passes of the FMS/sonic were made between 512.6 mbsf and the end of pipe. The FMS calipers were closed at 130 mbsf upon entering a washed out area below the pipe, whereas sonic velocity was logged into the pipe. A single pass with the GHMT/GPIT was run from 514.1 mbsf up into the pipe.

Data Quality

Conditions were excellent for logging at Hole 1127B. The wireline heave compensator was used during all logging runs and coped well with the moderate-to-light heave conditions. Borehole diameter as measured by the caliper log was remarkably uniform (~30–32 cm) from the base of the hole to 187 mbsf. Above 187 mbsf, the borehole diameter increased, with a maximum diameter of <40 cm.

Despite the fast wireline speed, the triple combo data appear to be of good quality. On the first FMS/sonic pass, the caliper arms failed to fully open, and contact with the borehole wall was poor. Consequently, the first pass is of poor quality, whereas the second pass produced high-quality FMS images. Excellent borehole conditions enabled the collection of a high-quality sonic log, reducing the need for the planned check-shot survey. The GHMT produced a good quality susceptibility log of the open-hole interval.

Preliminary Observations

Downhole logging data at Site 1127 are essential to understanding sedimentation at this site, as the recovered core underwent extensive disturbance during exsolution of H_2S and methane gases. Downhole trends in porosity, sonic velocity, and density at Site 1127 were dominated by compaction that results in gradual increases in velocity and density and decreases in porosity. Superimposed onto these trends are excursions that correlate to more indurated portions of the sedimentary sections. The most spectacular feature of the logs at Site 1127 is the cyclic nature of the NGR log. This cyclicity is likely to be a proxy of orbitally forced changes in sedimentation.

The entire section logged in Hole 1127B is characterized by a rather uniform appearance, both in geophysical logs and in the recovered core (Figs. **F23, F24, F25;** also see **"Lithostratigraphy,"** p. 3). The logged section is therefore defined as one logging unit, divided into three subunits on the basis of variations in the character of the gamma-ray log (Fig. **F24**).

Subunit 1A: 0–233 mbsf

Subunit 1A was logged through pipe to 80 mbsf, and in open hole for the remaining interval. Variations of NGR (15–35 American Petroleum Institute [API] units) in Subunit 1A are dominated by changes in uranium concentrations (Fig. **F24**). Porosity readings free of pipe effects vary between 50% and 90%, with a distinct high-porosity interval between 175 and 188 mbsf (Fig. **F25**). This marked increase in porosity immediately above a lithified horizon at 187 mbsf is probably an artifact caused by increased borehole diameter (from 12 to 14 in) not compensated for by the porosity sonde. Sonic velocities increase linearly with depth from ~1.8 to 2.1 km/s, indicating a normal compaction profile with some peaks, possibly resulting from thin beds of more indurated sediment (Fig. **F25**). The combination of low gamma radiation,

F23. Spectral gamma-ray logs from HNGS for variations in the interval logged through pipe, **p. 53.**

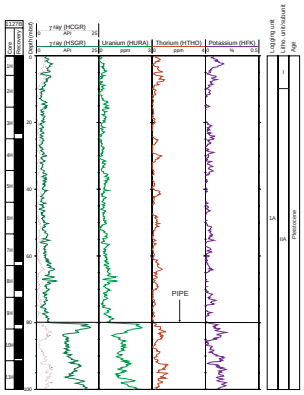

F24. Spectral gamma-ray logs from HNGS for the open-hole logged interval, **p. 54.**

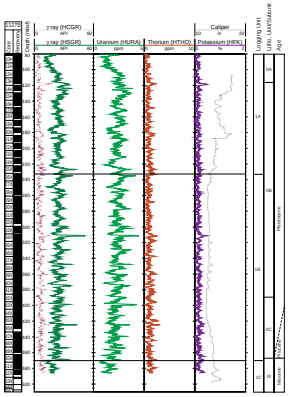

F25. Conventional geophysical logs vs. depth for the open-hole logged interval, **p. 55.**

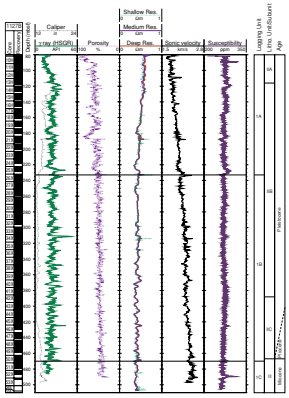

low porosity, and high velocity indicate that the boundary between logging Subunits 1A and 1B is a lithified horizon. This was not observed in the recovered core, possibly as a result of incomplete recovery at this depth (Figs. F24, F25; also see "Lithostratigraphy," p. 3). This conclusion is supported by FMS images that indicate the occurrence of a ~25-cm-thick lithified interval at the base of Subunit IA.

Subunit 1B: 233–470 mbsf

Subunit 1B is defined by a change to more high-frequency fluctuations in the cyclic character of the uranium gamma-ray log. The unit can be divided into 18–20 individual cycles, with cycle thickness decreasing downhole from 15–20 m in the top to ~10 m at the base of Subunit 1B (Figs. F24, F25). The top of logging Subunit 1B appears to correlate with Horizon A in seismic Sequence 2 (see "Seismic Stratigraphy," p. 26). Thus, Horizon A marks the initial change in cyclic character observed in logging Subunit 1B and may be useful for tracing the top of the cyclic package along the transect of Sites 1127, 1129, and 1131. The natural gamma cyclicity seen in Subunit 1B may result from changes in the organic matter content of the formation and/or variations in diagenetic concentration of uranium (e.g., associated with firmgrounds or "blackened grains"). Enrichments of diagenetic uranium are frequently associated with decreased porosity and increased density, sonic, and resistivity logs, and indicate the presence of hardgrounds that are also visible in FMS images as bright, resistive layers (Fig. F26). The FMS images from logging Subunit 1B show several horizons with highly conductive features 5–8 cm across that may be interpreted as either very large burrows or water-filled vugs in the borehole wall (Fig. F27). As a result of the large size of these features, our preferred interpretation is that they represent water-filled vugs caused by fluid (or gas) leaking into the borehole.

Subunit 1C: 470–510 mbsf

Subunit 1C is identified by a shift to lower gamma-ray values at the top of the subunit accompanied by a small decrease in resistivity and sonic velocity and an increase in MS. Subunit 1C displays relatively high sonic velocities (2.5 km/s), with porosity averaging ~40% (Fig. F25). The separation of shallow- and deep-resistivity logs in the lowermost part of Subunit 1C reflects fluid invasion as compared with Subunits 1A and 1B, where resistivity curves generally coincide (Fig. F25). The boundary between logging Subunits 1B and 1C at 470 mbsf coincides with a depositional hiatus at the Pleistocene/lower Pliocene boundary and corresponds to the boundary between lithostratigraphic Units II and III. Excessive borehole rugosity makes logging Subunit 1C appear chaotic on FMS images.

Downhole Temperature Gradients

A change in downhole temperature gradient was seen at 370 mbsf, accompanied by high variability in the temperature profile below this level (Fig. F28). The reason for this offset is unclear. The increase in temperature readings between downhole and uphole passes (2°–3°C) is probably caused by heating of borehole fluids toward formation temperature.

F26. FMS image from Subunit 1B, p. 56.

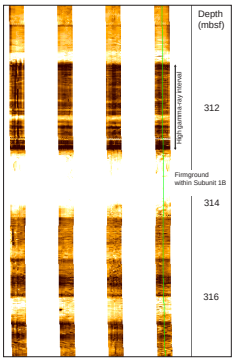

F27. FMS image from lower part of Subunit IB, p. 57.

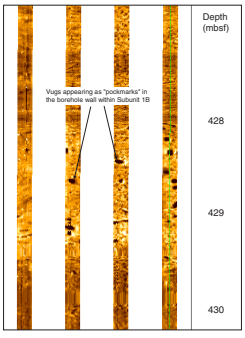

F28. Downhole variations in borehole temperature, p. 58.

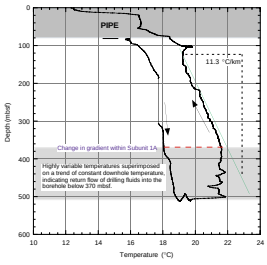

SEISMIC STRATIGRAPHY

Introduction

The seismic stratigraphic results from Sites 1127, 1129, and 1131 (Fig. F29) are considered together, as these sites represent a transect of three closely spaced sample points through the same sequences that form spectacular clinoforms beneath the modern shelf edge. The high-resolution site-survey seismic data (Fig. F30) show that Sites 1127 and 1129 penetrate thick Sequence 2 intervals and bottom in Sequence 3, whereas Site 1131 penetrates both Sequences 2 and 3 and bottoms in Sequence 4 (sequences defined in Feary and James, 1998, reprinted as Chap. 2). Seismic data indicate that the basal Sequence 2 sequence boundary should represent a significant hiatus, with the basal Sequence 3 sequence boundary probably representing a minor hiatus.

Time–Depth Conversion

Check-shot surveys using the single-channel WST were undertaken at Sites 1129 and 1131 to establish the time–depth relationship along this shelf edge to uppermost slope location and to correct the integrated sonic curves from Sites 1127, 1129, and 1131 for drift and for the pipe intervals. The parameters and procedures undertaken during these check-shot surveys are described in "Downhole Measurements," p. 26, in the "Site 1129" chapter and "Downhole Measurements," p. 23, in the "Site 1131" chapter. The 10 time–depth tie points derived from the check-shot survey at Site 1129 are presented in Figure F31, and the eight time–depth tie points derived from the survey at Site 1131 are presented in Figure F32. The presence of high methane and H_2S gas levels at Site 1127 caused deployment of downhole tools to be kept to a minimum until the effect of high gas levels on downhole equipment could be assessed. Accordingly, no check-shot survey was undertaken at this site. The establishment of a time–depth relationship (Fig. F33A) was dependent on use of the integrated sonic curve, constrained by results from the other two sites.

The time–depth tie points for Sites 1129 and 1131 were plotted on depth to two-way–traveltime graphs (Figs. F34A, F35A) to (1) determine the relationship between depths encountered at each site and sequence boundaries and horizons located on seismic data and (2) compare the check-shot–corrected time–depth relationships with predictions based on stacking velocities. These plots show that the actual time–depth relationships defined by the check-shot surveys fall toward the base of the envelopes defined by the stacking velocity curves for the immediate vicinity of each site. This is a result of stacking velocities providing an underestimate of true traveltimes. Based on this data, the integrated sonic curve for Site 1127 was also located toward the base of the stacking velocity envelope at this location. The velocity underestimates correspond to depth errors of (1) as much as 24 m between predicted and corrected depths to boundaries at Site 1127, (2) as much as 12 m between predicted and corrected depths to boundaries at Site 1129, and (3) as much as 15 m between predicted and corrected depths to boundaries at Site 1131 (Table T17, also in ASCII format). Plots of check-shot data and velocity for Site 1129 (Fig. F34B) and Site 1131 (Fig. F35B) show reasonably good correlations. Integrated sonic traces derived from

F29. Seismic site-survey tracks for Sites 1127, 1129, and 1131 in relation to other Leg 182 sites and the AGSO169 site-survey seismic lines, p. 59.

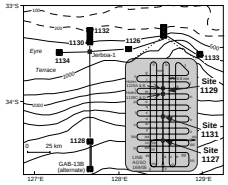

F30. Portion of seismic Line AGSO169/05a showing interpreted seismic stratigraphic sequences, p. 60.

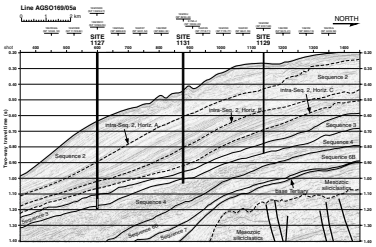

F31. Check-shot stations and acquisition geometry for the WST survey at Hole 1129D, p. 61.

Depth (mbrf)	Depth (mbsl)	Transit time (ms)	True path length (m)	Corrected TWT (ms)	Interval velocity (m/s)
368.0	356.1	221.24	394.7	442.22	1827.90
400.0	388.1	238.55	388.7	477.24	2027.76
440.1	428.2	258.11	428.8	516.79	2055.95
515.1	503.2	294.24	503.8	589.75	2121.02
580.2	568.3	324.78	568.9	651.11	2237.54
630.0	618.1	346.92	618.7	695.62	2435.08
680.2	668.3	367.43	668.9	736.85	2659.10
730.3	718.4	386.18	719.0	774.53	2470.65
759.9	748.0	398.11	748.6	798.49	2972.85
791.2	779.3	408.59	779.9	819.55	

Corrected TWT is TWT from sea level to WST tool along a vertical path

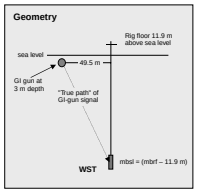

F32. Check-shot stations and acquisition geometry for the WST survey at Site 1131, p. 62.

Depth (mbrf)	Depth (mbsl)	Transit time (ms)	True path length (m)	Corrected TWT (ms)	Interval velocity (m/s)
490.2	478.5	302.15	478.9	605.08	1758.04
520.0	508.3	318.99	508.7	638.98	2087.78
550.1	538.4	333.31	538.8	667.81	2028.68
650.0	638.3	382.29	638.7	766.30	2138.07
750.0	738.3	428.88	738.7	859.84	2465.51
850.2	838.5	469.37	838.9	941.12	2434.49
880.2	868.5	481.66	868.9	965.77	2473.84
910.2	898.5	493.75	898.9	990.02	

Corrected TWT is TWT from sea level to WST tool along a vertical path

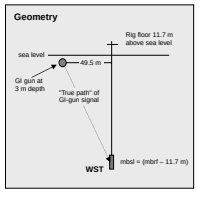

interval transit-time data for both sites (Figs. F34, F35) are in excellent agreement with stacking velocities.

Seismic Sequence Characteristics

The data collected at each of these sites show the site data within a more regional context and also allow a description of the characteristics of seismic sequences intersected at these sites (see "Lithostratigraphy," p. 3, and "Biostratigraphy," p. 9; "Lithostratigraphy," p. 4, and "Biostratigraphy," p. 12, in the "Site 1129" chapter; and "Lithostratigraphy," p. 3, and "Biostratigraphy," p. 9, in the "Site 1131" chapter). Correlations of lithostratigraphic and biostratigraphic data with seismic stratigraphy at Sites 1127 (Fig. F36), 1129 (Fig. F37), and 1131 (Fig. F38) are based on the regional moderate-resolution multichannel seismic data collected by the Japan National Oil Corporation (JNOC) in 1990 (Feary and James, 1998, reprinted as Chap. 2) and the high-resolution site-survey seismic data collected by the Australian Geological Survey Organisation (AGSO) in 1996 (Feary, 1997).

Sequence 2

Comparison of the high-resolution site-survey seismic data along the shelf edge transect with regional seismic data indicates that the Sequence 2 interval intersected at all three sites should represent a relatively complete succession, with the 467-m thickness at Site 1127 representing a more expanded upper Sequence 2 interval (Fig. F36), the 532-m thickness at Site 1131 representing a more expanded middle Sequence 2 interval (Fig. F38), and the 556-m thickness at Site 1129 representing a more expanded lower Sequence 2 interval (Fig. F37). The site-survey seismic data indicate that there should be significant facies differences between the Sequence 2 successions intersected at these three sites (Fig. F30). Site 1127 and the deeper parts of Sites 1129 and 1131 are characterized by uniform, continuous, evenly stratified clinoform reflectors, whereas the uppermost part of Site 1131 and the upper one-third of Site 1129 are characterized by mounded reflector geometries.

Lithostratigraphic data indicate that the continuous, evenly stratified reflectors at all three sites represent bioclastic packstone-dominated facies, with minor bioclastic wackestone and thin grainstone beds. The succession at Site 1127 shows a subtle cyclicity with alternating bioclastic wackestone- and packstone-dominated packages passing up into thin capping grainstone beds, interpreted as shallowing-upward cycles (see "Lithostratigraphy," p. 3). Downhole logging data indicate that this cyclicity is also present within the intervals characterized by continuous, evenly stratified reflectors at Sites 1129 and 1131 (see "Downhole Measurements," p. 23, in the "Site 1131" chapter, and "Downhole Measurements," p. 26, in the "Site 1129" chapter). The intervals characterized by mounded reflector geometries at Sites 1129 and 1131 are dominated by bryozoan floatstone and rudstone, interpreted as bryozoan mounds (see "Lithostratigraphy," p. 3, in the "Site 1131" chapter, and "Lithostratigraphy," p. 4, in the "Site 1129" chapter). The floatstone intervals alternate with bioclastic packstone intervals, interpreted to represent times when oceanographic conditions were unsuitable for bryozoan mound development (as at the present time).

Biostratigraphic data indicate that almost the entire thickness of Sequence 2 at all three sites represents Pleistocene accumulation overlying a thin (10–16 m) basal Pliocene interval. The Sequence 2 shelf edge

F33. Predicted and corrected depths and interval velocities for Site 1127, p. 63.

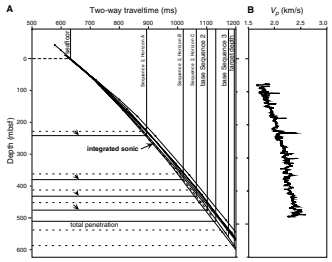

F34. Predicted and corrected depths and interval velocities for Site 1129, p. 64.

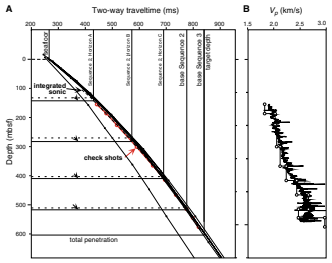

F35. Predicted and corrected depths and interval velocities for Site 1131, p. 65.

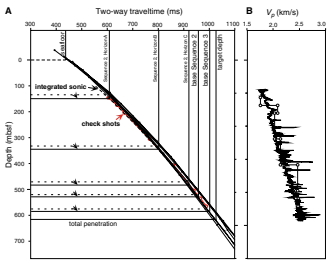

T17. Differences between depths to seismic horizons and corrected depths, p. 90.

F36. Lithostratigraphic units, seismic sequences, biostratigraphic hiatuses, and ages at Site 1127, p. 66.

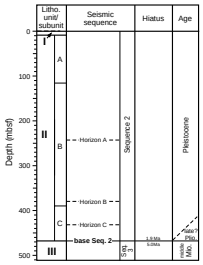

clinoform succession, therefore, represents a spectacularly high sediment accumulation rate. The sequence boundary at the base of Sequence 2 is an unconformity marking the transition from Pliocene- to middle Miocene-age sediments, representing a 10–12-m.y. hiatus.

Sequence 3

Site 1131 penetrated the entire 52-m thickness of Sequence 3, whereas Sites 1127 and 1129 penetrated only the upper 44 and 48 m, respectively. Biostratigraphic data indicate that Sequence 3 is of middle Miocene age. Recovery was very poor at all three sites, primarily as a result of preferential silicification of the well-lithified, partially dolomitized, bioclastic, glauconitic packstone to grainstone lithofacies apparently forming most of this sequence throughout the transect. The only other facies recovered was nannofossil chalk in the upper part of the Sequence 3 succession at Site 1127; seismic data confirmed that Site 1127 intersects a thin interval not represented at Sites 1131 or 1129. Despite the relative lithofacies uniformity, the seismic character of Sequence 3 varies considerably across the transect, from (1) poorly stratified, discontinuous to semicontinuous reflectors at Site 1127, in contrast to (2) low-amplitude, more evenly stratified and more continuous reflectors at Site 1131, and passing upslope to (3) higher amplitude, evenly stratified and continuous reflectors at Site 1129. This variability cannot be correlated with lithofacies differences, possibly because of the very poor recovery.

Sequence 4

Sequence 4 was only intersected in the deepest part of Site 1131, where biostratigraphic evidence indicates an ~20-m thickness of early Miocene age. Minimal recovery within this interval means that the sequence boundary was not observed. Lithostratigraphic data indicate that this sequence probably consists of the same well-lithified, partially dolomitized, bioclastic, glauconitic packstone to grainstone lithofacies forming the overlying Sequence 3. Similarly, the seismic character of the Sequence 4 interval intersected at this site is identical to the low amplitude, evenly stratified, continuous reflectors of the overlying Sequence 3.

F37. Lithostratigraphic units, seismic sequences, biostratigraphic hiatuses, and ages at Site 1129, p. 67.

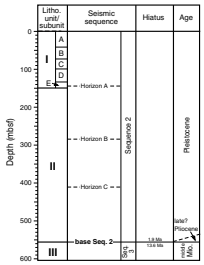

F38. Lithostratigraphic units, seismic sequences, biostratigraphic hiatuses, and ages at Site 1131, p. 68.

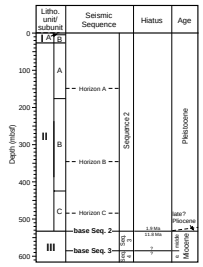

REFERENCES

Almond, D.O., McGowran, B., and Li, Q., 1993. Late Quaternary foraminiferal record from the Great Australian Bight and its environmental significance. *Mem. Assoc. Australas. Palaeontol.,* 15:417–428.

Bé, A.W.H., 1977. An ecological, zoogeographic and taxonomic review of Recent planktonic foraminifera. *In* Ramsay, A.T.S. (Ed.), *Oceanic Micropaleontology* (Vol. 1): London (Acad. Press), 1–100.

Berggren, W.A., Hilgen, F.J., Langereis, C.G., Kent, D.V., Obradovich, J.D., Raffi, I., Raymo, M.E., and Shackleton, N.J., 1995. Late Neogene chronology: new perspectives in high-resolution stratigraphy. *Geol. Soc. Am. Bull.,* 107:1272–1287.

Cisowski, S., 1981. Interacting vs. non-interacting single domain behavior in natural and synthetic samples. *Phys. Earth Planet. Inter.,* 26:56–62.

Curry, W.B., Shackleton, N.J., Richter, C., et al., 1995. *Proc. ODP, Init. Repts.,* 154: College Station, TX (Ocean Drilling Program).

Droxler, A.W., Schlager, W., and Whallon, C.C., 1983. Quaternary aragonite cycles and oxygen-isotope record in Bahamian carbonate ooze. *Geology,* 11:235–239.

Eberli, G.P., Swart, P.K., Malone, M.J., et al., 1997. *Proc. ODP, Init. Repts.,* 166: College Station, TX (Ocean Drilling Program).

Feary, D.A., 1997. ODP pollution prevention and safety panel: Leg 182 safety package—Cenozoic cool-water carbonates of the Great Australian Bight. *Aust. Geol. Surv. Org.,* 28.

Feary, D.A., and James, N.P., 1998. Seismic stratigraphy and geological evolution of the Cenozoic, cool-water, Eucla Platform, Great Australian Bight. *AAPG Bull.,* 82:792–816.

Foss, G.N., and Julson, B.D., 1993. Revised hydrogen sulfide drilling contingency plan—*JOIDES Resolution. ODP Tech. Note,* 19.

Gieskes, J.M., Gamo, T., and Brumsack, H., 1991. Chemical methods for interstitial water analysis aboard *JOIDES Resolution. ODP Tech. Note,* 15.

Hornibrook, N. de B., Brazier, R.C., and Strong, C.P., 1989. Manual of New Zealand Permian to Pleistocene foraminiferal biostratigraphy. *Paleontol. Bull. N.Z. Geol. Surv.,* 56:1–175.

Imbrie, J., Hays, J.D., Martinson, D.G., McIntyre, A., Mix, A.C., Morley, J.J., Pisias, N.G., Prell, W.L., and Shackleton, N.J., 1984. The orbital theory of Pleistocene climate: support from a revised chronology of the marine $\delta^{18}O$ record. *In* Berger, A., Imbrie, J., Hays, J., Kukla, G., and Saltzman, B. (Eds.), *Milankovitch and Climate* (Pt. 1), NATO ASI Ser. C, Math Phys. Sci., 126:269–305.

James, N.P., 1997. The cool water carbonate depositional realm. *Spec. Publ.—Soc. Econ. Paleontol. Mineral.,* 56:1–20.

James, N.P., Boreen, T.D., Bone, Y., and Feary, D.A., 1994. Holocene carbonate sedimentation on the west Eucla Shelf, Great Australian Bight: a shaved shelf. *Sediment. Geol.,* 90:161–177.

James, N.P., and von der Borch, C.C., 1991. Carbonate shelf edge off southern Australia: a prograding open-platform margin. *Geology,* 19:1005–1008.

Li, Q., James, N.P., Bone, Y., and McGowran, B., 1999. Palaeoceanographic significance of Recent foraminiferal biofacies on the southern shelf of Western Australia: a preliminary study. *Palaeogeogr., Palaeoclimatol., Palaeoecol.,* 147:101–120.

McGowran, B., Li, Q., Cann, J., Padley, D., McKirdy, D.M., and Shafik, S., 1997. Biogeographic impact of the Leeuwin Current in southern Australia since the late middle Eocene. *Palaeogeogr., Palaeoclimatol., Palaeoecol.,* 136:19–40.

Paull, C.K., Matsumoto, R., Wallace, P.J., et al., 1996. *Proc. ODP, Init. Repts.,* 164: College Station, TX (Ocean Drilling Program).

Prell, W.L., Murray, D.W., Clemens, S.C., and Anderson, D.M., 1992. Evolution and variability of the Indian Ocean summer monsoon: evidence from the western Ara-

bian Sea drilling program. *In* Duncan, R.A. (Ed.), *The Indian Ocean: A Synthesis of Results from the Ocean Drilling Program*. Am. Geophys. Union, 70:447–469.

Pujol, C., and Duprat, J., 1983. Quaternary planktonic foraminifers of the southwestern Atlantic (Rio Grande Rise) Deep Sea Drilling Project Leg 72. *In* Barker, P.F., Carlson, R.L., Johnson, D.A., et al., *Init. Repts. DSDP,* 72: Washington (U.S. Govt. Printing Office), 601–615.

Valet, J.-P., and Meynadier, L., 1993. Geomagnetic field intensity and reversals during the past four million years. *Nature,* 336:234–238.

Westbrook, G.K., Carson, B., Musgrave, R.J., et al., 1994. *Proc. ODP, Init. Repts.,* 146 (Pt. 1): College Station, TX (Ocean Drilling Program).

Figure F1. Map showing the location of Site 1127 on the eastern Eyre Terrace upper slope in relation to other Leg 182 sites and the Australian Geological Survey Organisation Survey 169 (AGSO169) seismic lines.

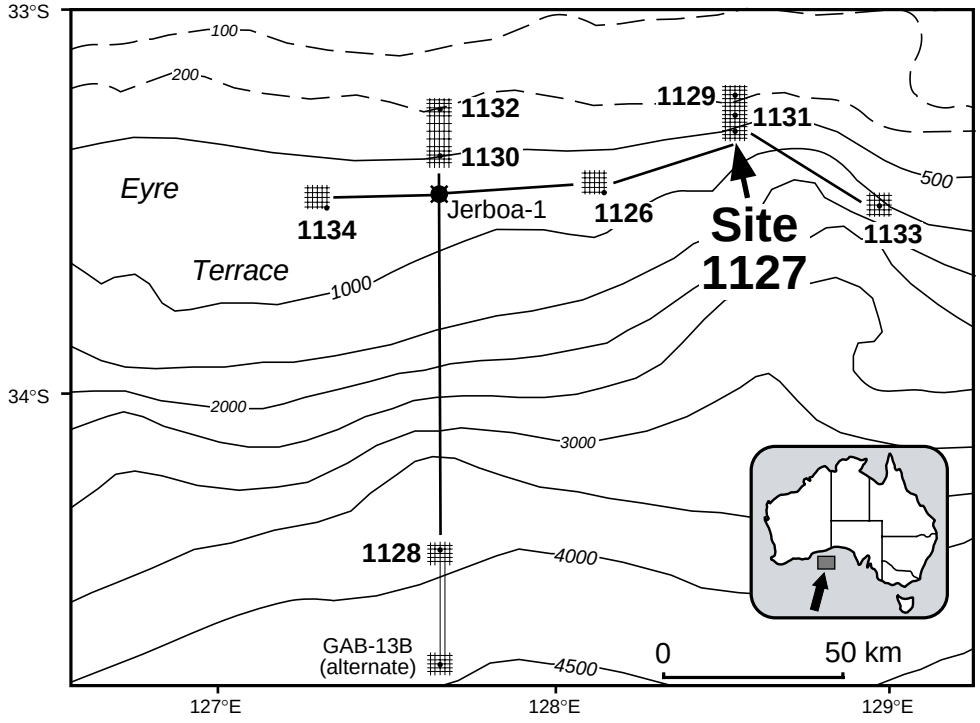

Figure F2. Portion of seismic Line AGSO169/05a showing interpreted seismic stratigraphic sequences planned (shown in white) and actually intersected (shown in black) at Site 1127. Note thick section of Sequence 2 consisting of sigmoidal clinoforms.

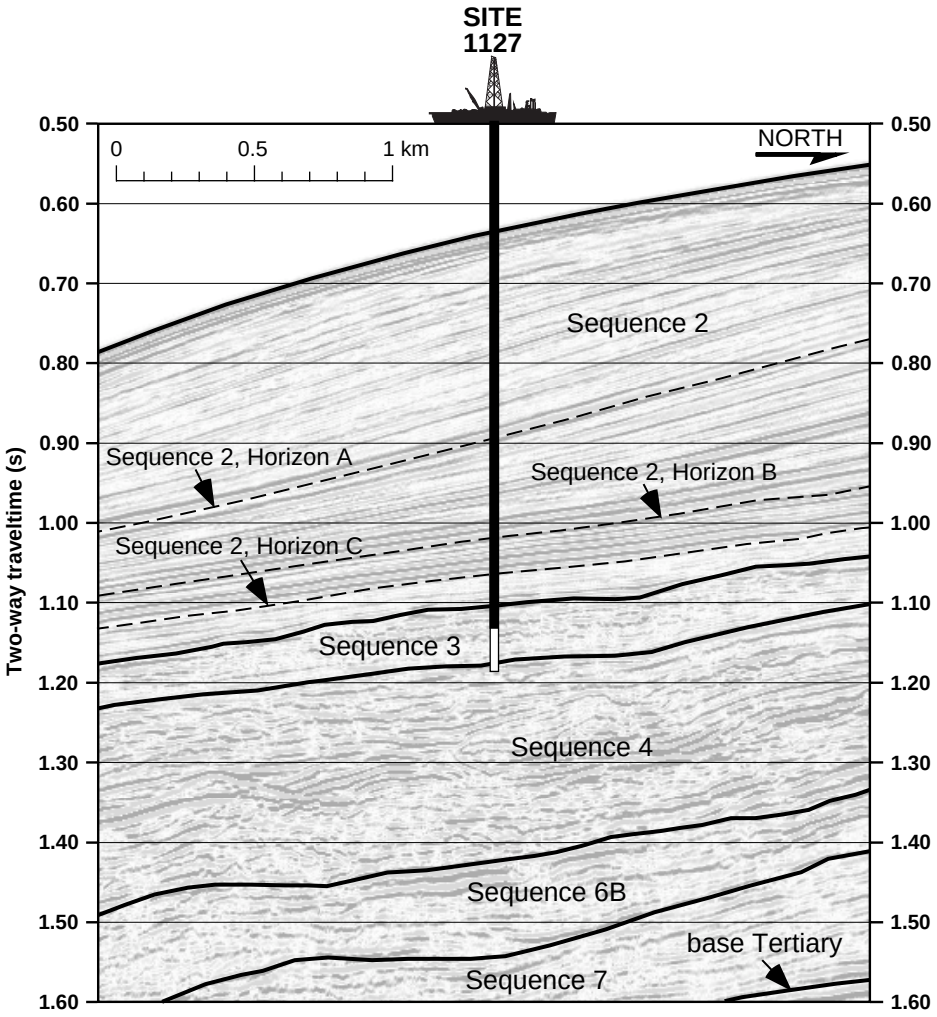

Figure F3. Lithostratigraphic summary log for Site 1127. Symbols in the lithostratigraphic column indicate the most abundant sedimentary particles. ? = magnetic intensity too low to measure. Ages and magnetostratigraphy are taken from "Biostratigraphy," p. 9, and "Paleomagnetism," p. 14.

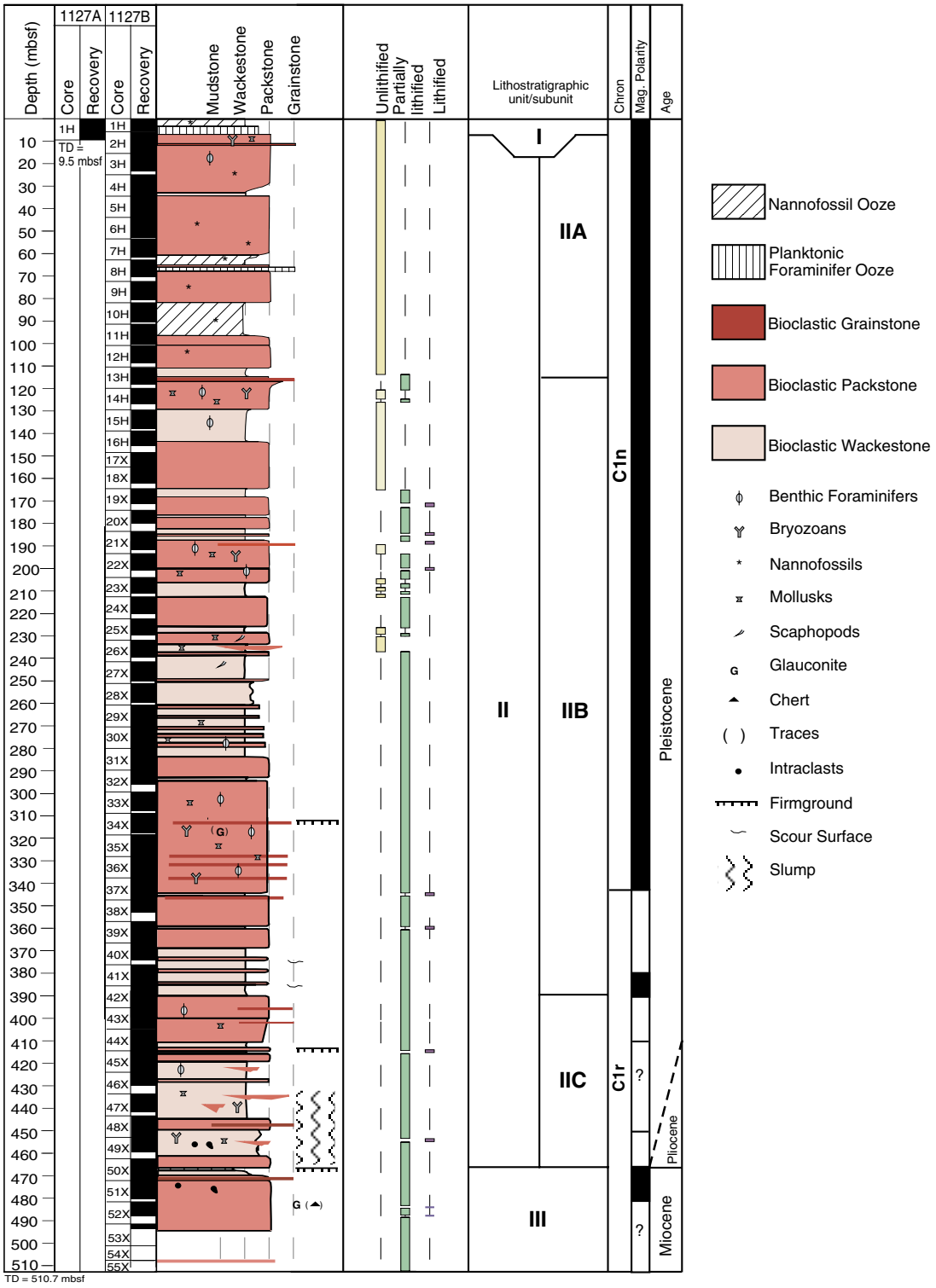

Figure F4. Summary of high-frequency sequences showing textural and grain-size changes. HFS = high-frequency depositional sequence; ? = magnetic intensity too low to measure. Ages, magnetostratigraphy, and the gamma-ray curve are taken from **"Biostratigraphy,"** p. 9, **"Paleomagnetism,"** p. 14, and **"Downhole Measurements,"** p. 23, respectively.

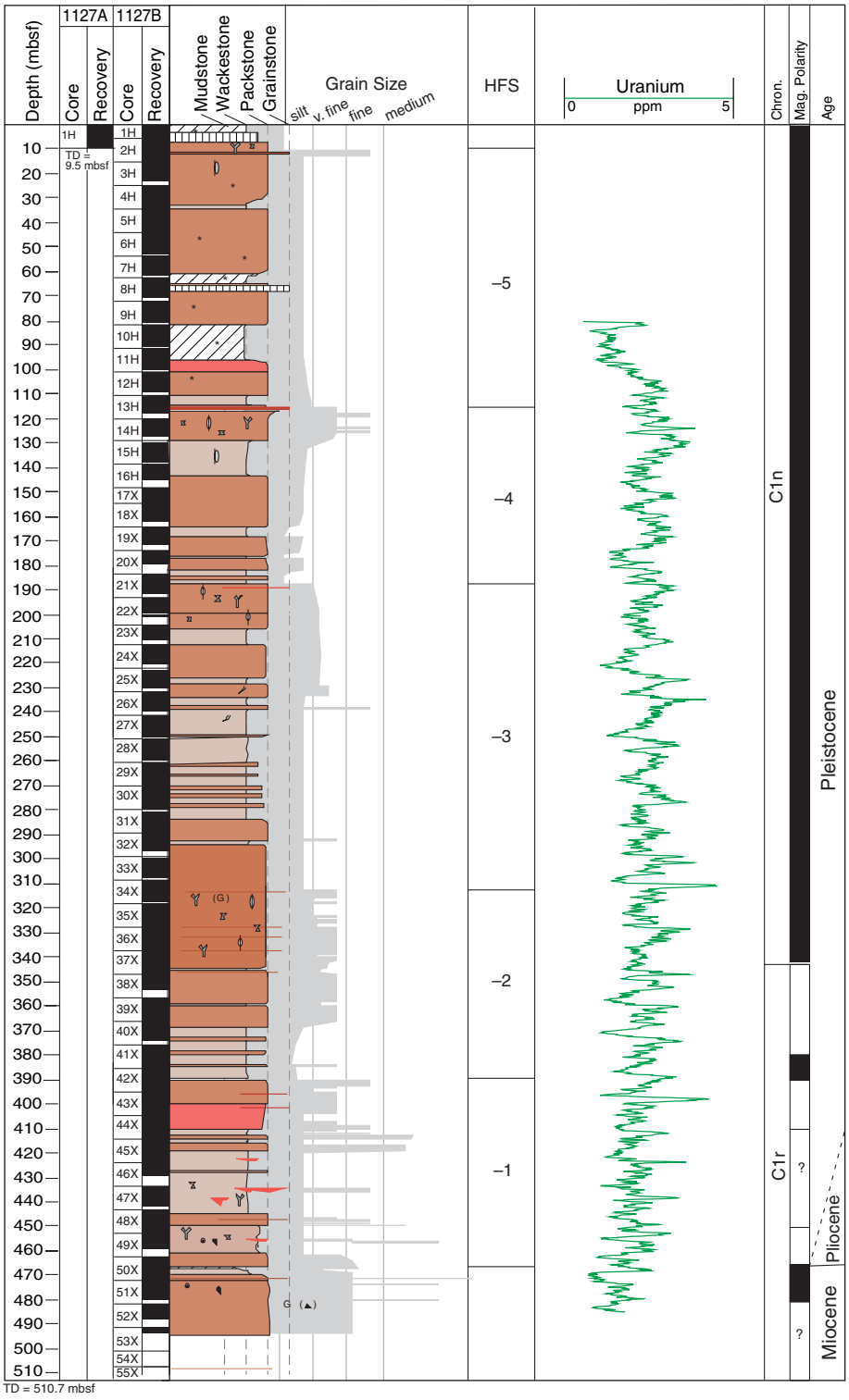

Figure F5. Stratigraphic position of calcareous nannofossil and planktonic foraminifer zones, together with benthic foraminifer assemblages at Site 1127. Dashed boundaries imply uncertainty. No sample means that the core catcher, if recovered, did not contain enough sediment to prepare for foraminifers.

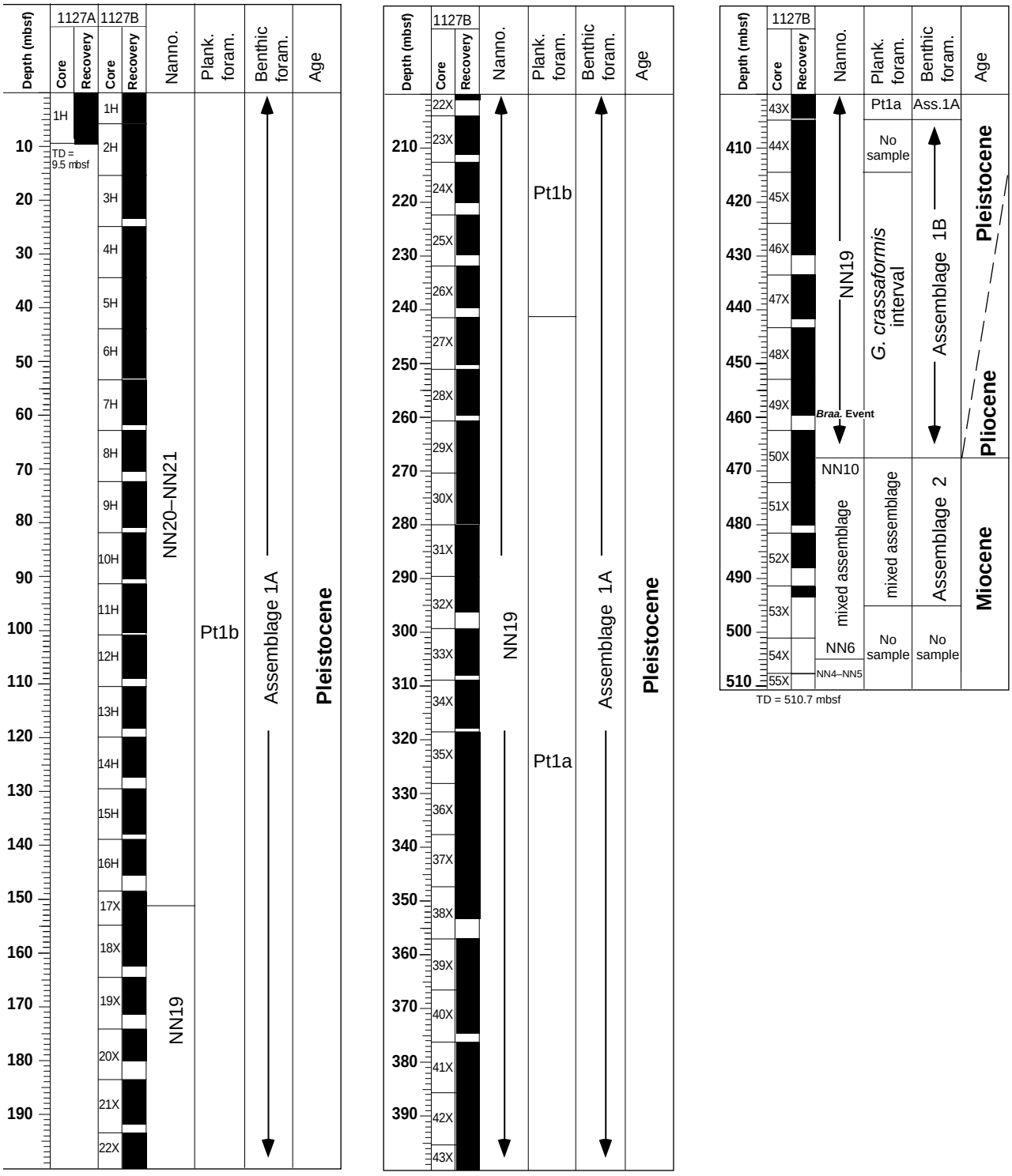

Figure F6. Sedimentation rate curve constructed from the 11 biostratigraphic datum levels listed in Table T2, p. 71. Stratigraphic error varies between ±1.425 and ±5.325 m, as indicated by the length of error bars.

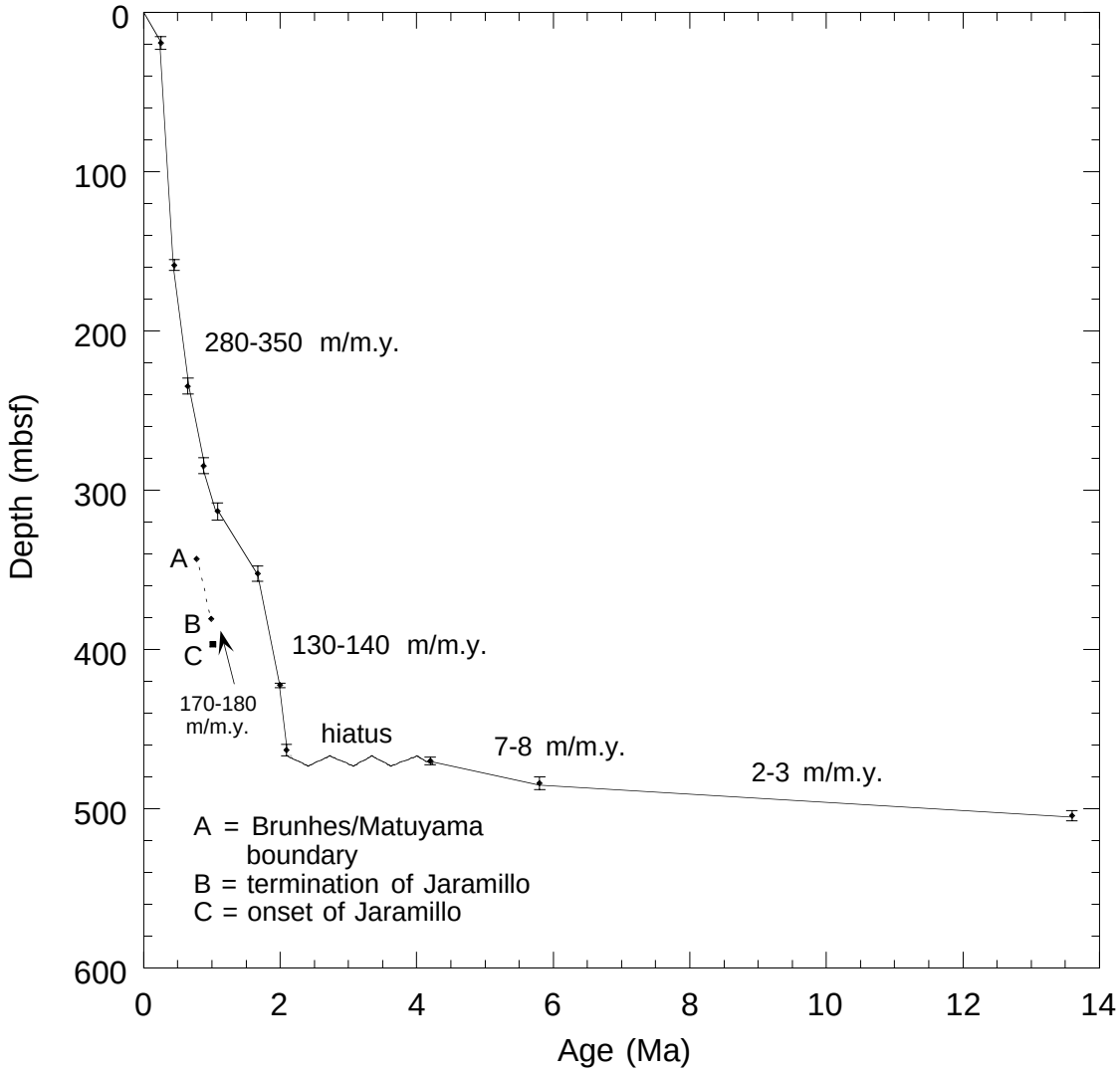

Figure F7. Downhole inclination determined (**A**) from natural remanent magnetization (NRM) long-core measurements and (**B**) after partial demagnetization at 20 mT, together with interpreted magnetostratigraphy. Long-core measurements (crosses) are compared with results from discrete samples (open squares).

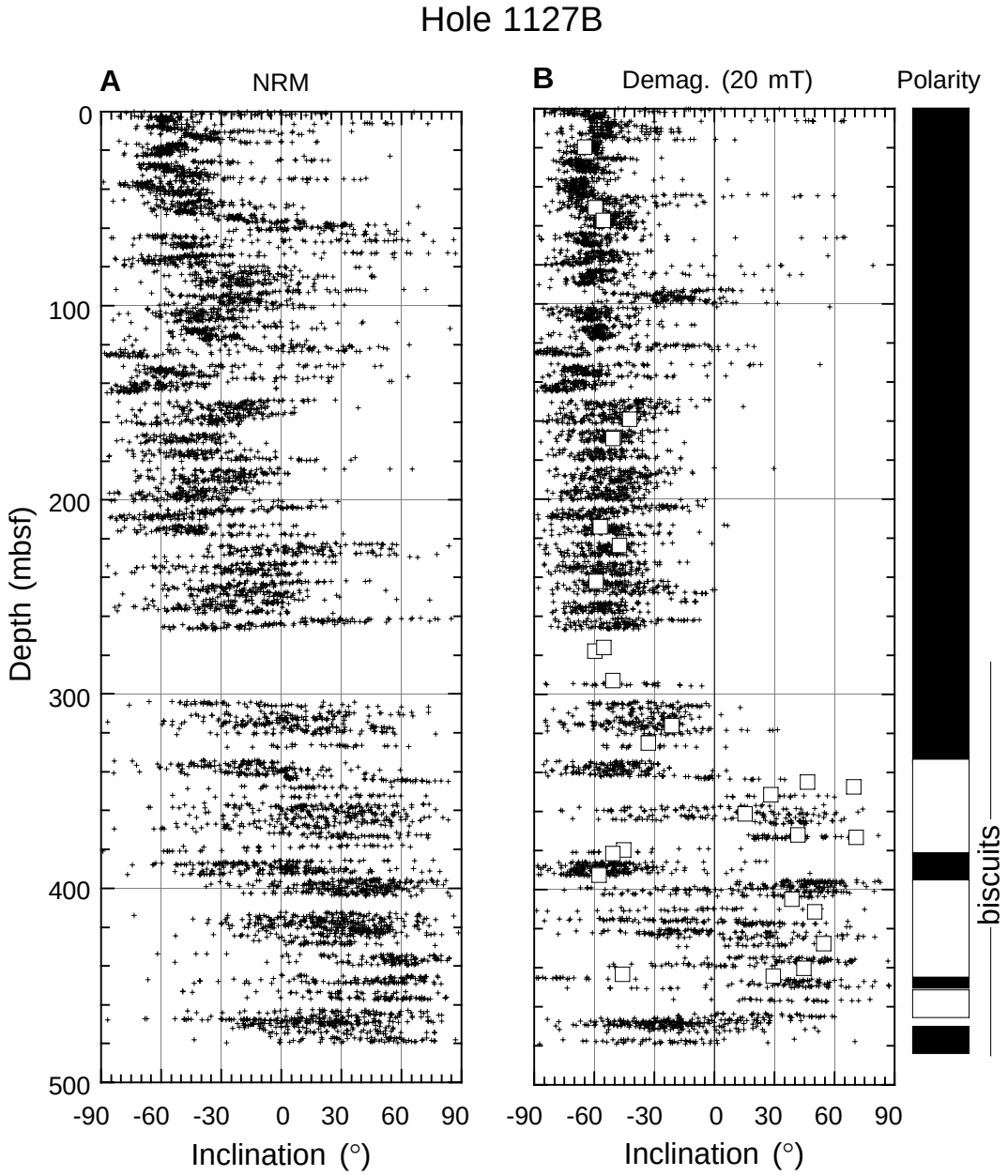

Figure F8. Normalized intensity decay (left) and demagnetization diagrams (right) of representative samples. **A.** Alternating field demagnetization showing two-component magnetization (Sample 182-1127B-25X-1, 135 cm). **B.** Thermal demagnetization showing univectorial decay of the natural remanent magnetization (NRM). Demagnetization diagrams show projections of the NRM vector in the vertical (open symbols) and horizontal (solid symbols) planes during progressive demagnetization (Sample 182-1127B-41X-3, 63 cm).

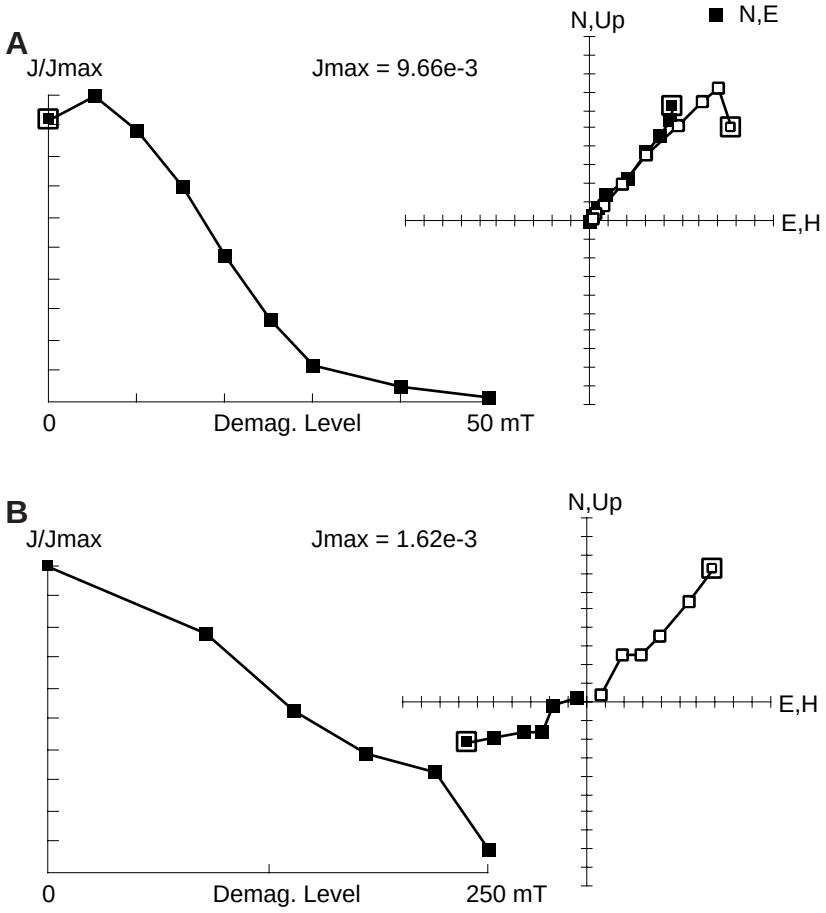

Figure F9. Long-core measurements of (**A**) the intensity of the remanent magnetization after partial demagnetization (20 mT) compared with (**B**) the composite paleointensity record (virtual axial dipole moment [VADM]) in the equatorial Pacific (Valet and Meynadier, 1993). Although the natural remanent magnetization (NRM) data are not normalized, the comparison suggests that the periodicity observed in the NRM record for the upper part of the Brunhes may be caused by ambient field variations.

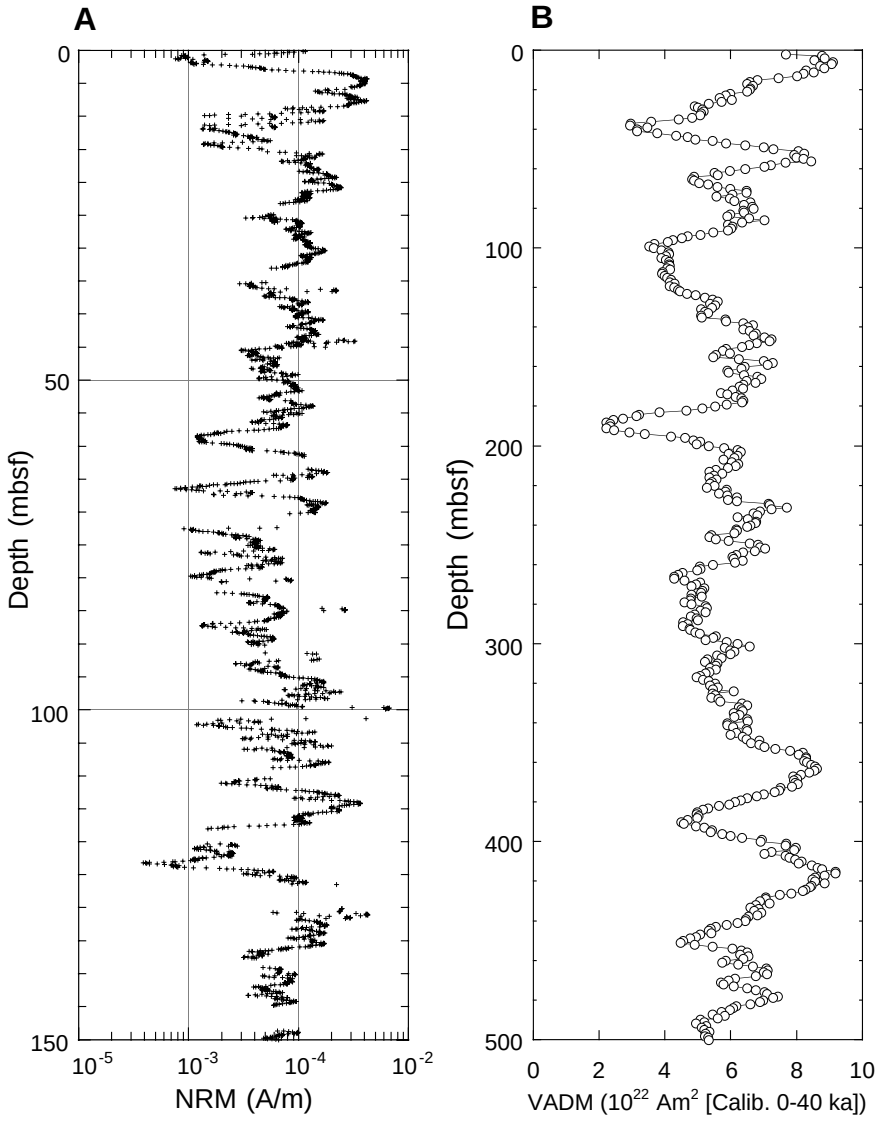

Figure F10. Plots of alternating field demagnetization of natural remanent magnetization (NRM), anhysteretic remanent magnetization (ARM), and isothermal remanent magnetization (IRM) and of the acquisition of IRM plot summarizing the magnetic characteristics of the analyzed samples. The acquisition of IRM illustrated is consistent with the presence of a cubic phase, and the demagnetization of NRM demonstrates that the intensity is above the noise limit of the instrument. SIRM 1, SIRM 2, and SIRM 3 were measured at ~24-hr intervals. The decrease in saturation isothermal remanent magnetization (SIRM) is attributed to the destruction of a ferromagnetic phase, of which greigite is the most likely candidate. The ratio of IRM:ARM is indicative of single-domain behavior.

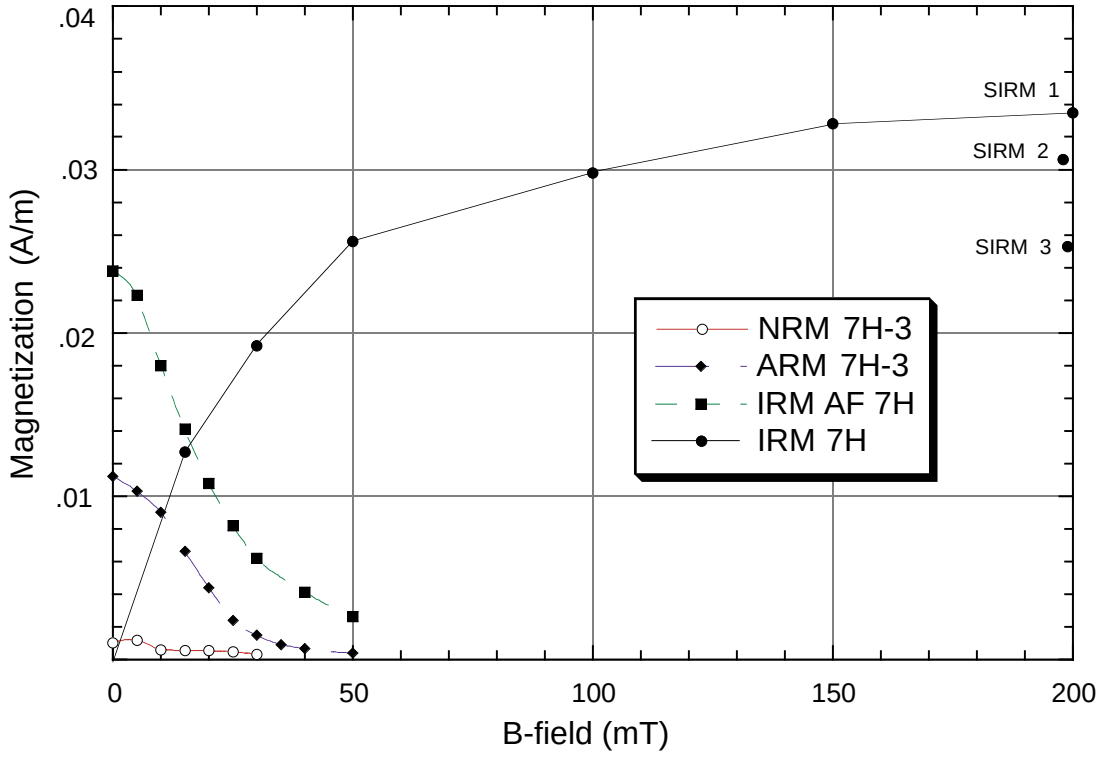

Figure F11. Methane (C_1) concentration, methane/ethane (C_1/C_2) values, and hydrogen sulfide (H_2S) concentration of vacutainer gases from Hole 1127B. ppmv = parts per million by volume.

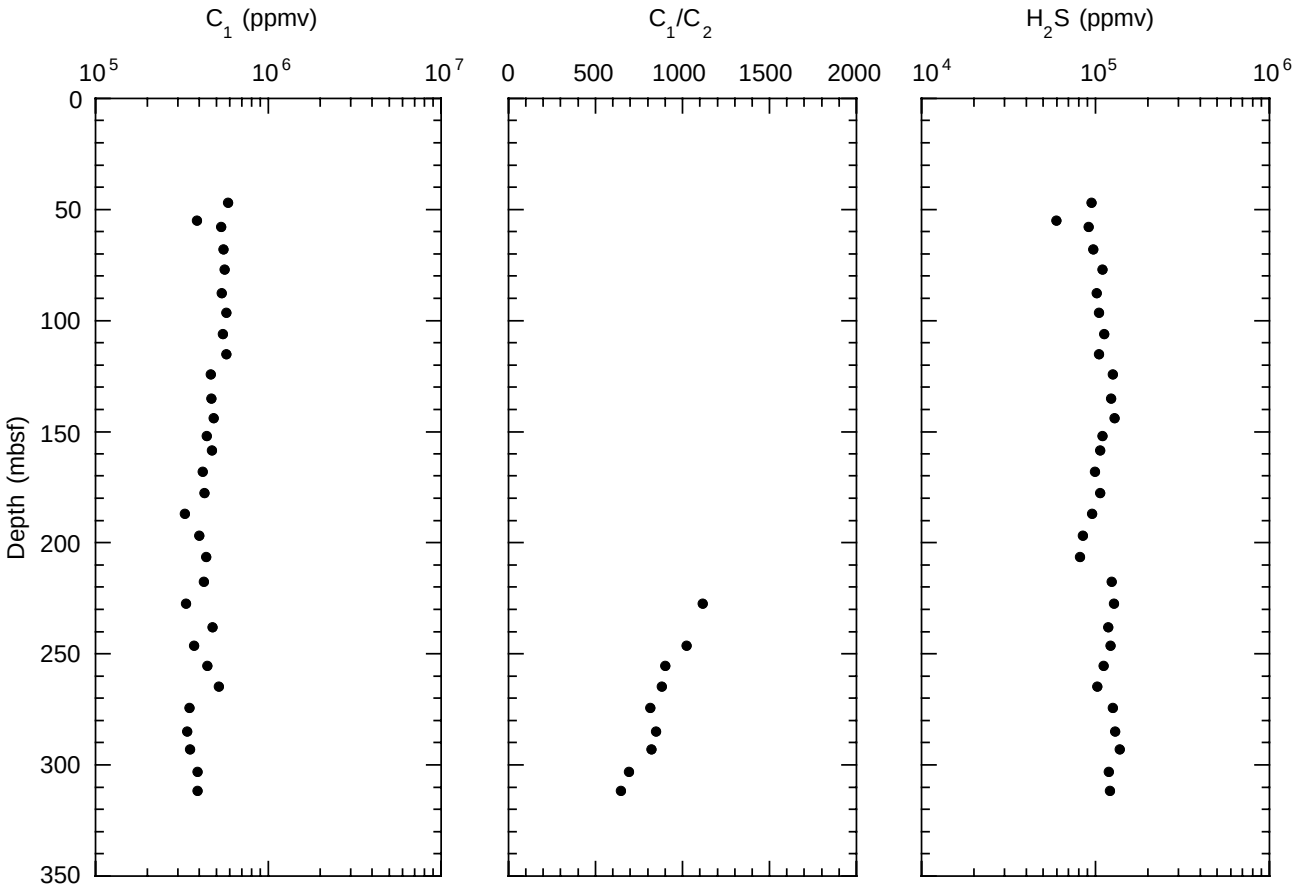

Figure F12. Methane (C_1) concentration, methane/ethane (C_1/C_2) values, and hydrogen sulfide (H_2S) concentration of headspace gases from Hole 1127B. ppmv = parts per million by volume.

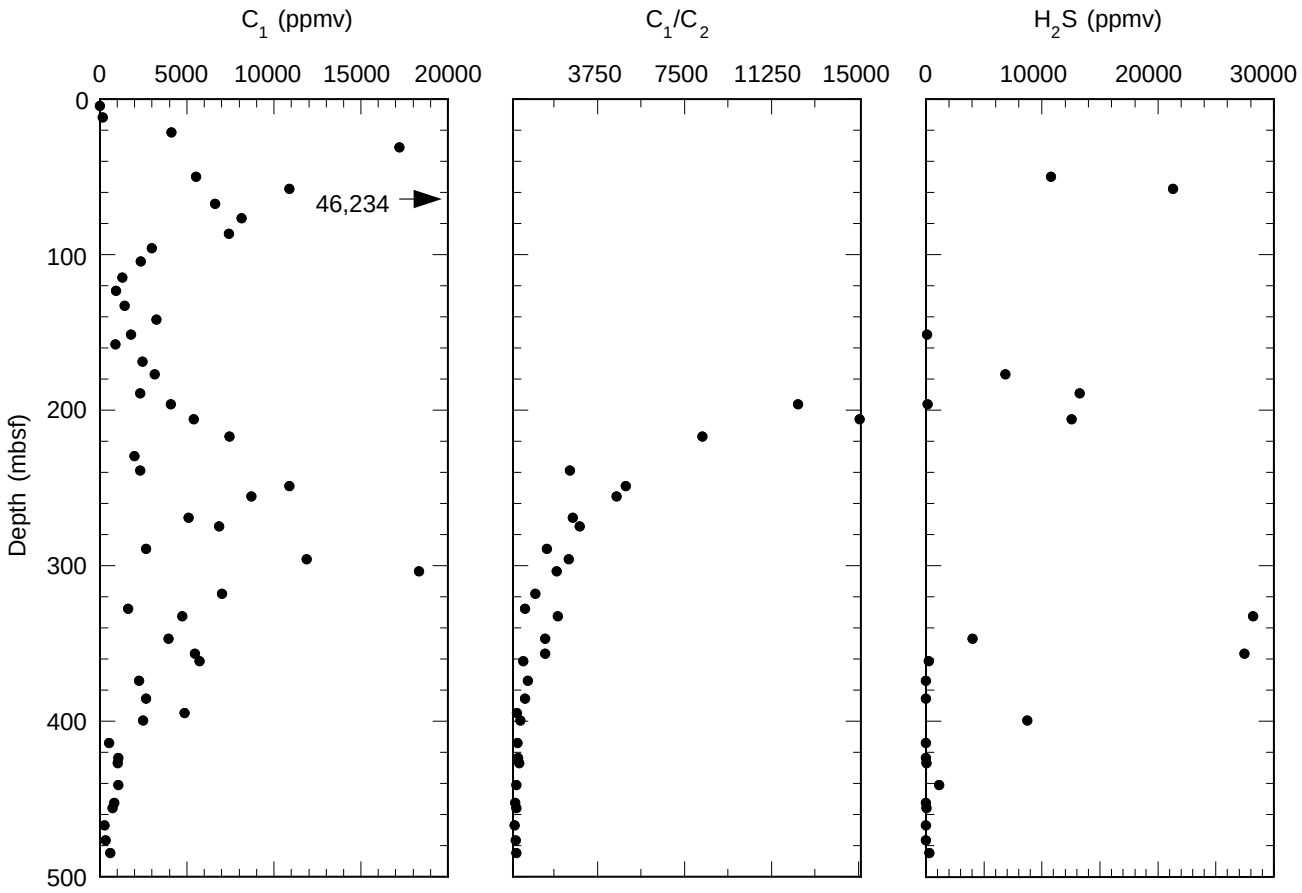

Figure F13. Calcium carbonate ($CaCO_3$) and organic carbon (C_{org}) contents in samples from Hole 1127B.

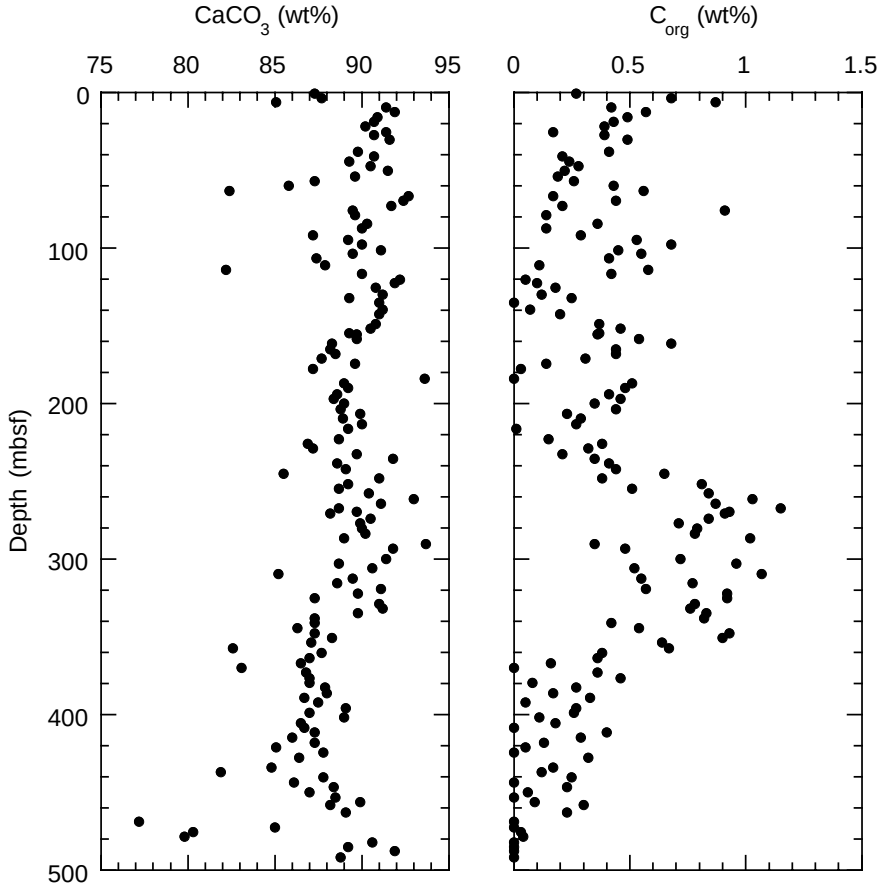

Figure F14. Salinity and chlorinity vs. depth distribution in Hole 1127B. The scatter of the salinity values between 100 and 340 mbsf is most likely caused by contamination with drilling fluid.

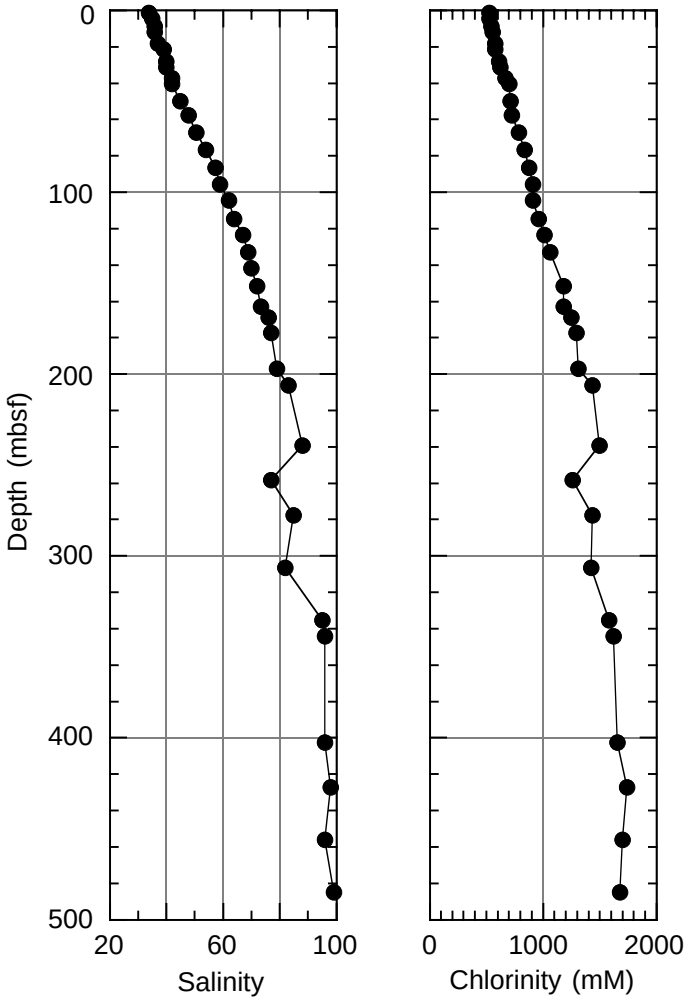

Figure F15. Depths vs. concentration profiles for (**A**) K^+, (**B**) Ca^{2+}, (**C**) Mg^{2+}, (**D**) Sr^{2+}, (**E**) $H_4SiO_4^0$ and (**F**) Li^+. Note that most of the observed variations are caused by the increasing salinity of the pore fluids.

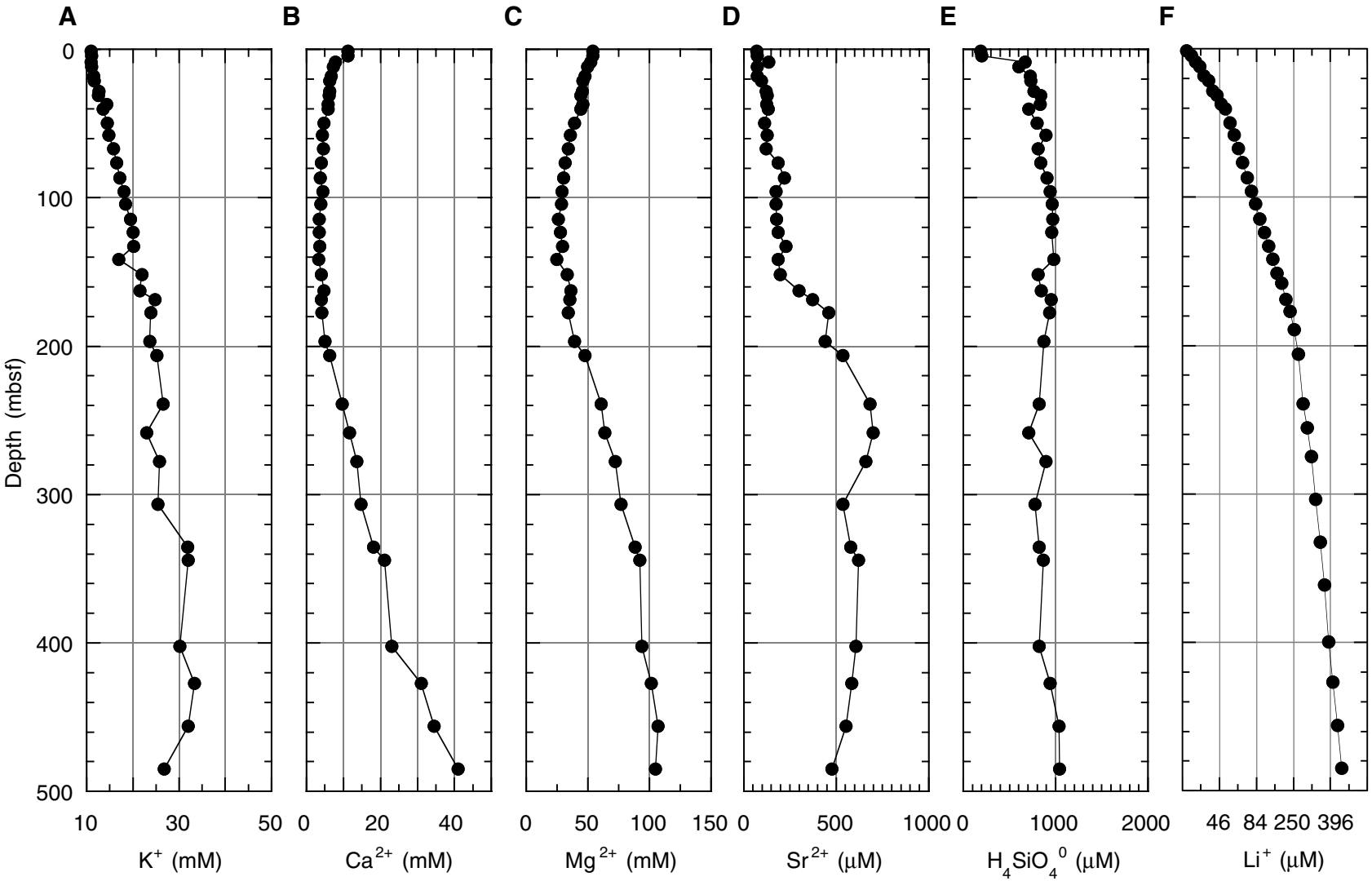

Figure F16. Depths vs. concentration profiles for (**A**) NH_4^+, (**B**) HPO_4^{2-}, (**C**) SO_4^{2-}, (**D**) alkalinity, (**E**) pH, and (**F**) pH determined using a punch-in electrode (ppH).

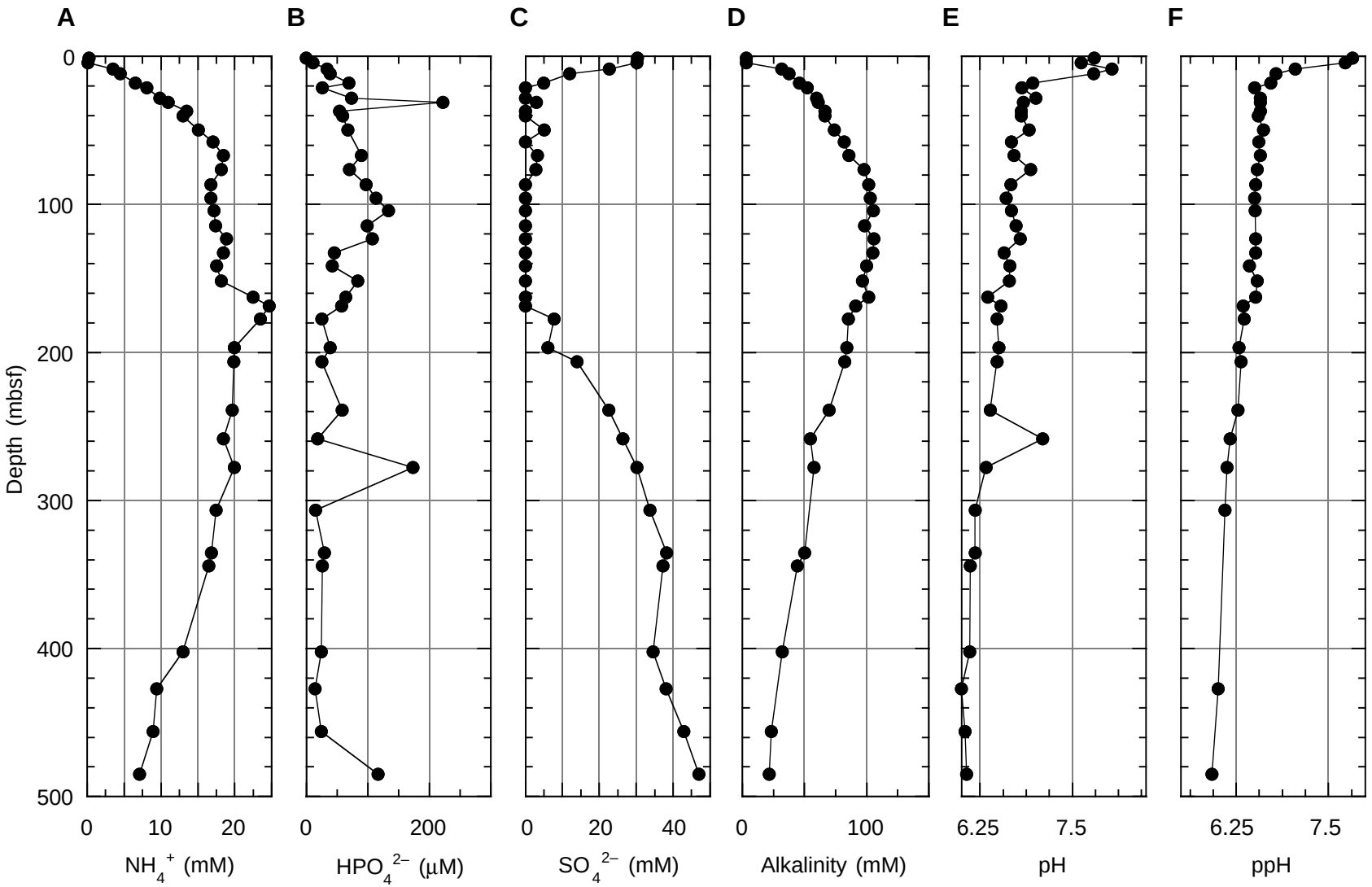

Figure F17. Depths vs. concentration profiles for (**A**) Ca^{2+} excess, (**B**) Mg^{2+} excess, (**C**) Mg^{2+}/Ca^{2+}, (**D**) Sr^{2+} excess, and (**E**) SO_4^{2-}/Cl^-. Because of the increase in salinity, excess concentration was calculated as $(M/Cl^- - a) \times Cl^-$, where $M = Ca^{2+}$, Mg^{2+}, or Sr^{2+}, and $a = M/Cl^-$ of standard seawater (i.e., International Association for the Physical Sciences of the Ocean). The values were taken from Gieskes et al. (1991).

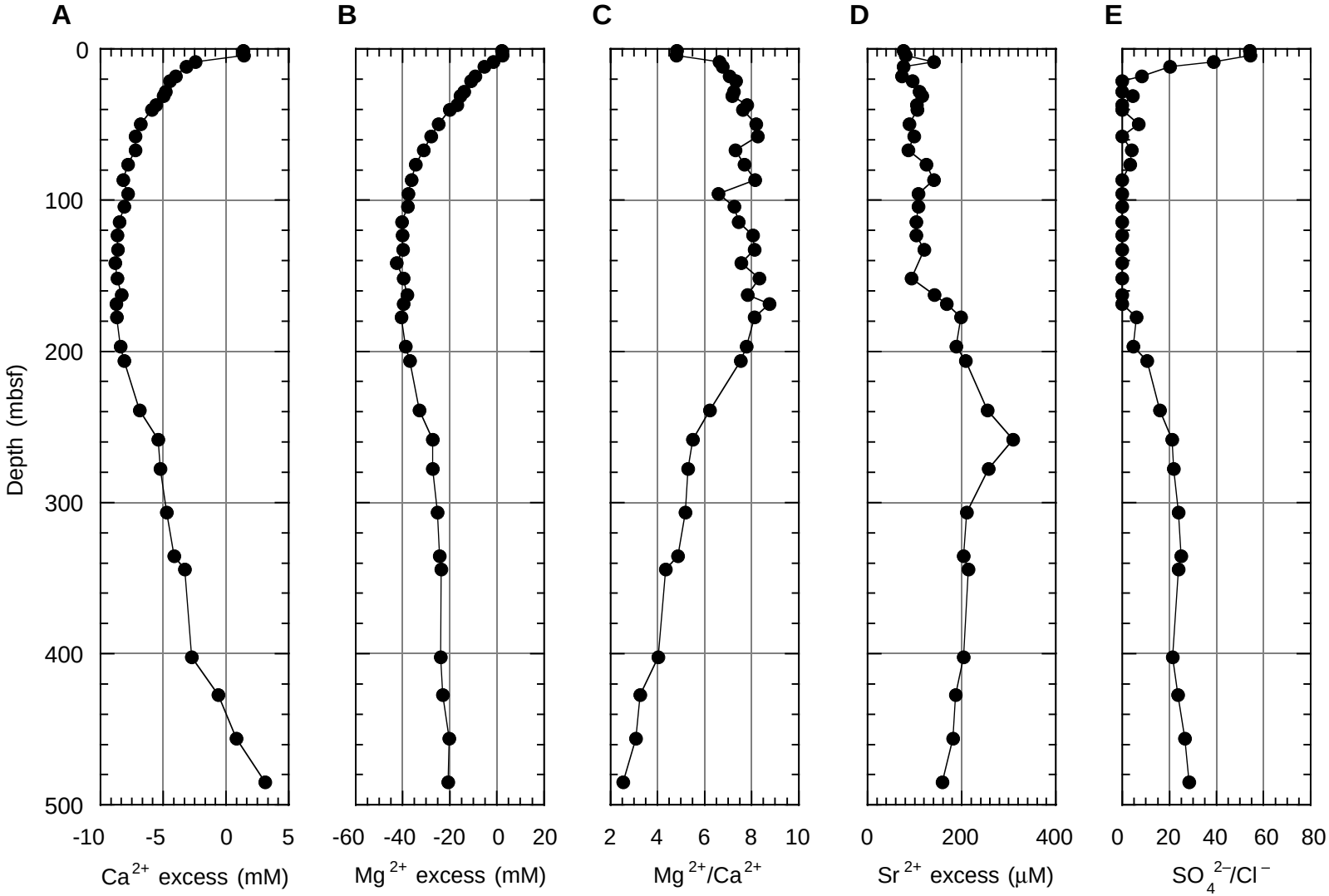

Figure F18. Relationship between alkalinity and the sulfate/chloride ratio in the pore fluids. The line shows the ideal 2:1 relationship in the absence of other diagenetic reactions involving alkalinity.

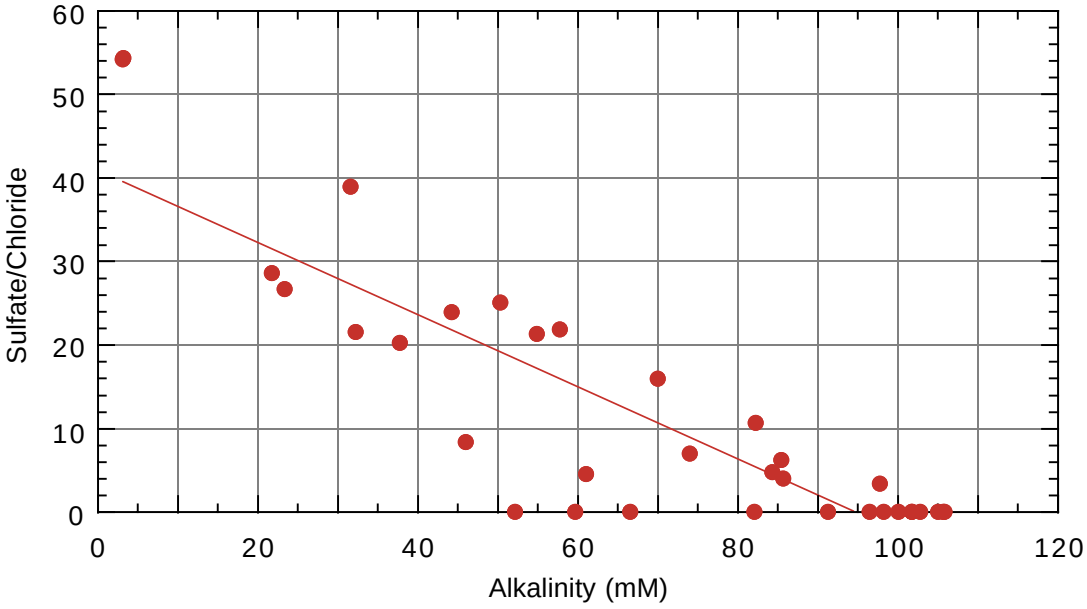

Figure F19. Variations in the concentration of aragonite, low-Mg calcite (LMC), high-Mg calcite (HMC), and dolomite at Site 1127. Calculations assume that the sediment is composed solely of these minerals and make no allowance for the presence of insoluble minerals (see "Organic Geochemistry," p. 17).

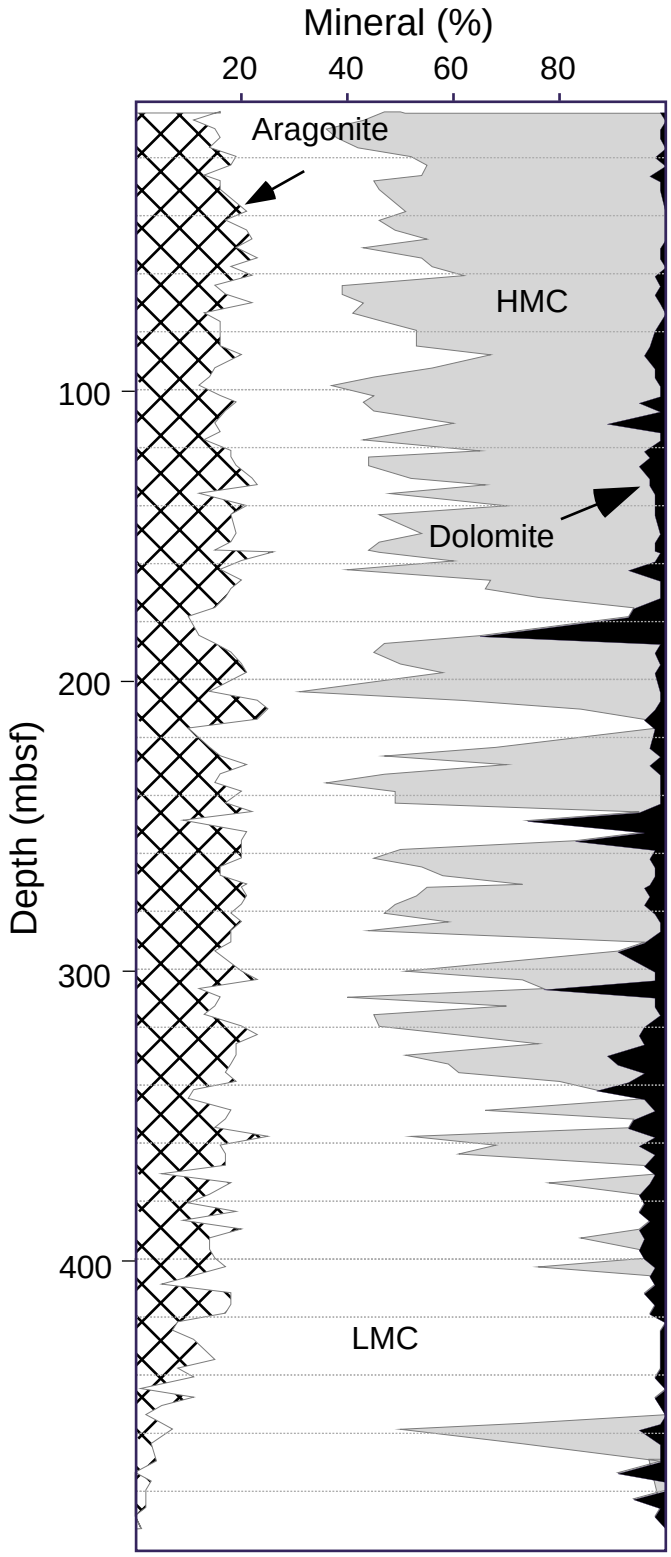

Figure F20. Combined plot of *P*-wave velocity, uncorrected gamma-ray attenuation (GRA [line]) and moisture-and-density (MAD) bulk density (dots), porosity, natural gamma radiation (NGR), and magnetic susceptibility for Site 1127. Physical properties units (PP units) are indicated on the right.

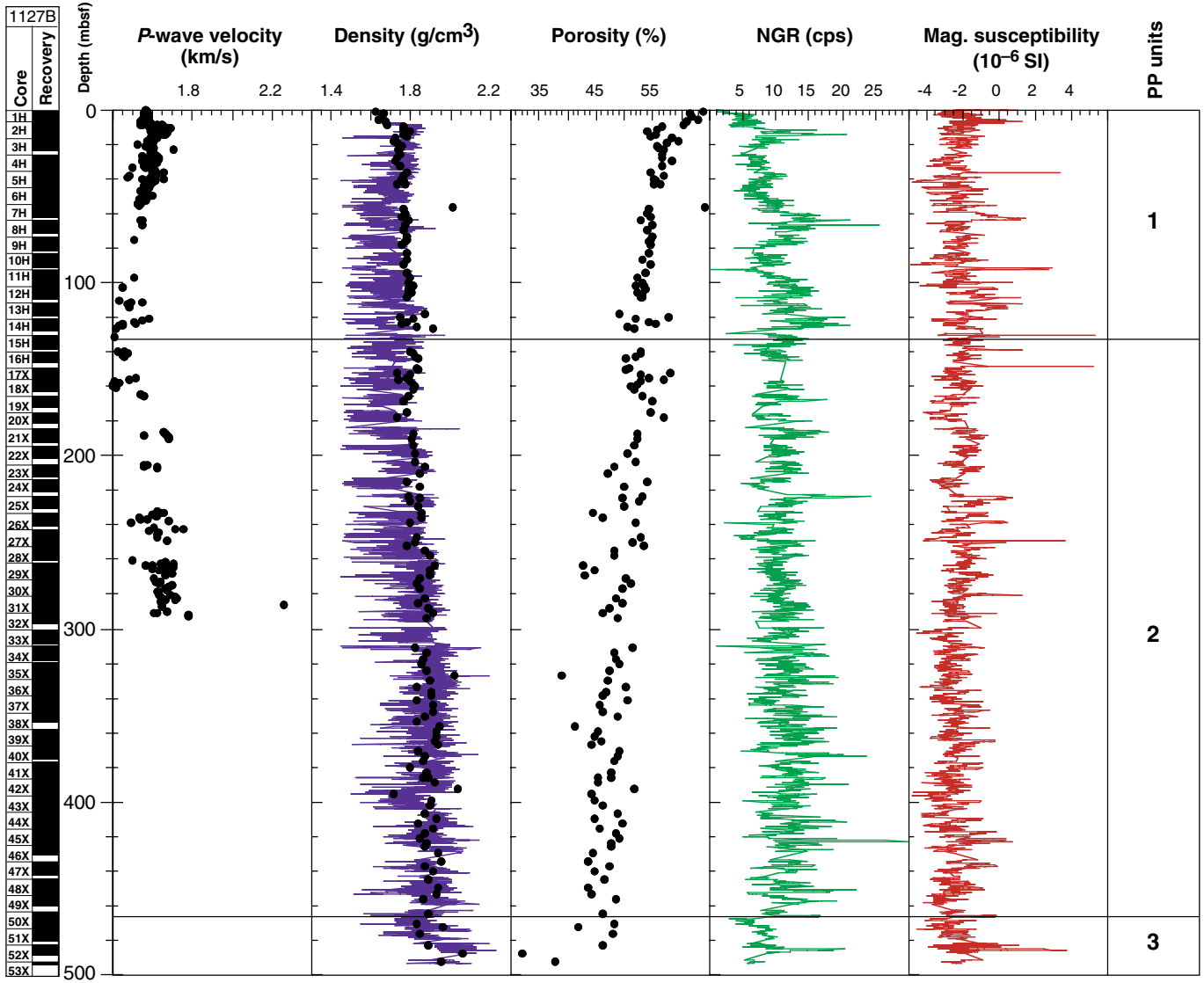

Figure F21. Variation with depth of mean (solid circles) and standard deviation (lines) of gamma-ray attenuation bulk density and index properties sample bulk density (open squares) for Site 1127.

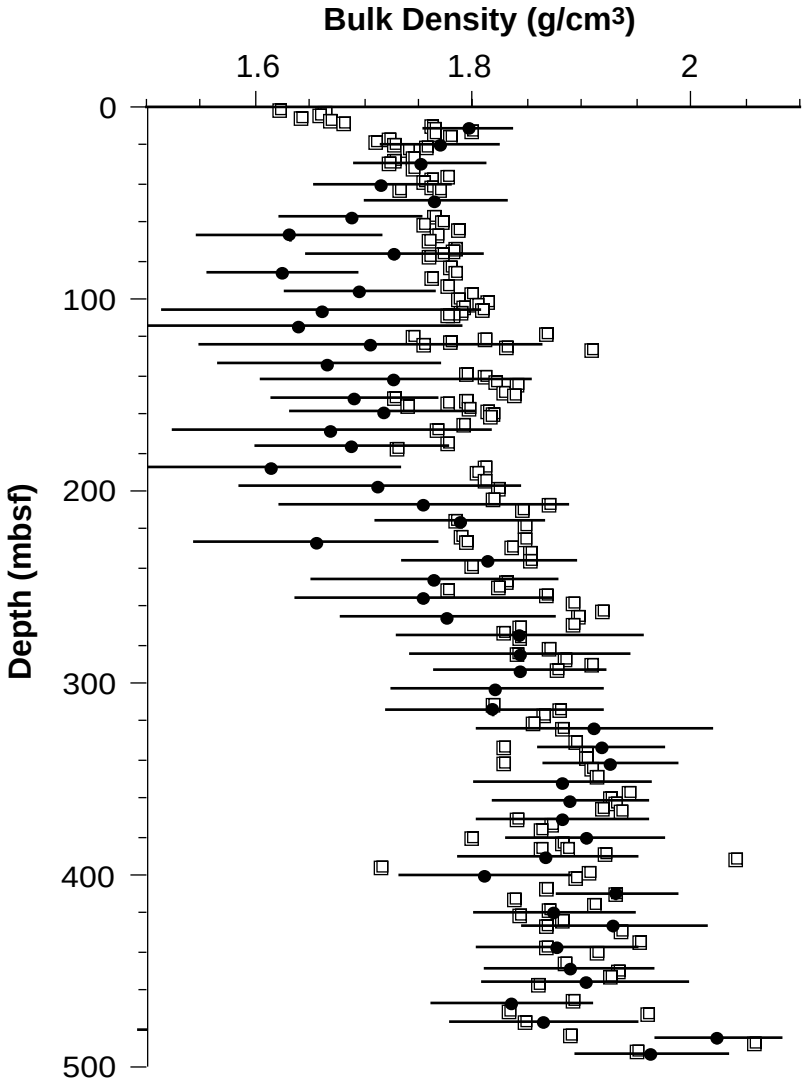

Figure F22. Variation of peak shear strength with depth at Site 1127.

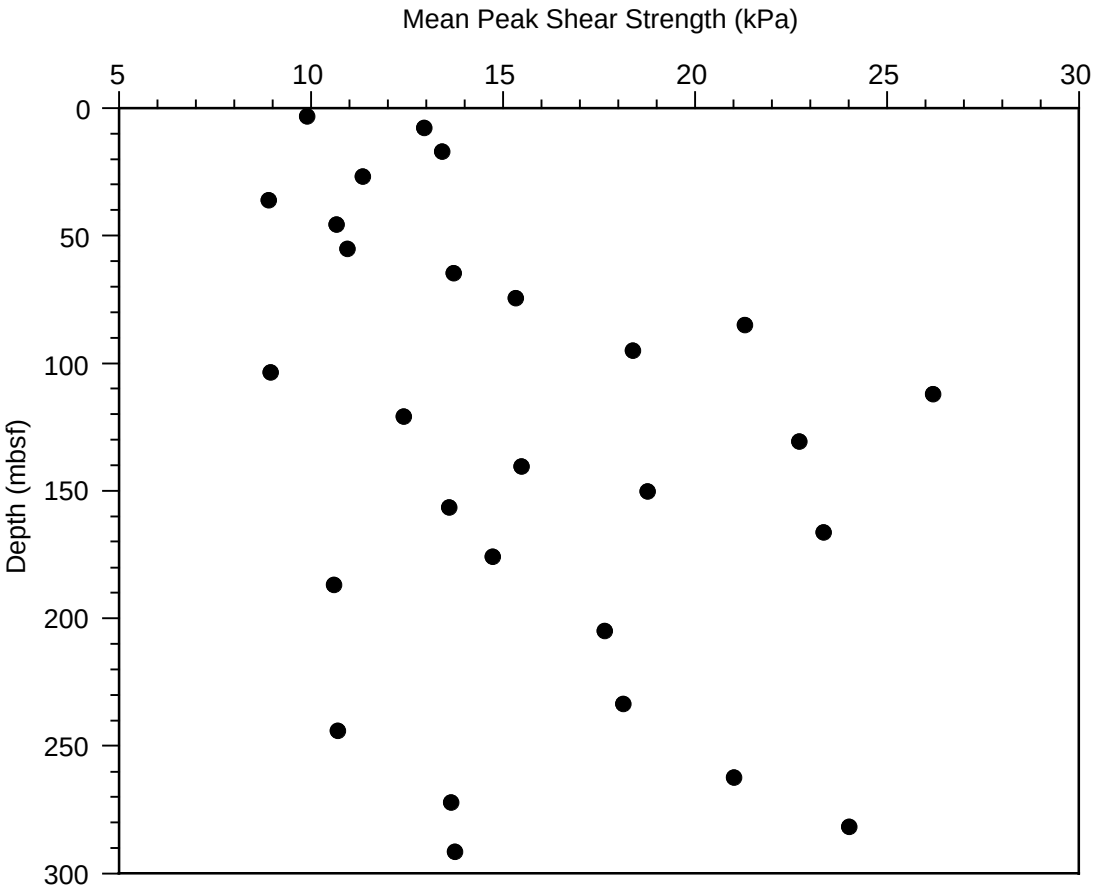

Figure F23. Summary of spectral gamma-ray logs from the hostile environment natural gamma-ray sonde (HNGS) plotted on an expanded depth scale to highlight variations in the interval logged through pipe. From left to right, columns are core recovery, total gamma radiation (from HSGR) and computed (uranium-free) gamma radiation (HCGR), uranium, thorium, potassium, logging units, lithostratigraphic units, and biostratigraphic ages.

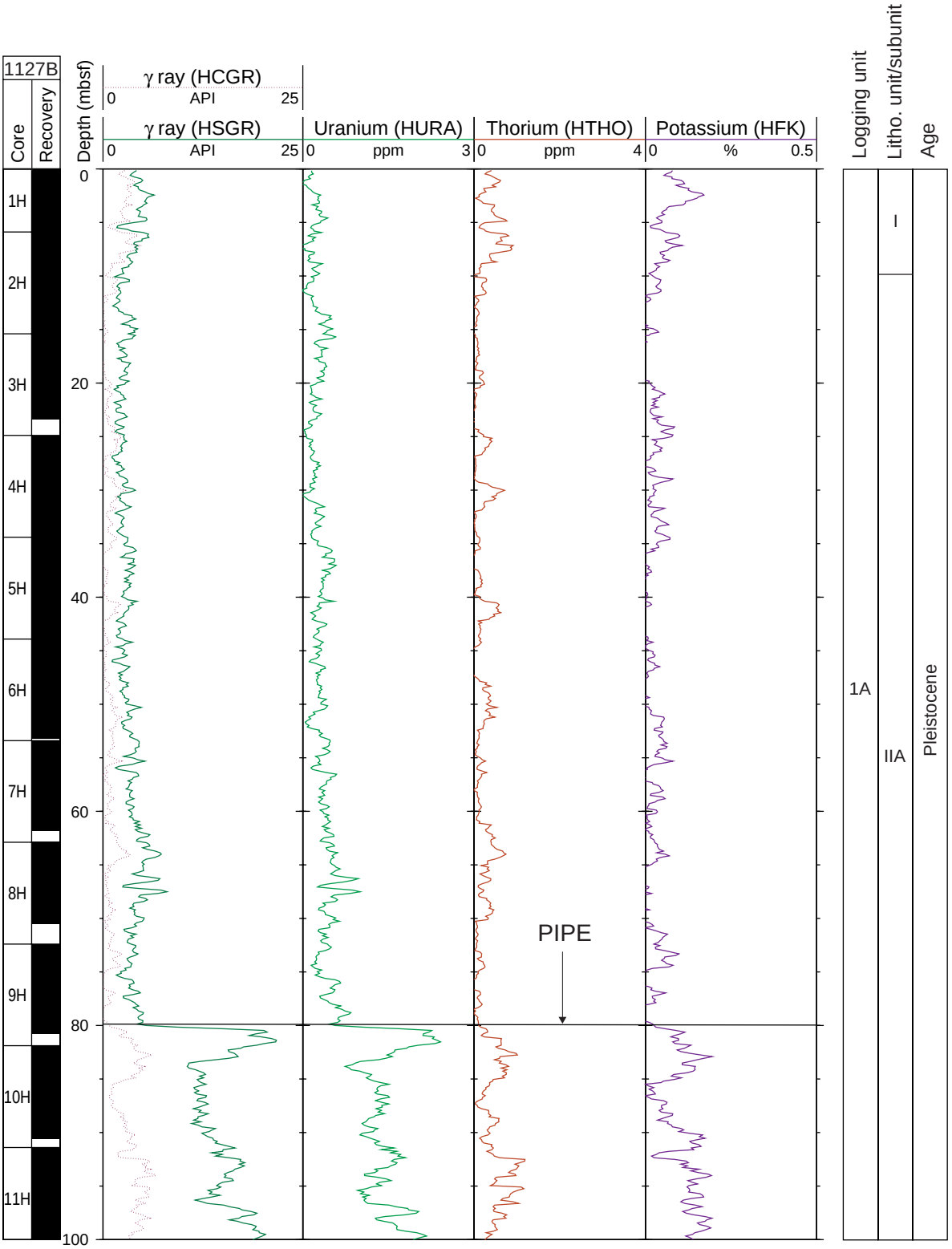

Figure F24. Summary of spectral gamma-ray logs from hostile environment natural gamma-ray sonde vs. depth for the open-hole logged interval. From left to right, columns are core recovery, total gamma radiation (HSGR) and computed (uranium-free) gamma radiation (HCGR), uranium, thorium, potassium and caliper, logging units, lithostratigraphic units, and biostratigraphic ages.

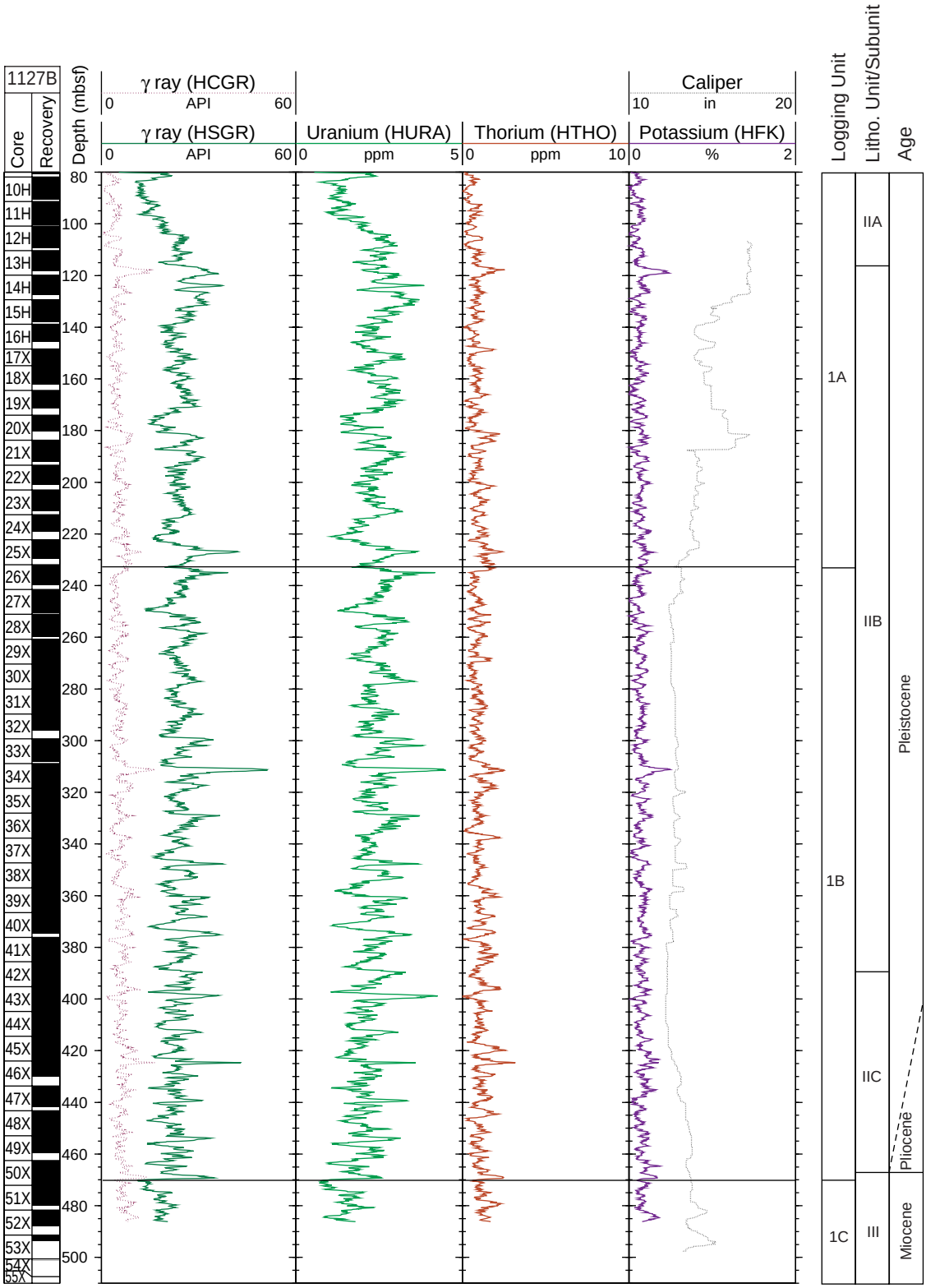

Figure F25. Summary of conventional geophysical logs vs. depth from the triple combination logging tool, Formation MicroScanner/sonic, and geologic high-resolution magnetic tool for the open-hole logged interval. From left to right, columns are core recovery; total gamma radiation (HSGR) and caliper; porosity; shallow, medium, and deep resistivity; sonic velocity; magnetic susceptibility; logging units; lithostratigraphic units; and biostratigraphic ages.

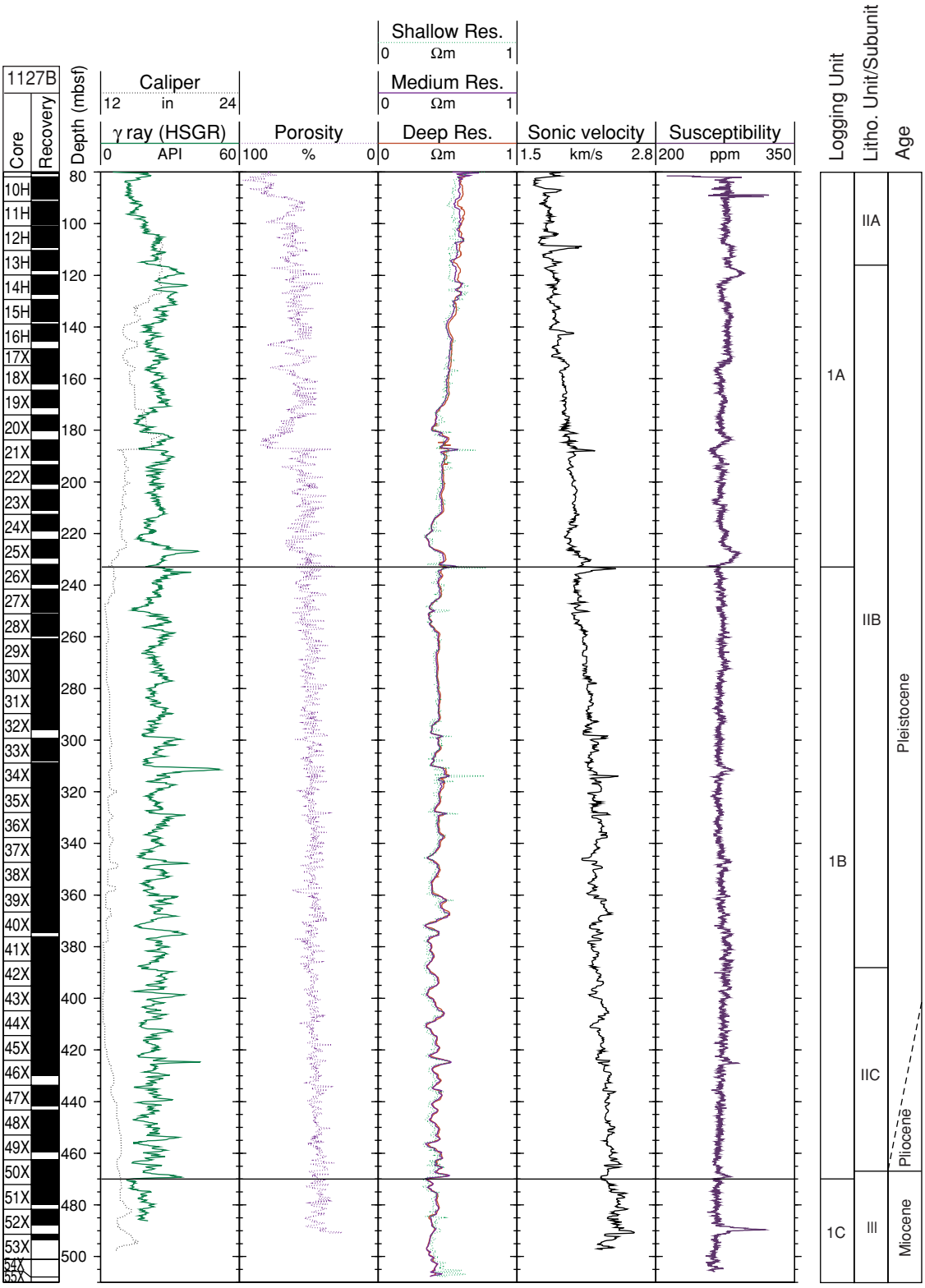

Figure F26. Formation MicroScanner image from logging Subunit 1B showing several zones of lithification expressed as resistive (bright) intervals. A highly resistive interval at 313–314 mbsf corresponds to a firmground within lithostratigraphic Unit IIB.

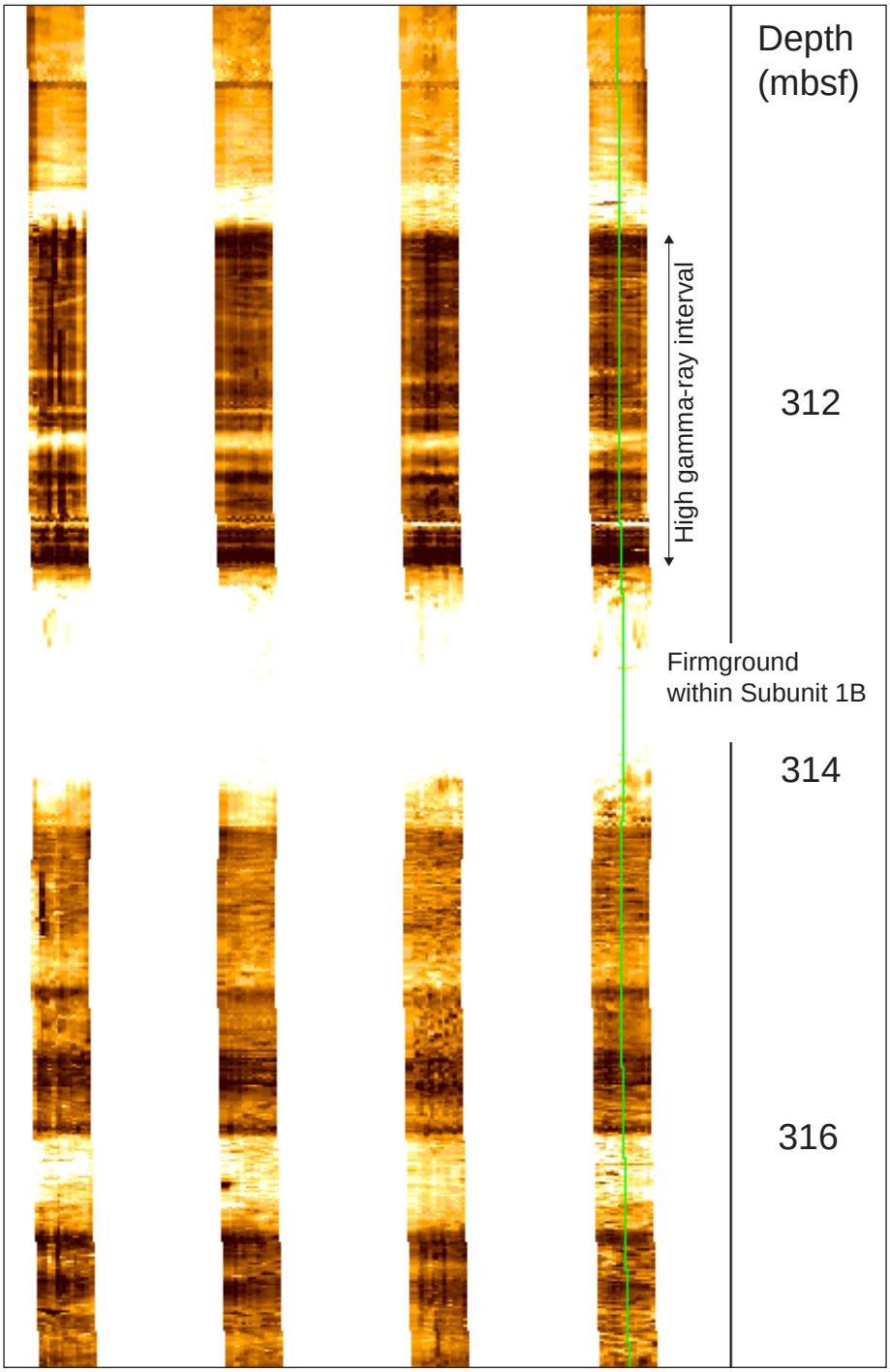

Figure F27. Formation MicroScanner image from lower part of logging Subunit 1B showing several highly conductive (dark) features interpreted as water-filled vugs in the borehole wall (428–429 mbsf). Individual features are 5–8 cm across.

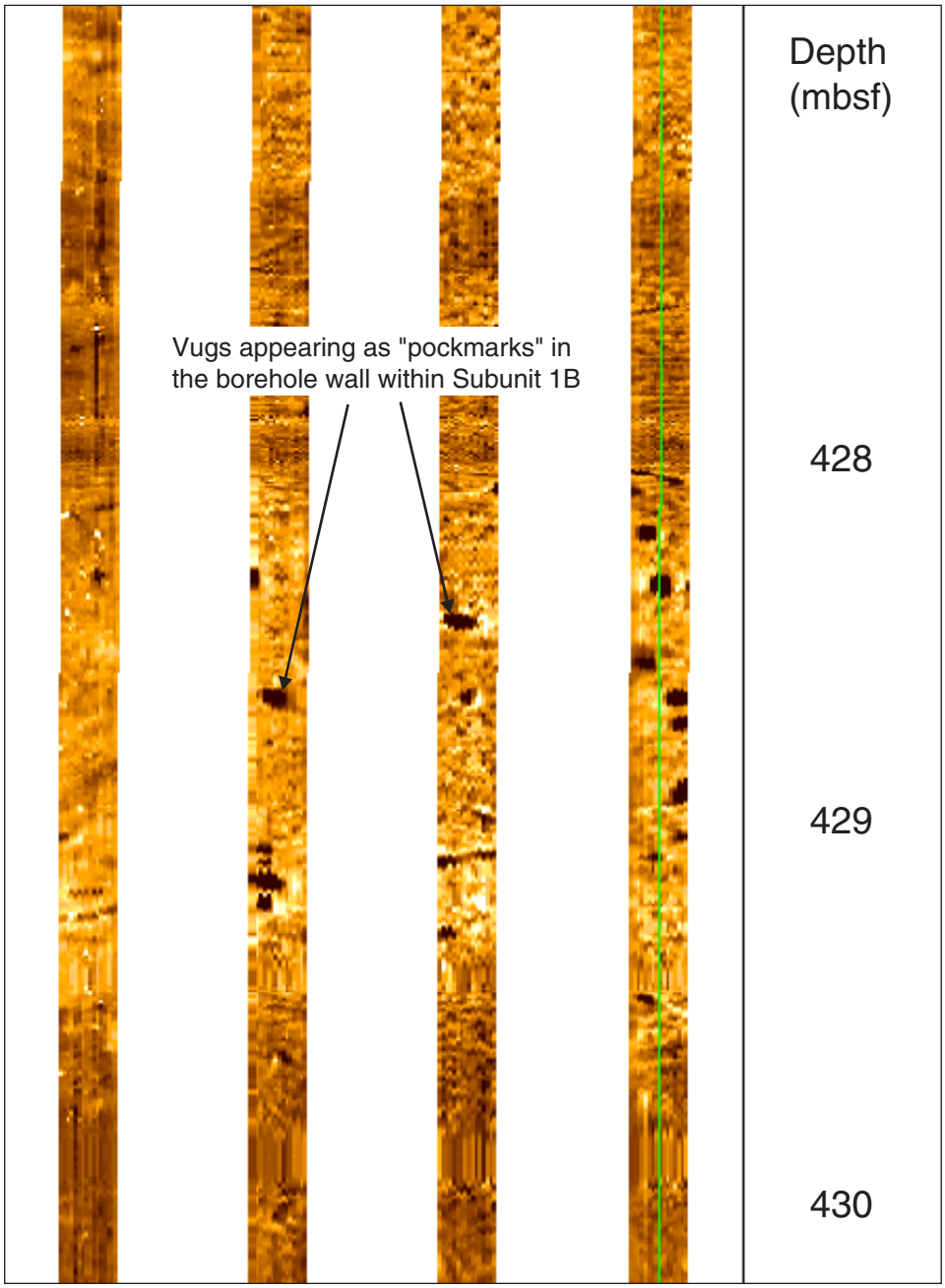

Figure F28. Downhole variations in borehole temperature measured by the Lamont-Doherty Earth Observatory high-resolution temperature/acceleration/pressure tool on the triple combination logging tool. Logging directions are indicated by arrows. Breaks in gradient may indicate changes in formation pressure, porosity, and/or permeability.

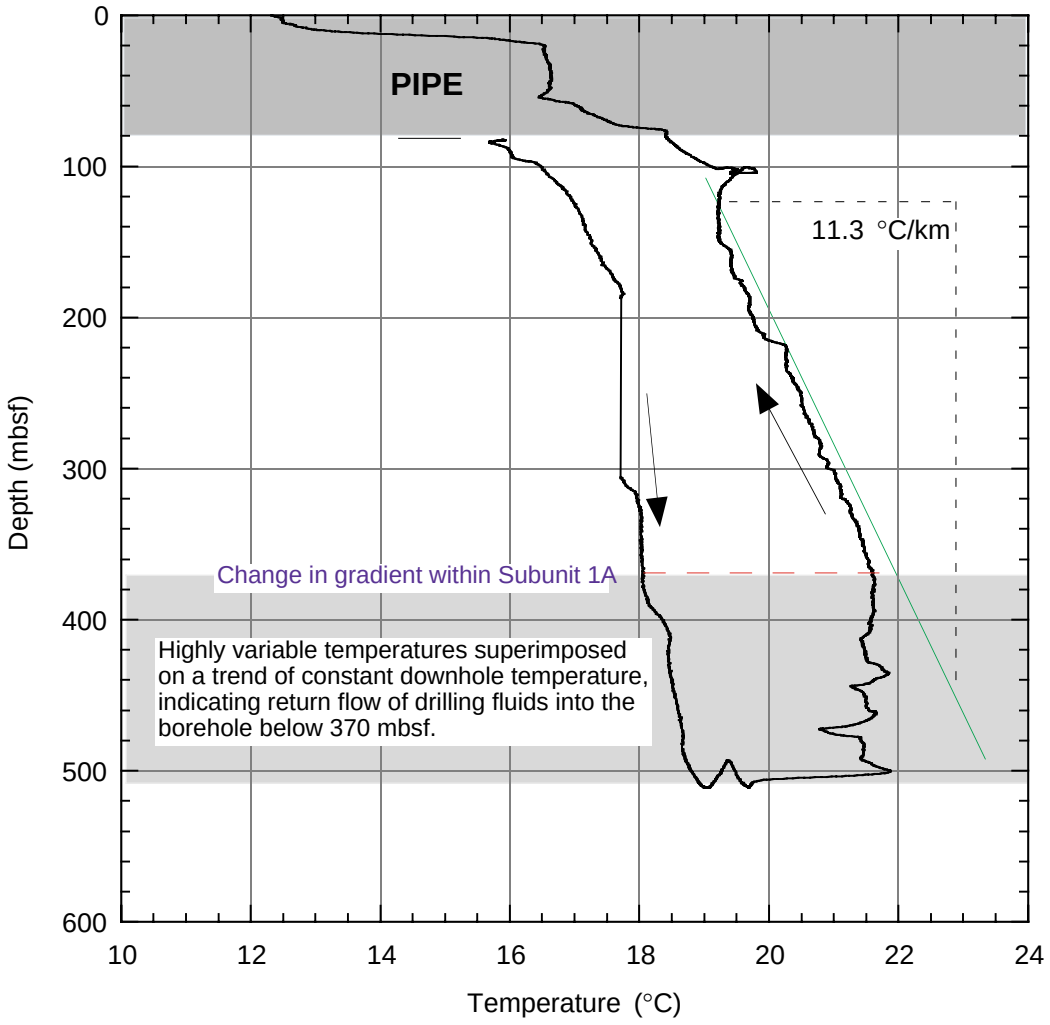

Figure F29. Map showing seismic site-survey tracks for Sites 1127, 1129, and 1131 (Line AGSO169/05) in relation to other Leg 182 sites and the Australian Geological Survey Organisation Survey 169 (AGSO169) site-survey seismic lines. The bold trackline (AGSO169/05a) corresponds to the seismic line segment shown in Figure F30, p. 60.

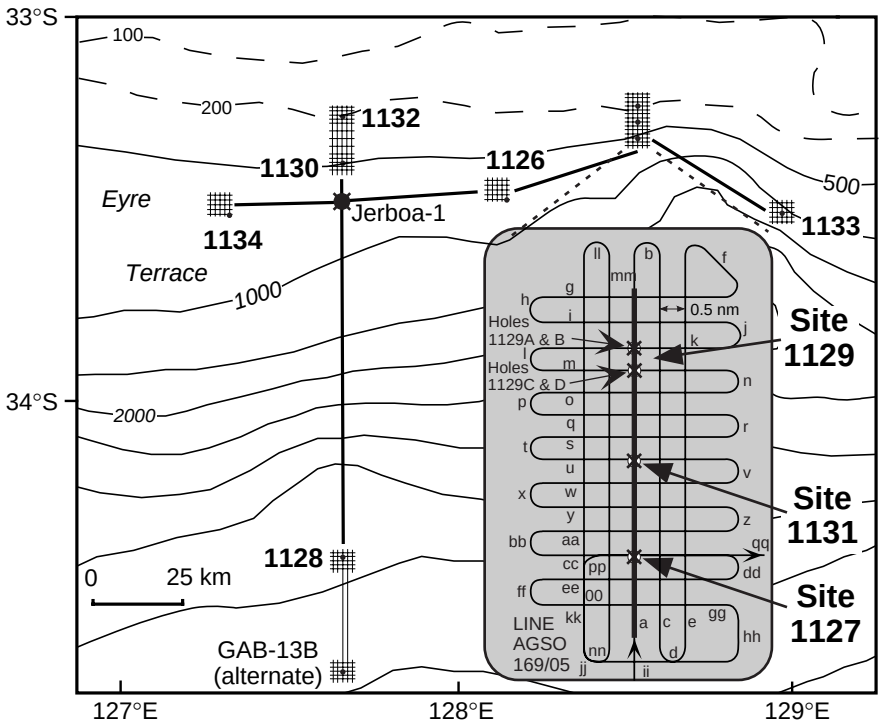

Figure F30. Portion of seismic Line AGSO169/05a showing interpreted seismic stratigraphic sequences planned (shown in white) and actually intersected (shown in black) at Sites 1127, 1129, and 1131.

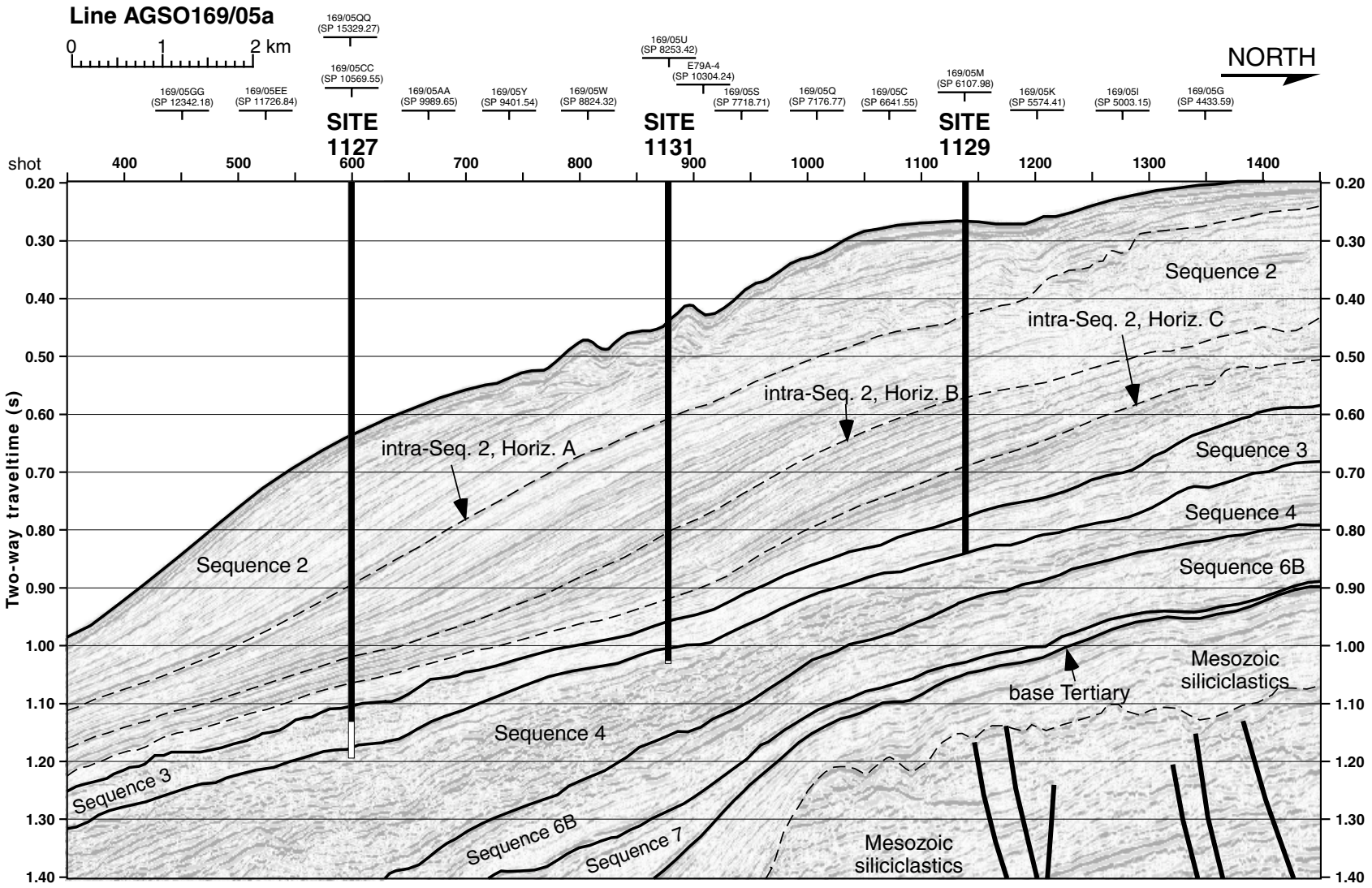

Figure F31. Check-shot stations and acquisition geometry for the well seismic tool (WST) survey at Hole 1129D, with corrected two-way–traveltimes (TWT) and derived interval velocities. GI = generator-injector; mbsl = meters below sea level; mbrf = meters below rig floor.

Depth (mbrf)	Depth (mbsl)	Transit time (ms)	True path length (m)	Corrected TWT (ms)	Interval velocity (ms)
368.0	356.1	221.24	356.7	442.22	1827.90
400.0	388.1	238.55	388.7	477.24	2027.76
440.1	428.2	258.11	428.8	516.79	2055.95
515.1	503.2	294.24	503.8	589.75	2121.92
580.2	568.3	324.78	568.9	651.11	2237.54
630.0	618.1	346.92	618.7	695.62	2435.08
680.2	668.3	367.43	668.9	736.85	2659.10
730.3	718.4	386.18	719.0	774.53	2470.65
759.9	748.0	398.11	748.6	798.49	2972.85
791.2	779.3	408.59	779.9	819.55	

Corrected TWT is TWT from sea level to WST tool along a vertical path

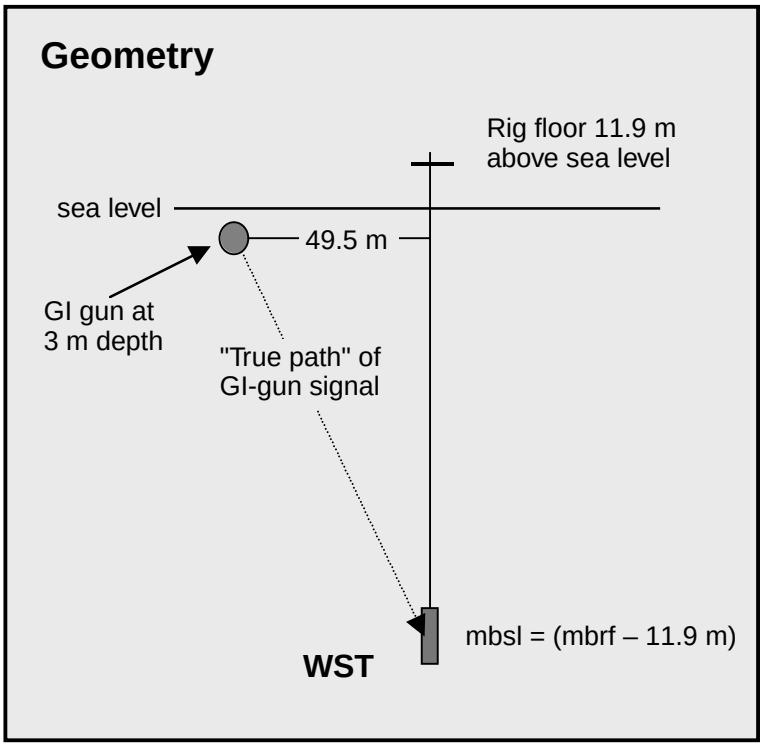

Figure F32. Check-shot stations and acquisition geometry for the well seismic tool (WST) survey at Hole 1131A, with corrected two-way–traveltimes (TWT) and derived interval velocities. GI = generator-injector; mbsl = meters below sea level; mbrf = meters below rig floor.

Depth (mbrf)	Depth (mbsl)	Transit time (ms)	True path length (m)	Corrected TWT (ms)	Interval velocity (ms)
490.2	478.5	302.15	478.9	605.08	1758.04
520.0	508.3	318.99	508.7	638.98	2087.78
550.1	538.4	333.31	538.8	667.81	2028.68
650.0	638.3	382.29	638.7	766.30	2138.07
750.0	738.3	428.88	738.7	859.84	2465.51
850.2	838.5	469.37	838.9	941.12	2434.49
880.2	868.5	481.66	868.9	965.77	2473.84
910.2	898.5	493.75	898.9	990.02	

Corrected TWT is TWT from sea level to WST tool along a vertical path

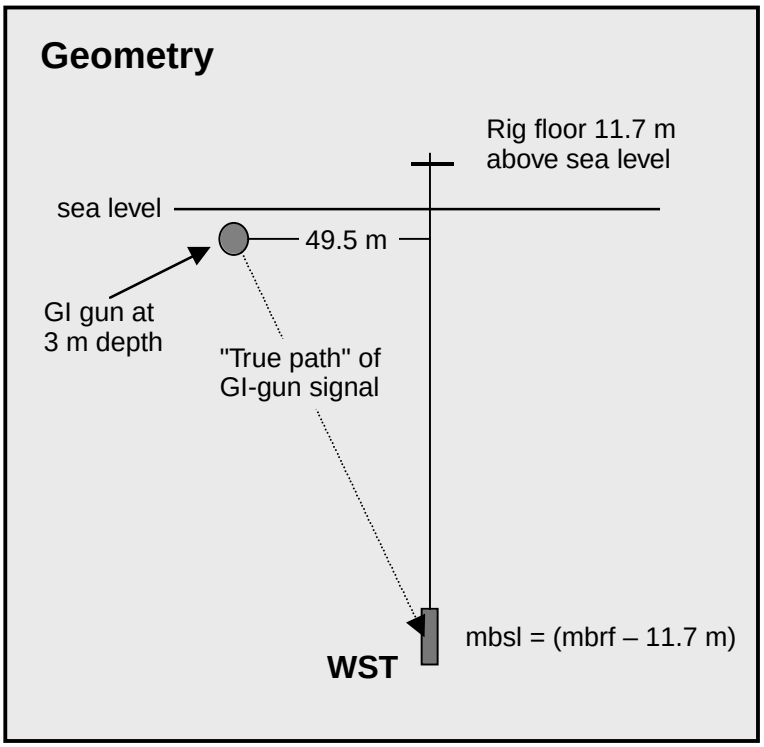

Figure F33. A. Plot showing relationship between predicted depths to key horizons and sequence boundaries (dashed) and corrected depths (arrowed) for Site 1127. Corrected depths are based on the integrated sonic log (derived from interval transit time data) shown plotted as a heavy dashed line relative to plots of site-survey seismic data stacking velocities. **B.** Plot of the velocity log (from compressional sonic trace) used as the basis for the integrated sonic log.

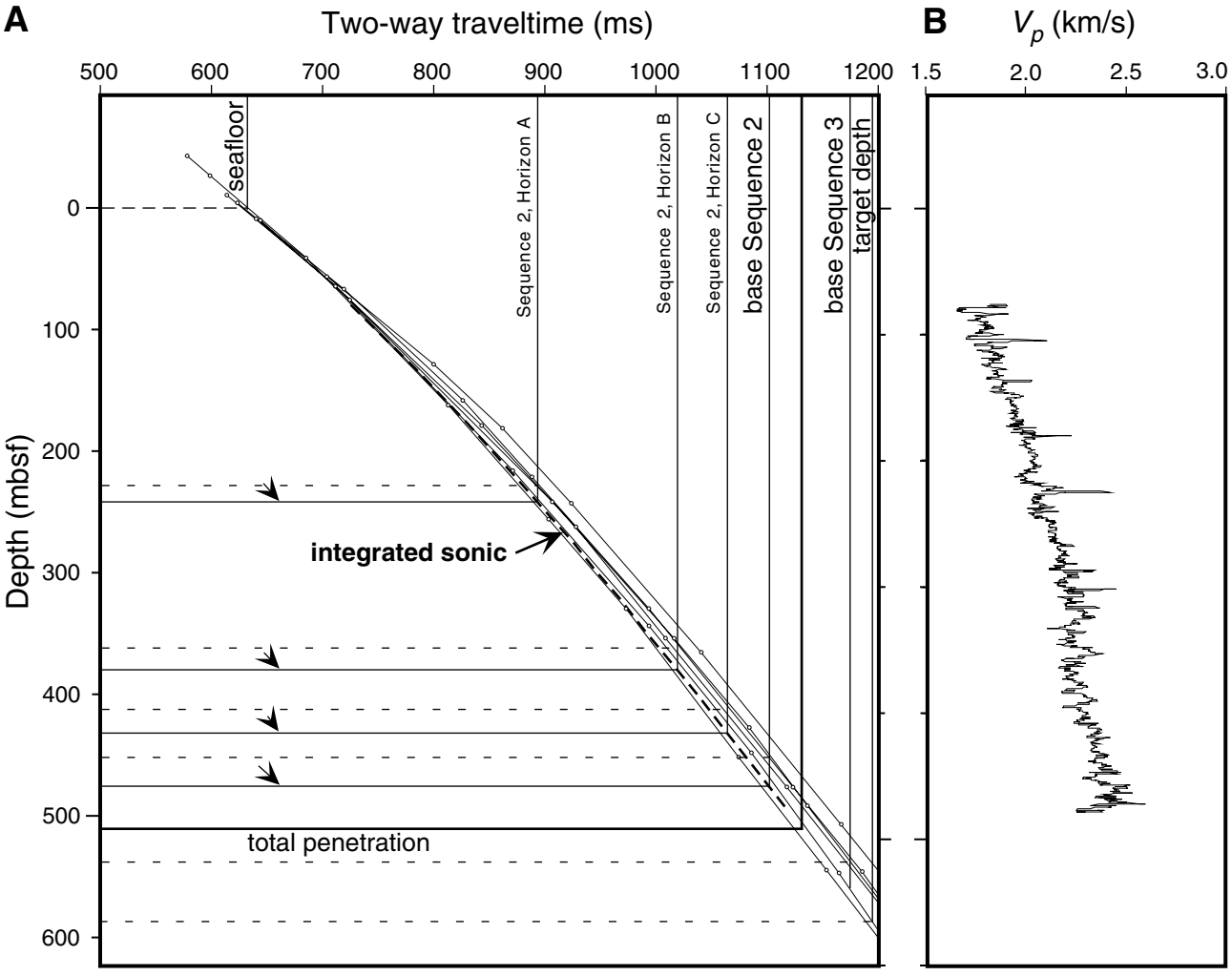

Figure F34. A. Plot showing relationship between predicted depths to key horizons and sequence boundaries (dashed) and corrected depths (arrowed) for Site 1129. Corrected depths are based on the check-shot survey data (heavy solid line), shown plotted toward the base of the envelope of stacking velocity curves derived from five common depth points of the site-survey seismic data immediately adjacent to this site (the sixth stacking velocity curve appears to be incorrect). The integrated sonic log, based on interval transit time data, is plotted as a heavy dashed line. **B.** Interval velocities derived from the 10 check-shot stations shown overlying the velocity log (derived from the compressional sonic trace).

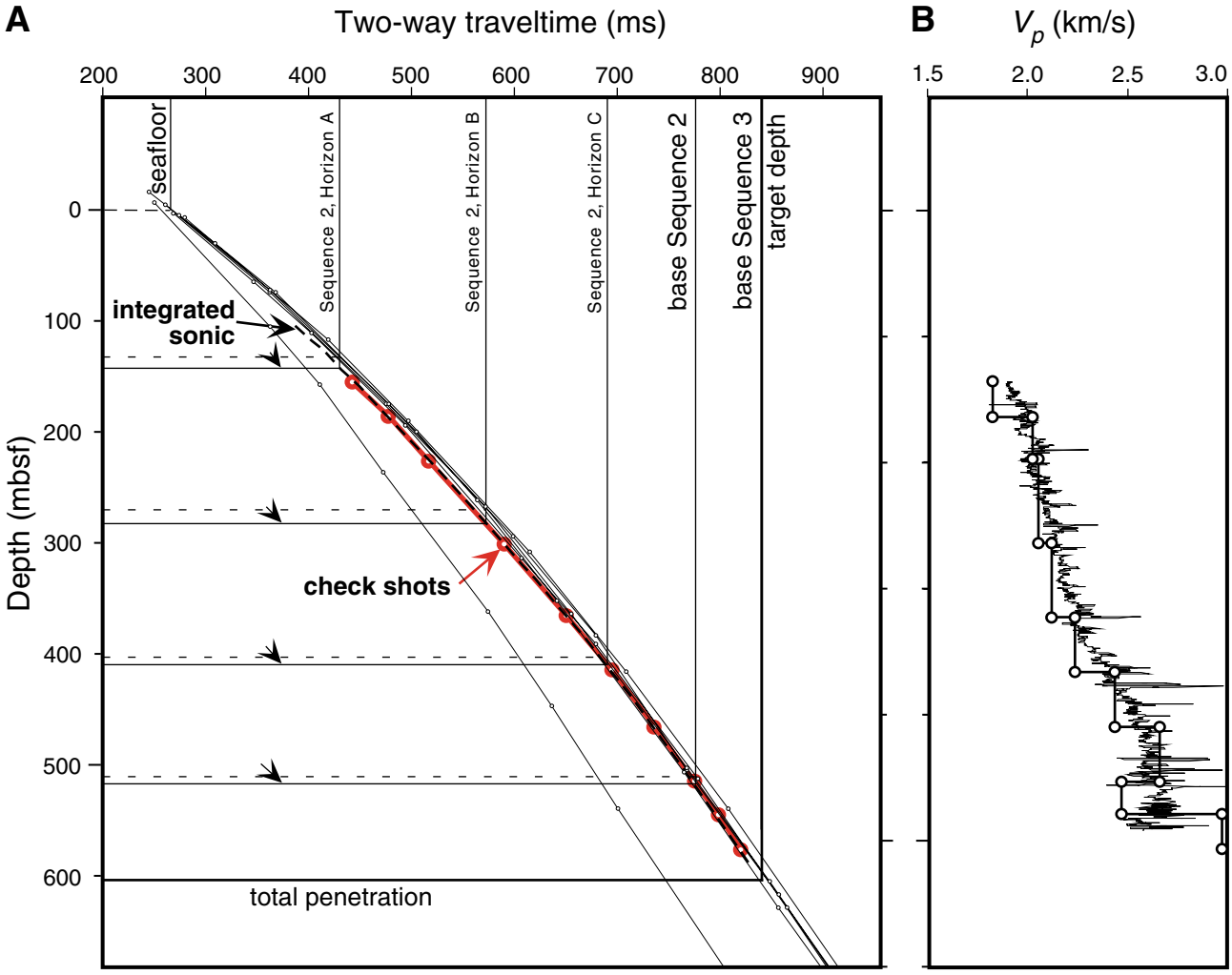

Figure F35. A. Plot showing relationship between predicted depths to key horizons and sequence boundaries (dashed) and corrected depths (arrowed) for Site 1131. Corrected depths are based on the check-shot survey data (heavy solid line), shown plotted at or immediately below the envelope of stacking velocity curves derived from six common depth points (CDPs) of the site-survey seismic data immediately adjacent to this site. The integrated sonic log, based on interval transit time data, is plotted as a heavy dashed line. **B.** Interval velocities derived from the eight check-shot stations shown overlying the velocity log (derived from the compressional sonic trace).

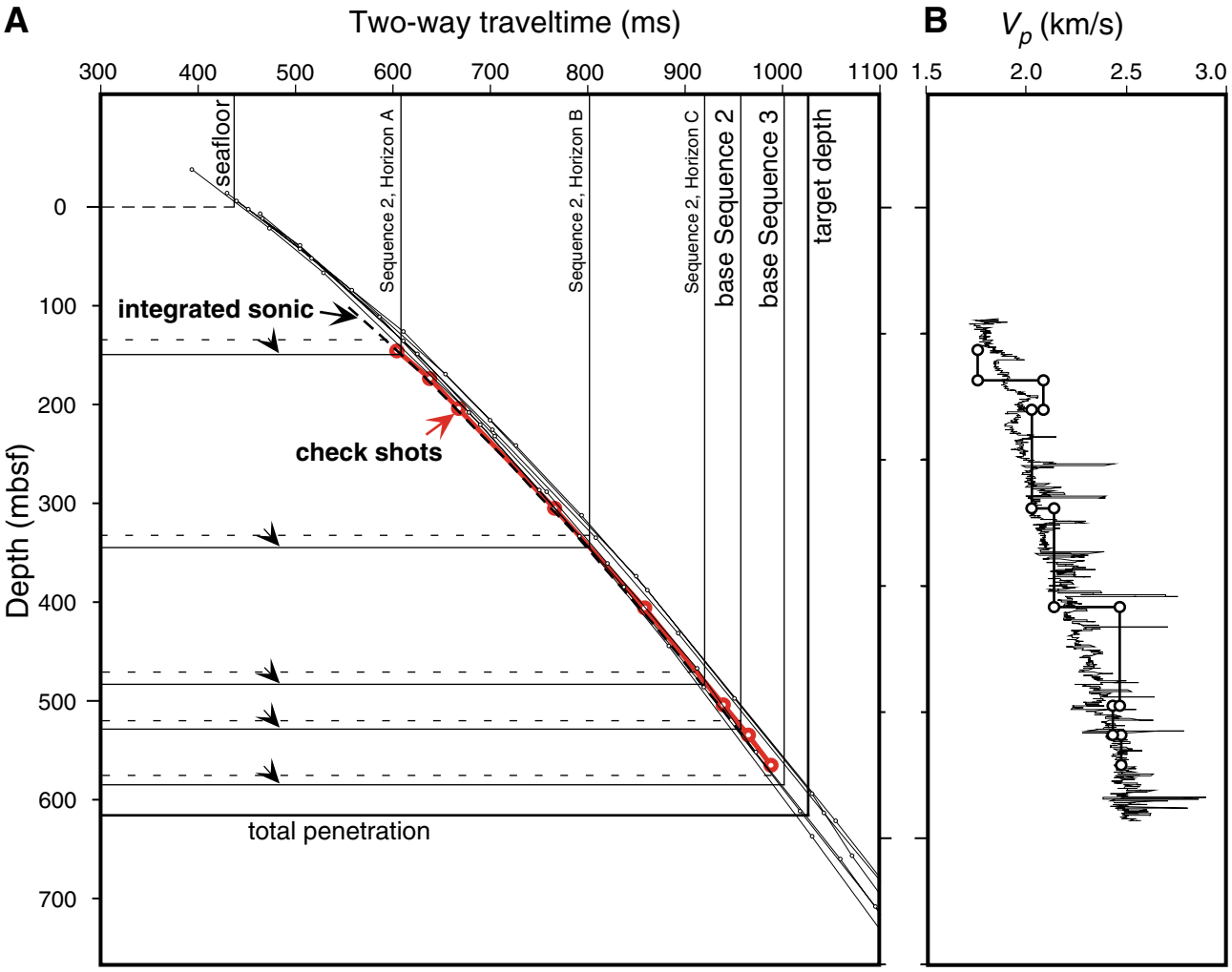

Figure F36. Tentative summary correlation between lithostratigraphic units, seismic sequences, biostratigraphic hiatuses, and ages at Site 1127.

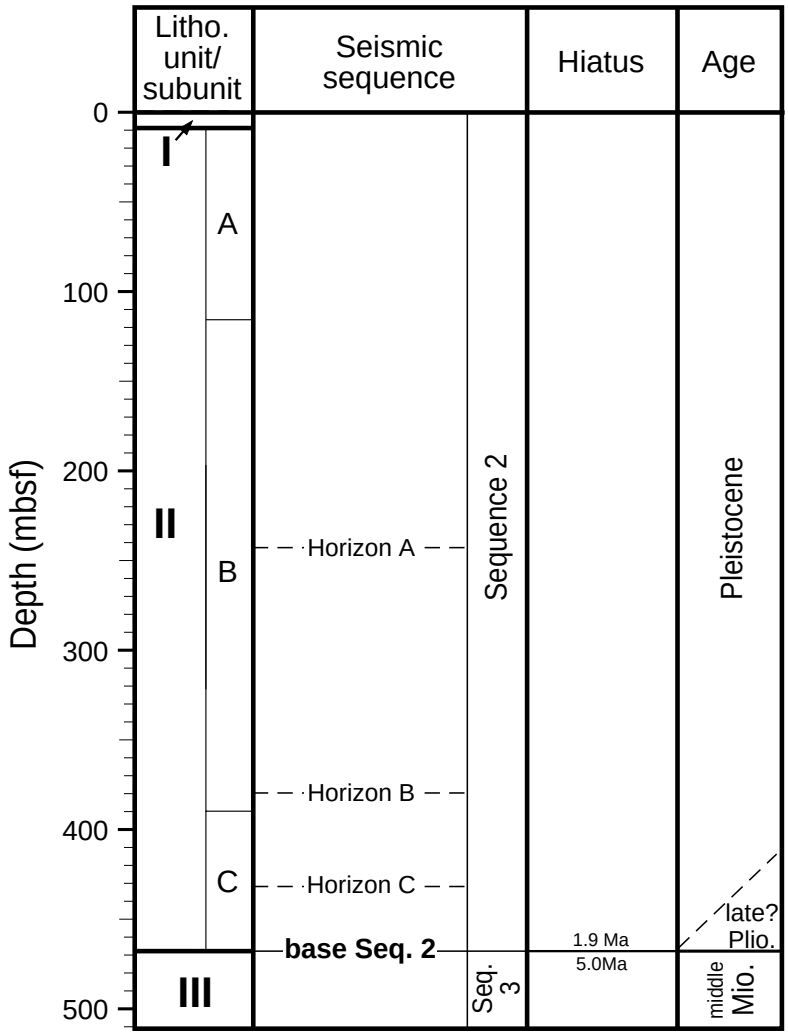

Figure F37. Tentative summary correlation between lithostratigraphic units, seismic sequences, biostratigraphic hiatuses, and ages at Site 1129.

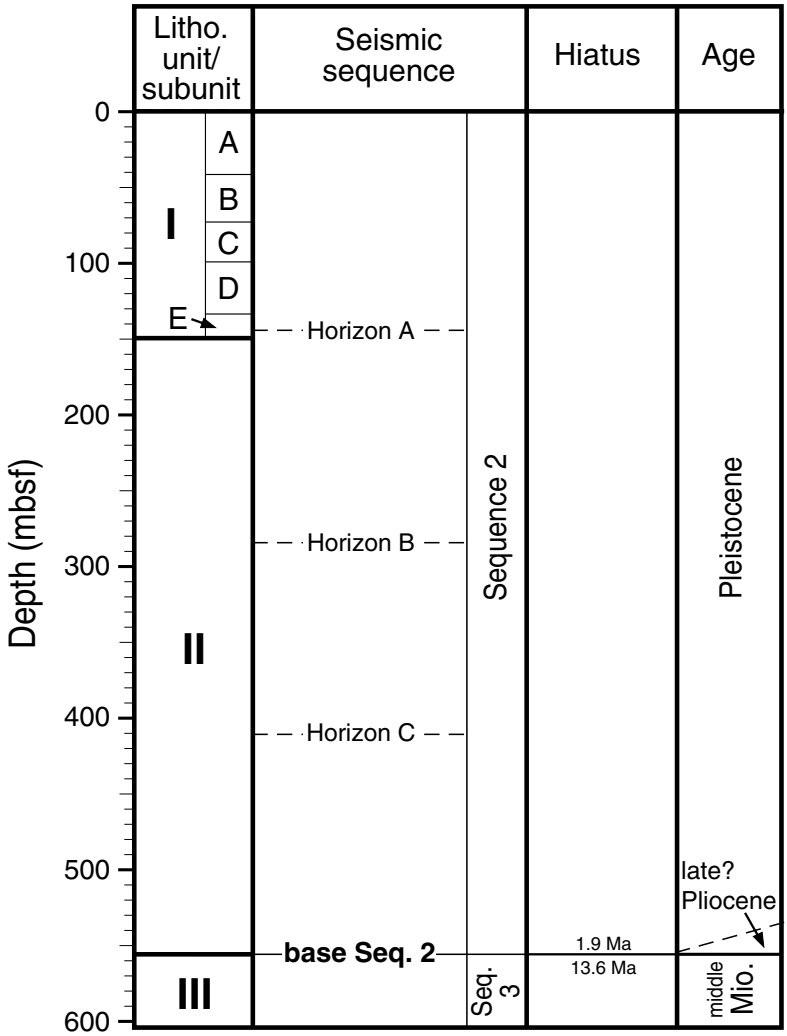

Figure F38. Tentative summary correlation between lithostratigraphic units, seismic sequences, biostratigraphic hiatuses, and ages at Site 1131. ? = seismic data show missing section corresponding to these surfaces, although biostratigraphic data provide no constraint on the length of missing time.

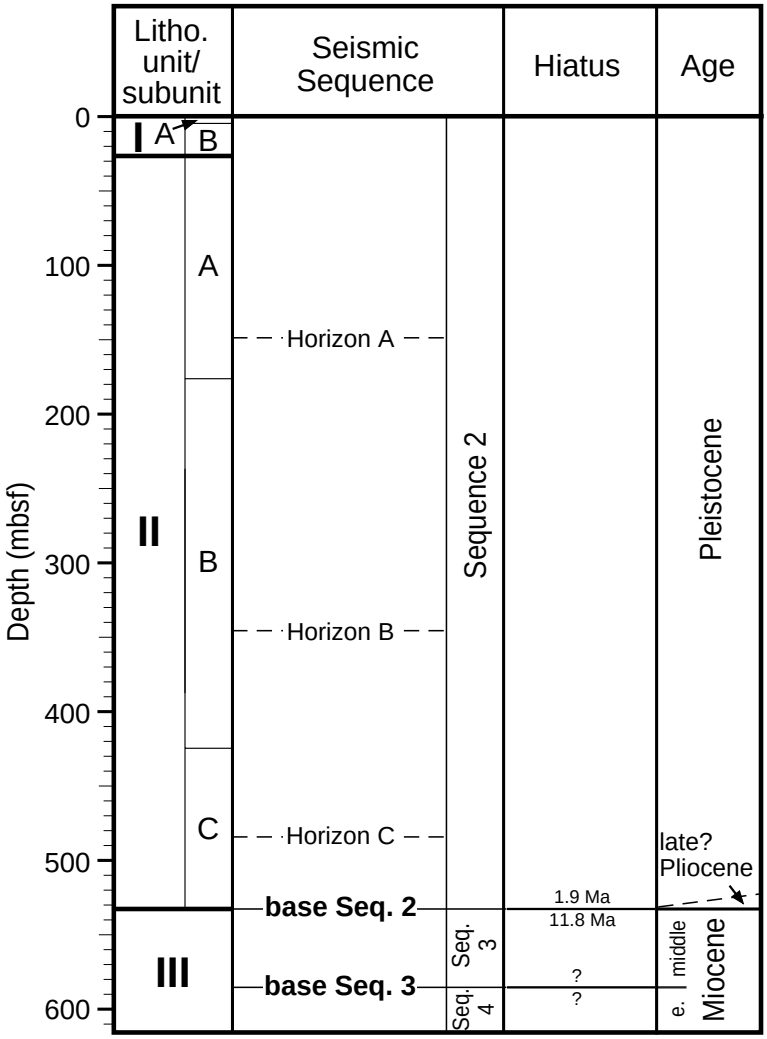

Table T1. Site 1127 coring summary. (See table note. Continued on next page.)

Hole 1127A

Latitude: –33.357428° (33°21.4457′S)
Longitude: 128.4813° (128°28.8780′E)
Seafloor (drill-pipe measurement from rig floor, mbrf): 490.0
Distance between rig floor and sea level (m): 11.3
Water depth (drill-pipe measurement from sea level, m): 478.7
Total depth (from rig floor, mbrf): 499.5
Penetration (mbsf): 9.5
Total number of cores: 1
Total length of cored section (m): 9.5
Total core recovered (m): 9.68
Core recovery (%): 101.9

Hole 1127B

Latitude: –33.357507° (33°21.4504′ South)
Longitude: 128.481275° (128°28.8765′ East)
Seafloor (drill-pipe measurement from rig floor, mbrf): 490.6
Distance between rig floor and sea level (m): 11.3
Water depth (drill-pipe measurement from sea level, m): 479.3
Total depth (from rig floor, mbrf): 1001.3
Penetration (mbsf): 510.7
Total number of cores: 55
Total length of cored section (m): 510.7
Total core recovered (m): 440.56
Core recovery (%): 86.27

Core	Date (1998)	Time (UTC + 8 hr)	Depth (mbsf)	Length cored (m)	Length recovered (m)	Recovery (%)	Comment
182-1127A-							
1H	30 Oct	2120	0.00-9.50	9.5	9.68	101.9	
Totals:				9.5	9.68	101.9	
182-1127B-							
1H	30 Oct	2145	0.00-5.90	5.9	5.86	99.3	H_2S
2H	30 Oct	2210	5.90-15.40	9.5	9.47	99.7	H_2S
3H	30 Oct	2245	15.40-24.90	9.5	7.95	83.7	H_2S; oriented
4H	30 Oct	2315	24.90-34.40	9.5	9.77	102.8	H_2S; oriented
5H	30 Oct	2345	34.40-43.90	9.5	9.49	99.9	H_2S; oriented
6H	31 Oct	0015	43.90-53.40	9.5	9.29	97.8	H_2S; oriented
7H	31 Oct	0350	53.40-62.90	9.5	8.41	88.5	H_2S
8H	31 Oct	0510	62.90-72.40	9.5	7.64	80.4	H_2S
9H	31 Oct	0620	72.40-81.90	9.5	8.39	88.3	H_2S
10H	31 Oct	0735	81.90-91.40	9.5	8.70	91.6	H_2S
11H	31 Oct	0910	91.40-100.90	9.5	8.91	93.8	H_2S
12H	31 Oct	1100	100.90-110.40	9.5	8.35	87.9	H_2S
13H	31 Oct	1230	110.40-119.90	9.5	7.82	82.3	H_2S
14H	31 Oct	1355	119.90-129.40	9.5	7.53	79.3	H_2S
15H	31 Oct	1515	129.40-138.90	9.5	8.55	90.0	H_2S
16H	31 Oct	1640	138.90-148.40	9.5	6.71	70.6	H_2S
17X	31 Oct	1815	148.40-154.90	6.5	6.83	105.1	H_2S
18X	31 Oct	2250	154.90-164.50	9.6	7.37	76.8	H_2S
19X	31 Oct	2340	164.50-174.10	9.6	6.94	72.3	H_2S
20X	1 Nov	0040	174.10-183.70	9.6	6.05	63.0	H_2S
21X	1 Nov	0205	183.70-193.40	9.7	8.24	85.0	H_2S
22X	1 Nov	0315	193.40-203.00	9.6	7.62	79.4	H_2S
23X	1 Nov	0430	203.00-212.60	9.6	8.20	85.4	H_2S
24X	1 Nov	0530	212.60-222.30	9.7	6.51	67.1	H_2S
25X	1 Nov	0645	222.30-231.90	9.6	7.53	78.4	H_2S
26X	1 Nov	0735	231.90-241.50	9.6	7.83	81.6	H_2S
27X	1 Nov	0815	241.50-251.10	9.6	8.99	93.7	H_2S
28X	1 Nov	0905	251.10-260.80	9.7	8.77	90.4	H_2S
29X	1 Nov	0945	260.80-270.40	9.6	10.03	104.5	H_2S
30X	1 Nov	1025	270.40-280.00	9.6	9.43	98.2	H_2S
31X	1 Nov	1100	280.00-289.70	9.7	9.78	100.8	H_2S
32X	1 Nov	1135	289.70-299.30	9.6	6.52	67.9	H_2S
33X	1 Nov	1210	299.30-308.90	9.6	8.78	91.5	H_2S
34X	1 Nov	1240	308.90-318.50	9.6	9.98	104.0	H_2S
35X	1 Nov	1315	318.50-328.10	9.6	9.86	102.7	H_2S
36X	1 Nov	1400	328.10-337.70	9.6	9.89	103.0	H_2S

Table T1 (continued).

Core	Date (1998)	Time (UTC + 8 hr)	Depth (mbsf)	Length cored (m)	Length recovered (m)	Recovery (%)	Comment
37X	1 Nov	1430	337.70-347.30	9.6	9.80	102.1	H_2S
38X	1 Nov	1510	347.30-357.00	9.7	9.89	102.0	H_2S
39X	1 Nov	1545	357.00-366.60	9.6	9.69	100.9	H_2S
40X	1 Nov	1620	366.60-376.20	9.6	7.99	83.2	H_2S
41X	1 Nov	1650	376.20-385.60	9.4	9.86	104.9	H_2S
42X	1 Nov	1730	385.60-395.20	9.6	9.86	102.7	H_2S
43X	1 Nov	1805	395.20-404.80	9.6	9.25	96.4	H_2S
44X	1 Nov	1840	404.80-414.40	9.6	9.74	101.5	H_2S
45X	1 Nov	1925	414.40-424.00	9.6	9.76	101.7	H_2S
46X	1 Nov	2005	424.00-433.70	9.7	5.89	60.7	H_2S
47X	1 Nov	2050	433.70-443.30	9.6	8.04	83.8	H_2S
48X	1 Nov	2130	443.30-452.90	9.6	9.74	101.5	H_2S
49X	1 Nov	2215	452.90-462.50	9.6	6.75	70.3	H_2S
50X	1 Nov	2255	462.50-472.10	9.6	9.78	101.9	H_2S
51X	1 Nov	2330	472.10-481.70	9.6	7.87	82.0	H_2S
52X	2 Nov	0010	481.70-491.40	9.7	6.27	64.6	H_2S
53X	2 Nov	0050	491.40-501.10	9.7	2.32	23.9	H_2S
54X	2 Nov	0205	501.10-507.70	6.6	0.01	0.2	
55X	2 Nov	0305	507.70-510.70	3.0	0.06	2.0	
Totals:				510.7	440.56	86.3	

Note: UTC = Universal Time Coordinated.

Table T2. Datum levels used for the calculation of the Site 1127 sedimentation rate.

Datum type	Datum level	Age (Ma)	Midpoint (mbsf)	Stratigraphic error (m)	Fossil group	Datum level code	Upper sample		Lower sample	
							Core, section, interval (cm)	Depth (mbsf)	Core, section, interval (cm)	Depth (mbsf)
							182-1127B-		182-1127B-	
B	*Emiliania huxleyi*	0.25	19.33	3.99	1	1	2H-CC, 12-15	15.34	3H-CC, 17-20	23.32
T	*Pseudoemiliania lacunosa*	0.45	158.75	3.52	1	2	17X-CC, 23-26	155.20	18X-CC, 29-32	162.24
T	*Globorotalia tosaensis*	0.65	234.78	4.95	4	3	25X-CC, 29-31	229.81	26X-CC, 67-70	239.70
T	*Reticulofenestra asanoi*	0.88	284.8	4.975	1	4	30X-CC, 13-16	279.80	31X-CC, 36-39	289.75
B	*Reticulofenestra asanoi*	1.08	313.33	5.325	1	5	33X-CC, 29-32	308.00	34X-CC, 43-46	318.65
	Brunhes/Matuyama	0.78	343.4			A				
T	*Calcidiscus macintyrei*	1.67	352.32	4.85	1	6	37X-CC, 36-39	347.47	38X-CC, 31-34	357.16
T	Jaramillo	0.99	380.7			B				
B	Jaramillo	1.07	394	3.5		C	42X-5, 20-21	393	42X-5, 120-121	395
B	*Globorotalia truncatulinoides*	2	422.71	1.425	4	7	45X-5, 89-94	421.29	45X-CC, 28-30	424.14
B	*Globorotalia inflata*	2.09	463.28	3.66	4	8	49X-CC, 34-37	459.62	50X-3, 144-146	466.94
T	*Zeaglobigerina nepenthes*	4.2	469.92	2.36	4	9	50X-4, 54-56	467.54	50X-CC, 32-35	472.25
T	*Globquadrina dehiscens*	5.8	483.97	4	4	10	51X-CC, 30-33	479.94	52X-CC, 20-23	487.94
T	*Sphenolithus heteromorphus*	13.6	504.43	3.32	1	11	54X-CC, 0-1	501.10	55X-CC, 5-6	507.75

Notes: T = top of taxon stratigraphic range, B = bottom of taxon stratigraphic range. Midpoint = the middle depth between the sample where the taxon occurs and the adjacent sample where it does not occur. Stratigraphic error = one-half the distance between the sample where the taxon occurs and the adjacent sample where it does not occur. Datum level code = the number assigned to the datum level on Figure **F6,** p. 36. Fossil groups = calcareous nannofossils (1) and planktonic foraminifers (4).

Table T3. Composition of vacutainer gases, Hole 1127B.

Core, section	Depth (mbsf)	CO_2 (ppmv)	H_2S (ppmv)	C_1 (ppmv)	C_2 (ppmv)	C_3 (ppmv)	*i*-C_4 (ppmv)	C_5 (ppmv)	C_6 (ppmv)	C_1/C_2
182-1127B-										
6H-3	46.90	277,949	94,937	585,009						
7H-2	54.90	169,295	59,447	387,304						
7H-4	57.90	262,628	91,600	531,866						
8H-4	67.90	283,876	97,016	551,624						
9H-4	77.06	334,800	109,896	556,882						
10H-5	87.75	291,436	101,255	536,630						
11H-4	96.40	326,350	104,866	569,434						
12H-4	106.13	342,884	112,507	545,548						
13H-4	115.13	328,965	105,052	570,472						
14H-4	124.31	405,637	126,275	466,030				14		
15H-5	135.16	401,384	123,085	466,531				15		
16H-4	143.90	419,256	128,558	484,810				23		
17X-3	151.90	348,578	109,679	439,719				18		
18X-3	158.40	345,695	106,518	470,648				21		
19X-3	168.00	327,997	99,460	418,224				19		
20X-3	177.60	360,728	106,359	426,733				17		
21X-3	186.91	298,960	95,168	329,045				18		
22X-3	196.90	268,553	84,546	399,503				16		
23X-3	206.50	228,893	81,714	438,417		11		26		
24X-4	217.60	437,103	124,037	423,977				67		
25X-4	227.42	513,221	127,612	333,799	299			67		1,116
26X-5	238.05	379,060	118,178	476,180		16		66		
27X-4	246.34	478,422	121,776	371,166	363			64		1,023
28X-3	255.38	424,630	111,750	443,548	492	17		57		902
29X-3	264.80	352,729	102,433	517,528	587	23		45		882
30X-3	274.40	504,993	125,966	349,526	428	21		61		817
31X-4	284.91	496,944	129,241	340,323	401	18		61	14	848
32X-3	293.07	479,152	138,027	352,416	429	18		65		821
33X-3	303.00	460,948	118,927	389,729	564	34		30		691
34X-2	311.61	449,751	121,214	389,831	605	42	13	19		644

Note: ppmv = parts per million by volume, blank = not detected.

Table T4. Composition of headspace gas in sediment, Hole 1127B.

Core, section	Depth (mbsf)	H_2S (ppmv)	C_1 (ppmv)	C_2 (ppmv)	C_3 (ppmv)	C_5 (ppmv)	C_1/C_2
182-1127B-							
1H-4	4.50		3				
2H-5	11.90		173				
3H-5	21.40		4,109				
4H-6	31.30		17,222				
5H-5	40.40		46,234	1			66,048
6H-5	49.90	10,781	9,458				
7H-4	57.90	21,338	11,606				
8H-4	67.40		6,634		1		
9H-4	76.90		8,153				
10H-5	86.80		7,408				
11H-4	95.90		2,999				
12H-4	104.60		2,339				
13H-4	114.80		1,285				
14H-4	123.60		925				
15H-4	133.20		1,413				
16H-3	141.90		3,254				
17X-3	151.40	99	1,890				
18X-3	157.90		885				
19X-4	169.00		2,460				
20X-3	177.10	6,876	4,895				
21X-5	189.40	13,272	3,410			17	
22X-3	196.40	141	6,302	1			6,302
23X-3	206.00	12,562	8,244	1		14	7,494
24X-4	217.10		7,451	1			8,279
25X-5	229.50		1,997				
26X-5	239.00		2,307	1			2,564
27X-5	249.00		10,916	2			4,962
28X-4	255.60		8,707	2			4,583
29X-6	269.10		5,090	2	1		2,679
30X-4	274.90		6,849	2	1		2,978
31X-7	289.30		2,668	2			1,570
32X-5	295.90		11,873	5	2		2,526
33X-4	303.80		18,328	9	4		1,992
34X-7	318.20		7,012	7	4		1,079
35X-7	327.90		1,623	3	2		624
36X-4	332.60	28,218	6,964	7	3		995
37X-7	347.10	4,026	5,639	8	1		714
38X-7	356.80	27,473	8,036	11	3		737
39X-4	361.50	257	8,210	15	5		562
40X-6	374.30		3,234	9	3		363
41X-7	385.70		3,804	13	4		302
42X-7	395.10		4,868	17	4		285
43X-4	399.70	8,762	4,323	18	5		246
44X-7	414.20		773	5	2		143
45X-7	423.80		1,494	10	3		145
46X-3	427.00	68	1,382	8	2		165
47X-6	441.30	1,140	1,561	12	3		126
48X-7	452.70		1,192	12	4		100
49X-3	455.90	39	1,015	9	2		114
50X-4	467.00		392	5	2		82
51X-4	476.60		495	4	1		115
52X-3	484.70	298	910	7	1		130

Note: ppmv = parts per million by volume, blank = not detected.

Table T5. Carbon, nitrogen, and sulfur data, Hole 1127B. (See table note. Continued on next two pages.)

Core, section, interval (cm)	Depth (mbsf)	C_{inorg} (wt%)	$CaCO_3$ (wt%)	Total carbon (wt%)	C_{org} (wt%)	Nitrogen (wt%)	Sulfur (wt%)
182-1127B-							
1H-1, 48-50	0.48	10.48	87.3	10.75	0.27	0.07	
1H-3, 48-50	3.48	10.53	87.7	11.21	0.68	0.11	
2H-1, 49-50	6.39	10.22	85.1	11.09	0.87	0.14	0.11
2H-3, 49-50	9.39	10.97	91.4	11.39	0.42	0.06	0.11
2H-5, 49-50	12.39	11.03	91.9	11.60	0.57	0.07	
3H-1, 49-50	15.89	10.92	90.9	11.41	0.49	0.07	0.10
3H-3, 49-50	18.89	10.89	90.7	11.32	0.43	0.06	0.14
3H-5, 49-50	21.89	10.83	90.2	11.22	0.39	0.06	
4H-1, 49-50	25.39	10.98	91.4	11.15	0.17	0.05	
4H-3, 49-50	27.32	10.89	90.7	11.28	0.39	0.06	
4H-5, 49-50	30.32	11.00	91.6	11.49	0.49	0.07	
5H-3, 49-50	37.89	10.79	89.8	11.20	0.41	0.07	
5H-5, 49-50	40.89	10.89	90.7	11.10	0.21	0.06	
6H-1, 49-50	44.39	10.73	89.3	10.97	0.24	0.07	0.01
6H-3, 49-50	47.39	10.86	90.5	11.14	0.28	0.05	
6H-5, 49-50	50.39	10.99	91.5	11.21	0.22	0.05	
7H-1, 49-50	53.89	10.75	89.6	10.94	0.19	0.06	
7H-3, 49-50	56.89	10.48	87.3	10.74	0.26	0.05	
7H-5, 49-50	59.89	10.31	85.8	10.74	0.43	0.07	
8H-1, 49-50	63.39	9.89	82.4	10.45	0.56	0.09	0.11
8H-3, 49-50	66.39	11.13	92.7	11.30	0.17	0.04	
8H-5, 49-50	69.39	11.09	92.4	11.53	0.44	0.06	
9H-1, 49-50	72.89	11.01	91.7	11.22	0.21	0.04	
9H-3, 49-50	75.89	10.75	89.5	11.66	0.91	0.07	
9H-5, 49-50	78.82	10.75	89.6	10.89	0.14		
10H-3, 49-50	84.28	10.84	90.3	11.20	0.36	0.05	
10H-5, 49-50	87.28	10.81	90.0	10.95	0.14		
11H-1, 49-50	91.89	10.47	87.2	10.76	0.29	0.05	
11H-3, 49-50	94.89	10.70	89.2	11.23	0.53	0.05	
11H-5, 49-50	97.87	10.81	90.0	11.49	0.68	0.06	
12H-1, 49-50	101.39	10.94	91.1	11.39	0.45	0.06	
12H-3, 49-50	103.63	10.75	89.5	11.30	0.55	0.05	
12H-5, 49-50	106.63	10.49	87.4	10.90	0.41	0.05	
13H-1, 49-50	110.89	10.56	87.9	10.67	0.11		
13H-3, 49-50	113.89	9.87	82.2	10.45	0.58	0.09	
13H-5, 49-50	116.61	10.80	90.0	11.22	0.42	0.06	
14H-1, 49-50	120.39	11.07	92.2	11.12	0.05		
14H-3, 49-50	122.54	11.03	91.9	11.13	0.10	0.04	0.20
14H-5, 49-50	125.54	10.90	90.8	11.08	0.18	0.04	
15H-1, 49-50	129.89	10.95	91.2	11.07	0.12	0.05	
15H-3, 49-50	132.15	10.72	89.3	10.97	0.25	0.05	
15H-5, 49-50	135.15	10.92	91.0	10.80		0.05	
16H-1, 49-50	139.39	10.94	91.2	11.01	0.07	0.05	
16H-3, 49-50	142.39	10.93	91.0	11.13	0.20	0.05	
17X-1, 49-50	148.89	10.90	90.8	11.27	0.37	0.06	
17X-3, 48-49	151.88	10.87	90.5	11.33	0.46	0.05	
17X-5, 49-50	154.72	10.72	89.3	11.10	0.37	0.05	
18X-1, 49-50	155.39	10.77	89.7	11.13	0.36	0.05	
18X-3, 49-50	158.39	10.77	89.7	11.31	0.54	0.07	
18X-5, 49-50	161.39	10.60	88.3	11.28	0.68	0.06	
19X-1, 49-50	164.99	10.59	88.2	11.03	0.44	0.06	
19X-3, 49-50	167.99	10.63	88.5	11.07	0.44	0.06	
19X-5, 49-50	170.99	10.53	87.7	10.84	0.31	0.05	
20X-1, 49-50	174.59	10.76	89.6	10.90	0.14		
20X-3, 49-50	177.59	10.47	87.2	10.50	0.03	0.04	
21X-1, 50-51	184.2	11.24	93.6	11.23		0.03	
21X-3, 49-50	186.9	10.68	89.0	11.19	0.51		
21X-5, 48-49	189.89	10.70	89.2	11.18	0.48	0.06	
22X-1, 49-50	193.89	10.64	88.6	11.05	0.41	0.06	
22X-3, 49-50	196.89	10.62	88.4	11.08	0.46	0.06	
22X-5, 49-50	199.89	10.69	89.0	11.04	0.35	0.05	
23X-1, 49-50	203.49	10.66	88.8	11.10	0.44	0.05	
23X-3, 49-50	206.49	10.79	89.9	11.02	0.23	0.06	
23X-5, 49-50	209.49	10.67	88.9	10.96	0.29	0.05	
24X-1, 49-50	213.09	10.80	90.0	11.07	0.27		
24X-3, 49-50	216.09	10.71	89.2	10.72	0.01	0.05	

Table T5 (continued).

Core, section, interval (cm)	Depth (mbsf)	C_{inorg} (wt%)	$CaCO_3$ (wt%)	Total carbon (wt%)	C_{org} (wt%)	Nitrogen (wt%)	Sulfur (wt%)
25X-1, 49-50	222.79	10.64	88.7	10.79	0.15	0.06	
25X-3, 49-50	225.79	10.44	86.9	10.82	0.38	0.07	
25X-5, 49-50	228.79	10.47	87.2	10.79	0.32	0.07	
26X-1, 49-50	232.39	10.77	89.7	10.98	0.21	0.05	
26X-3, 49-50	235.39	11.02	91.8	11.37	0.35	0.07	
26X-5, 49-50	238.39	10.63	88.6	11.05	0.41	0.06	
27X-1, 49-50	241.99	10.70	89.1	11.14	0.44	0.06	
27X-3, 49-50	244.99	10.26	85.5	10.91	0.65		0.29
27X-5, 49-50	247.99	10.92	91.0	11.30	0.38		0.17
28X-1, 49-50	251.59	10.71	89.2	11.52	0.81		0.37
28X-3, 49-50	254.59	10.65	88.7	11.16	0.51	0.05	0.23
28X-5, 49-50	257.59	10.86	90.4	11.70	0.84		
29X-1, 49-50	261.29	11.17	93.0	12.20	1.03		0.22
29X-3, 49-50	264.29	10.93	91.1	11.80	0.87	0.07	0.11
29X-5, 49-50	267.29	10.65	88.7	11.80	1.15		0.29
29X-7, 50-51	269.65	10.77	89.7	11.70	0.93	0.10	0.34
30X-1, 49-50	270.89	10.59	88.2	11.50	0.91	0.08	0.14
30X-3, 49-50	273.89	10.86	90.5	11.70	0.84	0.07	0.17
30X-5, 49-50	276.89	10.79	89.9	11.50	0.71	0.00	0.28
31X-1, 49-50	280.49	10.81	90.0	11.60	0.79	0.07	0.28
31X-3, 48-49	283.48	10.82	90.2	11.60	0.78	0.06	0.23
31X-5, 49-50	286.49	10.68	89.0	11.70	1.02	0.07	0.16
32X-1, 49-50	290.19	11.25	93.7	11.60	0.35		
32X-3, 50-51	293.2	11.02	91.8	11.50	0.48		
33X-1, 49-50	299.79	10.98	91.4	11.70	0.72	0.06	0.20
33X-3, 49-50	302.79	10.64	88.7	11.60	0.96	0.07	0.43
33X-5, 49-50	305.79	10.88	90.6	11.40	0.52		
34X-1, 49-50	309.39	10.23	85.2	11.30	1.07	0.06	0.15
34X-3, 49-50	312.39	10.75	89.5	11.30	0.55	0.04	0.35
34X-5, 49-50	315.39	10.63	88.6	11.40	0.77	0.06	
35X-1, 49-50	318.99	10.93	91.1	11.50	0.57	0.05	0.11
35X-3, 49-50	321.99	10.78	89.8	11.70	0.92	0.06	
35X-5, 49-50	324.99	10.49	87.3	11.40	0.92	0.06	
36X-1, 49-50	328.59	10.92	91.0	11.70	0.78		
36X-3, 49-50	331.59	10.94	91.2	11.70	0.76		
36X-5, 49-50	334.59	10.77	89.8	11.60	0.83	0.05	
37X-1, 49-50	338.19	10.48	87.3	11.30	0.82	0.05	
37X-3, 49-50	341.19	10.48	87.3	10.90	0.42		
37X-5, 49-50	344.19	10.36	86.3	10.90	0.54		0.00
38X-1, 49-50	347.79	10.47	87.3	11.40	0.93		
38X-3, 49-50	350.79	10.60	88.3	11.50	0.90		
38X-5, 49-50	353.79	10.46	87.1	11.10	0.64		
39X-1, 49-50	357.49	9.92	82.6	10.59	0.67	0.07	
39X-3, 49-50	360.49	10.53	87.7	10.91	0.38		
39X-5, 49-50	363.49	10.45	87.0	10.81	0.36		
40X-1, 49-50	367.09	10.39	86.5	10.55	0.16		
40X-3, 49-50	370.09	9.97	83.1	9.83			
40X-5, 49-50	373.09	10.42	86.8	10.78	0.36		
41X-1, 49-50	376.69	10.44	87.0	10.90	0.46		
41X-3, 49-50	379.69	10.44	87.0	10.52	0.08		
41X-5, 49-50	382.69	10.55	87.9	10.82	0.27		
42X-1, 49-50	386.09	10.57	88.0	10.74	0.17		
42X-3, 49-50	389.09	10.41	86.7	10.74	0.33	0.05	
42X-5, 49-50	392.09	10.50	87.5	10.55	0.05		
43X-1, 49-50	395.69	10.70	89.1	10.97	0.27	0.04	
43X-3, 49-50	398.69	10.45	87.0	10.71	0.26	0.05	
43X-5, 49-50	401.69	10.68	89.0	10.79	0.11		
44X-1, 49-50	405.29	10.38	86.5	10.56	0.18		
44X-3, 49-50	408.29	10.40	86.7	10.23			
44X-5, 49-50	411.29	10.48	87.3	10.88	0.40		
45X-1, 48-50	414.88	10.33	86.0	10.62	0.29		
45X-3, 48-50	417.88	10.48	87.3	10.61	0.13		
45X-5, 48-50	420.88	10.21	85.1	10.26	0.05		
46X-1, 49-50	424.49	10.54	87.8	10.53			
46X-3, 49-50	427.49	10.37	86.4	10.69	0.32		
47X-1, 49-50	434.19	10.18	84.8	10.35	0.17		
47X-3, 49-50	437.19	9.83	81.9	9.95	0.12		
47X-5, 49-50	440.19	10.54	87.8	10.79	0.25		

Table T5 (continued).

Core, section, interval (cm)	Depth (mbsf)	C_{inorg} (wt%)	$CaCO_3$ (wt%)	Total carbon (wt%)	C_{org} (wt%)	Nitrogen (wt%)	Sulfur (wt%)
48X-1, 49-50	443.79	10.34	86.1	10.34			
48X-3, 49-50	446.79	10.61	88.4	10.84	0.23		
48X-5, 49-50	449.79	10.44	87.0	10.50	0.06		
49X-1, 49-50	453.39	10.62	88.5	10.48			
49X-3, 49-50	456.39	10.79	89.9	10.88	0.09		
49X-4, 49-50	457.89	10.59	88.2	10.89	0.30		
50X-1, 49-50	462.99	10.70	89.1	10.93	0.23		
50X-5, 49-50	468.99	9.26	77.2	9.14			
51X-1, 49-50	472.59	10.21	85.0	10.20			
51X-3, 49-50	475.59	9.64	80.3	9.67	0.03		
51X-5, 49-50	478.59	9.58	79.8	9.62	0.04		
52X-1, 49-50	482.19	10.88	90.6	10.75			
52X-3, 49-50	485.19	10.70	89.2	10.24			
52X-5, 49-50	487.69	11.04	91.9	10.90			
53X-1, 48-50	491.88	10.66	88.8	10.57			

Note: Blank = not detected.

Table T6. Interstitial water geochemistry, Site 1127.

Core, section	Depth (mbsf)	Ca^{2+} (mM)	Mg^{2+} (mM)	K^{+} (mM)	Li^{+} (µM)	$H_4SiO_4^0$ (µM)	Sr^{2+} (µM)	NH_4^{+} (mM)	HPO_4^{2-} (µM)	SO_4^{2-} (mM)	Alkalinity (mM)	pH	ppH	Salinity	Cl^{-} (mM)
181-1127B-															
1H-1	1.45	11.3	54.6	11.0	36	191	73	0.3	0.0	30.4	3.17	7.80	7.83	34	528.88
1H-3	4.45	11.3	54.7	11.1	33	206	76	0.1	10.7	30.3	3.26	7.62	7.73	35	528.15
2H-2	8.85	8.0	52.7	11.0	36	672	138	3.5	33.9	22.8	31.66	8.04	7.05	36	545.60
2H-4	11.85	7.4	50.0	11.1	35	606	76	4.5	38.6	12.0	37.80	7.79	6.79	36	555.09
3H-2	18.35	6.8	48.1	11.6	38	726	76	6.6	69.1	5.1	46.01	6.97	6.72	37	578.16
3H-4	21.35	6.3	46.2	11.7	41	732	99	8.1	26.2	0.0	52.19	6.82	6.50	39	578.24
4H-3	28.28	6.3	45.9	12.7	44	766	122	9.9	74.0	0.0	59.75	7.01	6.58	40	615.02
4H-5	31.28	6.2	44.7	12.6	46	843	130	11.0	221.9	3.0	61.09	6.84	6.58	40	622.27
5H-2	37.35	5.9	46.4	14.4	52	837	126	13.5	54.5	0.0	66.63	6.81	6.58	42	666.94
5H-4	40.35	5.9	44.8	13.6	50	711	134	13.0	59.6	0.0	66.58	6.81	6.55	42	702.44
6H-4	49.85	4.8	39.5	14.5	54	805	115	15.1	67.7	5.2	74.02	6.92	6.62	45	713.95
7H-3	57.80	4.4	36.2	14.8	62	901	130	17.1		0.0	82.16	6.68	6.56	48	728.31
8H-3	67.30	4.7	34.4	15.9	64	813	122	18.5	89.4	3.3	85.78	6.71	6.58	50.5	786.04
9H-3	76.80	4.1	31.8	16.6	80	841	187	18.2	70.5	3.0	97.82	6.94	6.54	54	836.86
10H-4	86.69	3.8	30.6	17.2	88	908	222	16.8	97.7	0.0	101.84	6.67	6.52	57.5	879.00
11H-3	95.80	4.5	29.4	18.1	87	940	176	16.8	113.3	0.0	102.88	6.61	6.50	59	909.42
12H-3	104.54	4.0	29.0	18.5	84	965	176	17.2	134.0	0.0	105.70	6.68	6.51	62	910.38
13H-3	114.73	3.5	26.4	19.5	108	970	180	17.4	99.6	0.0	98.28	6.74		64	959.82
14H-4	124.95	3.5	28.0	20.1	143	961	187	18.9	107.8	0.0	105.90	6.80	6.52	67	1011.43
15H-3	133.06	3.7	29.8	20.1	119		229	18.5	45.6	0.0	105.10	6.58	6.52	69	1064.66
16H-2	141.80									0.0	100.10	6.66	6.43	70	1072.22
17X-2	151.30	4.1	33.8	22.0	94	811	199	18.2	83.4	0.0	96.52	6.65	6.54	72	1181.95
18X-2	157.80	4.7	36.9	21.5	126	848	302	22.5	64.5	0.0	101.80	6.35	6.52	73.5	1182.48
19X-3	168.90	4.1	35.8	24.8	100	955	375	24.7	57.8	0.0	91.31	6.54	6.35	76	1248.08
20X-2	177.00	4.3	34.7	23.9	250	935	463	23.5	25.5	7.8	85.48	6.48	6.36	77	1296.73
21X-4	189.31	5.1	39.4	23.7	222	873	443	20.0	38.9	6.1	84.34	6.51	6.29	79	1310.85
23X-2	205.90	6.4	47.9	25.2	230		539	19.9	25.2	14.0	82.27	6.48	6.32	83	1438.36
26X-3	236.30	9.8	61.0	26.6	183	824	684	19.7	58.4	22.7	70.03	6.39	6.28	88	1495.87
28X-3	255.50	11.7	64.2	22.9	163	713	700	18.5	18.7	26.5	54.91	7.10	6.17	77	1264.79
30X-3	274.80	13.7	72.5	25.8	172	899	661	20.0	173.3	30.4	57.80	6.33	6.13	85	1433.69
33X-3	303.70	14.8	77.2	25.5	641	779	539	17.5	14.8	33.9		6.18	6.10	82	1424.38
36X-3	332.50	18.2	88.9	31.9	623	822	581	16.9	29.8	38.3	50.34	6.18		95	1585.33
39X-3	361.40	21.2	92.6	32.0	523	871	623	16.5	26.2	37.3	44.32	6.12		96	1622.15
43X-3	399.60	23.2	94.1	30.2	396	824	608	13.0	24.7	34.6	32.27	6.11		96	1658.28
46X-2	426.90	31.0	102.0	33.4	323	942	585	9.5	13.9	38.2		6.00	6.01	98	1740.73
49X-2	455.80	34.7	107.4	32.1	246	1040	554	9.0	24.7	42.9	23.45	6.05		96	1702.77
52X-2	484.60	41.2	105.0	26.8	590	1043	478	7.1	116.7	47.1	21.84	6.07	5.92	99	1681.36

Note: Blank = not detected.

Table T7. Summary of X-ray diffraction analysis, Site 1127. (**See table notes.** Continued on next two pages.)

Leg	Site	Hole	Core	Type	Section	Top (cm)	Bottom (cm)	Depth (mbsf)	Aragonite (wt%)	Quartz (wt%)	LMC (wt%)	HMC (wt%)	Dolomite (wt%)
182	1127	B	1	H	3	48	50	3.48	15	1	34	50	0
182	1127	B	1	H	3	48	50	3.48	15	1	31	52	1
182	1127	B	2	H	1	49	50	6.39	10	1	33	56	0
182	1127	B	2	H	3	49	50	9.39	14	0	22	63	1
182	1127	B	2	H	5	49	50	12.39	15	0	22	61	1
182	1127	B	3	H	1	49	50	15.89	14	0	28	58	0
182	1127	B	3	H	3	49	50	18.89	19	0	33	47	2
182	1127	B	3	H	5	49	50	21.89	18	0	37	45	0
182	1127	B	4	H	1	49	50	25.39	13	0	41	42	3
182	1127	B	4	H	3	49	50	27.32	15	0	29	55	1
182	1127	B	4	H	5	49	50	30.32	15	1	30	53	1
182	1127	B	5	H	3	49	50	37.89	20	1	30	49	0
182	1127	B	5	H	5	49	50	40.89	17	0	29	54	0
182	1127	B	6	H	1	49	50	44.39	21	0	28	51	0
182	1127	B	6	H	3	49	50	47.39	21	1	33	45	0
182	1127	B	6	H	5	49	50	50.39	19	0	23	57	1
182	1127	B	7	H	1	49	50	53.89	22	2	31	45	1
182	1127	B	7	H	3	49	50	56.89	17	1	38	44	0
182	1127	B	7	H	5	49	50	59.89	18	5	40	36	2
182	1127	B	8	H	1	49	50	63.39	12	3	24	60	1
182	1127	B	8	H	3	49	50	66.39	15	1	23	59	2
182	1127	B	8	H	5	49	50	69.39	22	0	21	55	1
182	1127	B	9	H	1	49	50	72.89	13	0	28	59	0
182	1127	B	9	H	3	49	50	75.89	16	1	31	52	1
182	1127	B	9	H	5	49	50	78.82	16	1	36	46	2
182	1127	B	10	H	3	49	50	84.28	15	0	38	44	3
182	1127	B	10	H	5	49	50	87.28	19	1	47	30	4
182	1127	B	11	H	1	49	50	91.89	15	0	41	42	2
182	1127	B	11	H	3	49	50	94.89	14	1	31	53	2
182	1127	B	11	H	5	49	50	97.87	11	0	25	63	1
182	1127	B	12	H	1	49	50	101.39	16	1	28	54	1
182	1127	B	12	H	3	49	50	103.63	16	2	24	52	5
182	1127	B	12	H	5	49	50	106.63	16	1	29	54	1
182	1127	B	13	H	1	49	50	110.89	14	1	45	29	11
182	1127	B	13	H	3	49	50	113.89	14	2	35	48	1
182	1127	B	13	H	5	49	50	116.61	12	1	29	57	1
182	1127	B	14	H	1	49	50	120.39	16	2	46	31	4
182	1127	B	14	H	3	49	50	122.54	17	1	26	54	3
182	1127	B	14	H	5	49	50	125.54	18	0	26	50	5
182	1127	B	15	H	1	49	50	129.89	21	1	30	45	3
182	1127	B	15	H	3	49	50	132.15	22	1	43	31	3
182	1127	B	15	H	5	49	50	135.15	12	0	36	50	2
182	1127	B	16	H	1	49	50	139.39	20	1	49	28	2
182	1127	B	16	H	3	49	50	142.39	18	0	28	51	2
182	1127	B	17	X	1	49	50	148.89	19	1	34	46	1
182	1127	B	17	X	3	48	49	151.88	17	1	27	53	2
182	1127	B	17	X	5	49	50	154.72	15	0	29	55	2
182	1127	B	18	X	1	49	50	155.39	15	11	21	53	1
182	1127	B	18	X	3	49	50	158.39	20	0	40	38	2
182	1127	B	18	X	5	49	50	161.39	15	0	25	53	7
182	1127	B	19	X	1	49	50	164.99	19	1	47	32	1
182	1127	B	19	X	3	49	50	167.99	16	1	49	33	1
182	1127	B	19	X	5	49	50	170.99	16	1	59	23	1
182	1127	B	20	X	1	49	50	174.59	15	0	79	0	6
182	1127	B	20	X	3	49	50	177.59	9	1	83	0	7
182	1127	B	21	X	1	50	51	184.2	12	1	52	0	35
182	1127	B	21	X	3	49	50	186.9	15	0	32	52	1
182	1127	B	21	X	5	48	49	189.89	18	0	27	53	2
182	1127	B	22	X	1	49	50	193.89	19	0	31	49	1
182	1127	B	22	X	3	49	50	196.89	21	0	36	40	2
182	1127	B	23	X	1	49	50	203.49	13	0	18	68	1
182	1127	B	23	X	3	49	50	206.49	22	1	39	37	1
182	1127	B	23	X	5	49	50	209.49	24	1	59	14	2
182	1127	B	24	X	1	49	50	213.09	20	2	73	0	4
182	1127	B	24	X	3	49	50	216.09	10	0	88	0	2
182	1127	B	25	X	1	49	50	222.79	13	1	54	29	3
182	1127	B	25	X	3	49	50	225.79	14	2	32	51	1
182	1127	B	25	X	5	49	50	228.79	19	2	49	27	3

Table T7 (continued).

Leg	Site	Hole	Core	Type	Section	Top (cm)	Bottom (cm)	Depth (mbsf)	Aragonite (wt%)	Quartz (wt%)	LMC (wt%)	HMC (wt%)	Dolomite (wt%)
182	1127	B	26	X	1	49	50	232.39	16	0	31	52	1
182	1127	B	26	X	3	49	50	235.39	15	0	21	64	1
182	1127	B	26	X	5	49	50	238.39	19	1	29	50	1
182	1127	B	27	X	1	49	50	241.99	17	0	32	50	1
182	1127	B	27	X	3	49	50	244.99	22	1	72	0	5
182	1127	B	27	X	5	49	50	247.99	9	1	64	0	26
182	1127	B	28	X	1	49	50	251.59	20	1	75	0	4
182	1127	B	28	X	3	49	50	254.59	19	1	64	0	17
182	1127	B	28	X	5	49	50	257.59	20	0	30	48	2
182	1127	B	29	X	1	49	50	261.29	19	1	26	51	3
182	1127	B	29	X	3	49	50	264.29	16	0	38	44	2
182	1127	B	29	X	5	49	50	267.29	16	1	41	40	2
182	1127	B	29	X	7	50	51	269.65	20	1	52	24	3
182	1127	B	30	X	1	49	50	270.89	19	1	35	41	4
182	1127	B	30	X	3	49	50	273.89	21	0	32	44	3
182	1127	B	30	X	5	49	50	276.89	19	0	30	47	4
182	1127	B	31	X	1	49	50	280.49	18	0	29	51	2
182	1127	B	31	X	3	48	49	283.48	19	1	39	40	1
182	1127	B	31	X	5	49	50	286.49	17	1	26	55	1
182	1127	B	32	X	1	49	50	290.19	18	0	79	0	4
182	1127	B	32	X	3	50	51	293.2	15	0	76	0	9
182	1127	B	33	X	1	49	50	299.79	20	0	31	46	2
182	1127	B	33	X	3	49	50	302.79	22	1	50	24	2
182	1127	B	33	X	5	49	50	305.79	12	1	65	0	23
182	1127	B	34	X	1	49	50	309.39	15	1	23	58	2
182	1127	B	34	X	3	49	50	312.39	12	2	55	28	2
182	1127	B	34	X	5	49	50	315.39	12	1	32	54	1
182	1127	B	35	X	1	49	50	318.99	18	2	26	51	4
182	1127	B	35	X	3	49	50	321.99	23	0	38	34	5
182	1127	B	35	X	5	49	50	324.99	18	1	57	20	4
182	1127	B	36	X	1	49	50	328.59	19	0	31	38	11
182	1127	B	36	X	3	49	50	331.59	16	2	41	32	9
182	1127	B	36	X	5	49	50	334.59	16	1	44	35	4
182	1127	B	37	X	1	49	50	338.19	18	1	60	14	7
182	1127	B	37	X	3	49	50	341.19	10	1	75	0	13
182	1127	B	37	X	5	49	50	344.19	9	1	86	0	4
182	1127	B	38	X	1	49	50	347.79	16	2	48	32	2
182	1127	B	38	X	3	49	50	350.79	16	1	76	0	6
182	1127	B	38	X	5	49	50	353.79	14	1	78	0	7
182	1127	B	39	X	1	49	50	357.49	23	2	26	47	2
182	1127	B	39	X	3	49	50	360.49	16	1	52	27	5
182	1127	B	39	X	5	49	50	363.49	16	1	45	37	2
182	1127	B	40	X	1	49	50	367.09	16	1	79	0	4
182	1127	B	40	X	3	49	50	370.09	5	1	92	0	2
182	1127	B	40	X	5	49	50	373.09	16	1	60	19	3
182	1127	B	41	X	1	49	50	376.69	13	1	81	0	5
182	1127	B	41	X	3	49	50	379.69	9	1	86	0	4
182	1127	B	41	X	5	49	50	382.69	15	4	77	0	5
182	1127	B	42	X	1	49	50	386.09	8	1	88	0	3
182	1127	B	42	X	3	49	50	389.09	19	1	75	0	5
182	1127	B	42	X	5	49	50	392.09	14	1	69	12	4
182	1127	B	43	X	1	49	50	395.69	13	1	81	0	5
182	1127	B	43	X	3	49	50	398.69	14	1	82	0	4
182	1127	B	43	X	5	49	50	401.69	16	1	59	22	2
182	1127	B	44	X	1	49	50	405.29	10	1	87	0	3
182	1127	B	44	X	3	49	50	408.29	3	1	94	0	2
182	1127	B	44	X	5	49	50	411.29	17	1	78	0	4
182	1127	B	45	X	1	48	50	414.88	16	2	81	0	2
182	1127	B	45	X	3	48	50	417.88	14	3	80	0	3
182	1127	B	45	X	5	48	50	420.88	6	2	92	0	0
182	1127	B	46	X	1	49	50	424.49	6	2	91	0	1
182	1127	B	46	X	3	49	50	427.49	10	1	88	0	1
182	1127	B	47	X	1	49	50	434.19	14	1	84	0	1
182	1127	B	47	X	3	49	50	437.19	7	1	90	0	1
182	1127	B	47	X	5	49	50	440.19	10	1	87	0	2
182	1127	B	48	X	1	49	50	443.79	0	1	99	0	0
182	1127	B	48	X	3	49	50	446.79	9	2	88	0	2
182	1127	B	48	X	5	49	50	449.79	4	1	94	0	1
182	1127	B	49	X	1	49	50	453.39	0	2	98	0	0

Table T7 (continued).

Leg	Site	Hole	Core	Type	Section	Top (cm)	Bottom (cm)	Depth (mbsf)	Aragonite (wt%)	Quartz (wt%)	LMC (wt%)	HMC (wt%)	Dolomite (wt%)
182	1127	B	49	X	3	49	50	456.39	4	1	68	26	1
182	1127	B	49	X	4	49	50	457.89	6	1	43	46	5
182	1127	B	50	X	1	49	50	462.99	2	1	70	26	1
182	1127	B	50	X	5	49	50	468.99	0	4	95	0	1
182	1127	B	51	X	1	49	50	472.59	0	0	91	0	9
182	1127	B	51	X	3	49	50	475.59	0	3	97	0	0
182	1127	B	51	X	5	49	50	478.59	0	2	98	0	0
182	1127	B	52	X	1	49	50	482.19	0	2	93	0	6
182	1127	B	52	X	3	49	50	485.19	0	2	98	0	1
182	1127	B	52	X	5	49	50	487.69	0	0	97	0	2
182	1127	B	53	X	1	48	50	491.88	0	1	99	0	0

Notes: LMC = low-Mg calcite, HMC = high-Mg calcite. This table is also available in **ASCII format.**

Table T8. *P*-wave velocity measurements from the multisensor track, Site 1127.

Leg	Site	Hole	Core	Type	Section	Interval (cm)	Depth (mbsf)	V_p (km/s)
182	1127	B	2	H	2	3.00	7.43	1.8852
182	1127	B	2	H	2	23.00	7.63	1.8813
182	1127	B	2	H	2	43.00	7.83	1.8804
182	1127	B	2	H	2	59.00	7.99	1.8813
182	1127	B	2	H	2	75.00	8.15	1.8817
182	1127	B	2	H	2	79.00	8.19	2.3979
182	1127	B	2	H	2	83.00	8.23	2.3986
182	1127	B	2	H	3	11.00	9.01	2.3965
182	1127	B	2	H	3	27.00	9.17	1.5490
182	1127	B	2	H	3	35.00	9.25	1.8826
182	1127	B	2	H	3	43.00	9.33	2.3993
182	1127	B	2	H	3	55.00	9.45	2.3950
182	1127	B	2	H	3	59.00	9.49	1.5484
182	1127	B	2	H	3	67.00	9.57	1.8791
182	1127	B	2	H	3	75.00	9.65	2.3958
182	1127	B	2	H	3	79.00	9.69	2.3986
182	1127	B	2	H	3	103.00	9.93	2.7848
182	1127	B	2	H	4	3.00	10.43	2.4022
182	1127	B	2	H	4	7.00	10.47	1.8808
182	1127	B	2	H	4	11.00	10.51	3.3152
182	1127	B	2	H	4	15.00	10.55	2.3986
182	1127	B	2	H	4	19.00	10.59	2.4036
182	1127	B	2	H	4	27.00	10.67	3.3097
182	1127	B	2	H	4	31.00	10.71	3.3002
182	1127	B	2	H	4	39.00	10.79	2.4029
182	1127	B	2	H	4	43.00	10.83	2.3993
182	1127	B	2	H	4	47.00	10.87	3.3070
182	1127	B	2	H	4	51.00	10.91	3.3016
182	1127	B	2	H	4	67.00	11.07	3.2975
182	1127	B	2	H	4	71.00	11.11	3.3030
182	1127	B	2	H	4	75.00	11.15	1.8808
182	1127	B	2	H	4	79.00	11.19	2.3958
182	1127	B	2	H	4	83.00	11.23	1.8817
182	1127	B	2	H	4	87.00	11.27	3.3030
182	1127	B	2	H	4	103.00	11.43	3.3125
182	1127	B	2	H	4	119.00	11.59	3.2300
182	1127	B	2	H	4	135.00	11.75	3.4697
182	1127	B	2	H	4	139.00	11.79	3.2975
182	1127	B	2	H	5	3.00	11.93	2.4036
182	1127	B	2	H	5	7.00	11.97	2.3993
182	1127	B	2	H	5	11.00	12.01	3.3179
182	1127	B	2	H	5	15.00	12.05	3.3097
182	1127	B	2	H	5	19.00	12.09	3.3193
182	1127	B	2	H	5	23.00	12.13	3.3043
182	1127	B	2	H	5	27.00	12.17	3.3152
182	1127	B	2	H	5	31.00	12.21	3.3125
182	1127	B	2	H	5	35.00	12.25	2.3979
182	1127	B	2	H	5	39.00	12.29	3.3125
182	1127	B	2	H	5	43.00	12.33	2.4008
182	1127	B	2	H	5	47.00	12.37	3.3016
182	1127	B	2	H	5	51.00	12.41	3.3002
182	1127	B	2	H	5	75.00	12.65	3.3016
182	1127	B	2	H	5	83.00	12.73	3.3016
182	1127	B	2	H	5	95.00	12.85	2.1504
182	1127	B	2	H	5	111.00	13.01	2.9182
182	1127	B	2	H	6	3.00	13.43	3.3070
182	1127	B	2	H	6	19.00	13.59	2.3972
182	1127	B	2	H	6	27.00	13.67	3.3084
182	1127	B	2	H	6	31.00	13.71	2.3965
182	1127	B	2	H	6	35.00	13.75	2.3965
182	1127	B	2	H	6	47.00	13.87	3.3016
182	1127	B	2	H	6	51.00	13.91	1.8813
182	1127	B	2	H	6	55.00	13.95	3.3097
182	1127	B	2	H	6	67.00	14.07	3.3057

Note: Only a portion of this table appears here. The complete table is available in **ASCII format.**

Table T9. Gamma-ray attenuation densiometry measurements from the multisensor track, Site 1127.

Leg	Site	Hole	Core	Type	Section	Interval (cm)	Depth (mbsf)	Density (g/cm^3)	Corrected Density (g/cm^3)
182	1127	B	2	H	2	3.0	7.43	1.72	1.66
182	1127	B	2	H	2	7.0	7.47	1.75	1.69
182	1127	B	2	H	2	11.0	7.51	1.72	1.66
182	1127	B	2	H	2	15.0	7.55	1.76	1.70
182	1127	B	2	H	2	19.0	7.59	1.71	1.65
182	1127	B	2	H	2	23.0	7.63	1.74	1.68
182	1127	B	2	H	2	27.0	7.67	1.74	1.68
182	1127	B	2	H	2	31.0	7.71	1.74	1.68
182	1127	B	2	H	2	35.0	7.75	1.74	1.68
182	1127	B	2	H	2	39.0	7.79	1.74	1.68
182	1127	B	2	H	2	43.0	7.83	1.71	1.64
182	1127	B	2	H	2	47.0	7.87	1.72	1.66
182	1127	B	2	H	2	51.0	7.91	1.69	1.62
182	1127	B	2	H	2	55.0	7.95	1.67	1.60
182	1127	B	2	H	2	59.0	7.99	1.72	1.65
182	1127	B	2	H	2	63.0	8.03	1.71	1.64
182	1127	B	2	H	2	67.0	8.07	1.69	1.63
182	1127	B	2	H	2	71.0	8.11	1.73	1.66
182	1127	B	2	H	2	75.0	8.15	1.70	1.64
182	1127	B	2	H	2	79.0	8.19	1.74	1.68
182	1127	B	2	H	2	83.0	8.23	1.74	1.68
182	1127	B	2	H	2	87.0	8.27	1.77	1.71
182	1127	B	2	H	2	91.0	8.31	1.75	1.68
182	1127	B	2	H	2	95.0	8.35	1.77	1.70
182	1127	B	2	H	2	99.0	8.39	1.74	1.67
182	1127	B	2	H	2	103.0	8.43	1.78	1.72
182	1127	B	2	H	2	107.0	8.47	1.77	1.70
182	1127	B	2	H	2	111.0	8.51	1.73	1.66
182	1127	B	2	H	2	115.0	8.55	1.74	1.68
182	1127	B	2	H	2	119.0	8.59	1.74	1.68
182	1127	B	2	H	2	123.0	8.63	1.76	1.69
182	1127	B	2	H	2	127.0	8.67	1.77	1.71
182	1127	B	2	H	2	131.0	8.71	1.76	1.70
182	1127	B	2	H	2	135.0	8.75	1.80	1.74
182	1127	B	2	H	2	139.0	8.79	1.78	1.72
182	1127	B	2	H	3	3.0	8.93	1.81	1.75
182	1127	B	2	H	3	7.0	8.97	1.86	1.80
182	1127	B	2	H	3	11.0	9.01	1.82	1.76
182	1127	B	2	H	3	15.0	9.05	1.84	1.79
182	1127	B	2	H	3	19.0	9.09	1.83	1.77
182	1127	B	2	H	3	23.0	9.13	1.81	1.75
182	1127	B	2	H	3	27.0	9.17	1.83	1.77
182	1127	B	2	H	3	31.0	9.21	1.84	1.78
182	1127	B	2	H	3	35.0	9.25	1.83	1.77
182	1127	B	2	H	3	39.0	9.29	1.82	1.76
182	1127	B	2	H	3	43.0	9.33	1.85	1.79
182	1127	B	2	H	3	47.0	9.37	1.83	1.78
182	1127	B	2	H	3	51.0	9.41	1.84	1.78
182	1127	B	2	H	3	55.0	9.45	1.85	1.79
182	1127	B	2	H	3	59.0	9.49	1.82	1.76
182	1127	B	2	H	3	63.0	9.53	1.83	1.78
182	1127	B	2	H	3	67.0	9.57	1.81	1.75
182	1127	B	2	H	3	71.0	9.61	1.80	1.74
182	1127	B	2	H	3	75.0	9.65	1.78	1.72
182	1127	B	2	H	3	79.0	9.69	1.80	1.75
182	1127	B	2	H	3	83.0	9.73	1.82	1.76
182	1127	B	2	H	3	87.0	9.77	1.82	1.76
182	1127	B	2	H	3	91.0	9.81	1.82	1.77
182	1127	B	2	H	3	95.0	9.85	1.85	1.80
182	1127	B	2	H	3	99.0	9.89	1.82	1.77
182	1127	B	2	H	3	103.0	9.93	1.85	1.79
182	1127	B	2	H	3	107.0	9.97	1.81	1.76
182	1127	B	2	H	3	111.0	10.01	1.85	1.79

Note: Only a portion of this table appears here. The complete table is available in **ASCII format.**

Table T10. Magnetic susceptibility measurements from the multisensor track, Site 1127.

Leg	Site	Hole	Core	Type	Section	Interval (cm)	Depth (mbsf)	Magnetic susceptibility (10^{-6} SI units)	Corrected susceptibility (10^{-6} SI units)
182	1127	A	1	H	1	3.0	0.03	0.1	0.1
182	1127	A	1	H	1	11.0	0.11	1.0	1.0
182	1127	A	1	H	1	19.0	0.19	–1.0	–1.0
182	1127	A	1	H	1	27.0	0.27	–1.1	–1.1
182	1127	A	1	H	1	35.0	0.35	–1.6	–1.6
182	1127	A	1	H	1	43.0	0.43	–1.9	–1.9
182	1127	A	1	H	1	51.0	0.51	–1.9	–1.9
182	1127	A	1	H	1	59.0	0.59	–2.0	–2.0
182	1127	A	1	H	1	67.0	0.67	–2.4	–2.4
182	1127	A	1	H	1	75.0	0.75	–2.0	–2.0
182	1127	A	1	H	1	83.0	0.83	–2.3	–2.3
182	1127	A	1	H	1	91.0	0.91	–2.2	–2.2
182	1127	A	1	H	1	99.0	0.99	–2.6	–2.6
182	1127	A	1	H	1	107.0	1.07	–2.5	–2.5
182	1127	A	1	H	1	115.0	1.15	–2.6	–2.6
182	1127	A	1	H	1	123.0	1.23	–2.8	–2.8
182	1127	A	1	H	1	131.0	1.31	–2.9	–2.9
182	1127	A	1	H	1	139.0	1.39	–2.6	–2.6
182	1127	A	1	H	2	3.0	1.53	–2.5	–2.5
182	1127	A	1	H	2	11.0	1.61	–2.8	–2.8
182	1127	A	1	H	2	19.0	1.69	–2.4	–2.4
182	1127	A	1	H	2	27.0	1.77	–2.7	–2.7
182	1127	A	1	H	2	35.0	1.85	–2.9	–2.9
182	1127	A	1	H	2	43.0	1.93	–3.0	–3.0
182	1127	A	1	H	2	51.0	2.01	–3.4	–3.4
182	1127	A	1	H	2	59.0	2.09	–2.9	–2.9
182	1127	A	1	H	2	67.0	2.17	–2.8	–2.8
182	1127	A	1	H	2	75.0	2.25	–3.3	–3.3
182	1127	A	1	H	2	83.0	2.33	–2.9	–2.9
182	1127	A	1	H	2	91.0	2.41	–3.0	–3.0
182	1127	A	1	H	2	99.0	2.49	–3.0	–3.0
182	1127	A	1	H	2	107.0	2.57	–3.1	–3.1
182	1127	A	1	H	2	115.0	2.65	–3.3	–3.3
182	1127	A	1	H	2	123.0	2.73	–3.6	–3.6
182	1127	A	1	H	2	131.0	2.81	–3.3	–3.3
182	1127	A	1	H	2	139.0	2.89	–3.1	–3.1
182	1127	A	1	H	2	147.0	2.97	–3.2	–3.2
182	1127	A	1	H	3	3.0	3.03	–2.3	–2.3
182	1127	A	1	H	3	11.0	3.11	–2.5	–2.5
182	1127	A	1	H	3	19.0	3.19	–2.3	–2.3
182	1127	A	1	H	3	27.0	3.27	–2.5	–2.5
182	1127	A	1	H	3	35.0	3.35	–2.6	–2.6
182	1127	A	1	H	3	43.0	3.43	–3.2	–3.2
182	1127	A	1	H	3	51.0	3.51	–2.8	–2.8
182	1127	A	1	H	3	59.0	3.59	–2.8	–2.8
182	1127	A	1	H	3	67.0	3.67	–2.7	–2.7
182	1127	A	1	H	3	75.0	3.75	–2.3	–2.3
182	1127	A	1	H	3	83.0	3.83	–2.3	–2.3
182	1127	A	1	H	3	91.0	3.91	–2.5	–2.5
182	1127	A	1	H	3	99.0	3.99	–2.6	–2.6
182	1127	A	1	H	3	107.0	4.07	–2.9	–2.9
182	1127	A	1	H	3	115.0	4.15	–3.0	–3.0
182	1127	A	1	H	3	123.0	4.23	–3.2	–3.2
182	1127	A	1	H	3	131.0	4.31	–3.2	–3.2
182	1127	A	1	H	3	139.0	4.39	–2.5	–2.5
182	1127	A	1	H	4	3.0	4.53	–1.1	–1.1
182	1127	A	1	H	4	11.0	4.61	–1.0	–1.0
182	1127	A	1	H	4	19.0	4.69	–1.2	–1.2
182	1127	A	1	H	4	27.0	4.77	–1.2	–1.2
182	1127	A	1	H	4	35.0	4.85	–1.0	–1.0
182	1127	A	1	H	4	43.0	4.93	–1.4	–1.4
182	1127	A	1	H	4	51.0	5.01	–1.8	–1.8
182	1127	A	1	H	4	59.0	5.09	–1.9	–1.9

Note: Only a portion of this table appears here. The complete table is available in **ASCII format.**

Table T11. Natural gamma-ray measurements from the multisensor track, Site 1127.

Leg	Site	Hole	Core	Type	Section	Interval (cm)	Depth (mbsf)	NGR (cps)
182	1127	A	1	H	1	3.0	0.03	2.08
182	1127	A	1	H	1	19.0	0.19	1.46
182	1127	A	1	H	1	35.0	0.35	1.08
182	1127	A	1	H	1	51.0	0.51	1.23
182	1127	A	1	H	1	67.0	0.67	0.96
182	1127	A	1	H	1	83.0	0.83	2.42
182	1127	A	1	H	1	99.0	0.99	2.04
182	1127	A	1	H	1	115.0	1.15	1.89
182	1127	A	1	H	1	131.0	1.31	2.42
182	1127	A	1	H	2	3.0	1.53	4.15
182	1127	A	1	H	2	19.0	1.69	2.89
182	1127	A	1	H	2	35.0	1.85	2.92
182	1127	A	1	H	2	51.0	2.01	2.81
182	1127	A	1	H	2	67.0	2.17	2.69
182	1127	A	1	H	2	83.0	2.33	5.15
182	1127	A	1	H	2	99.0	2.49	6.12
182	1127	A	1	H	2	115.0	2.65	5.46
182	1127	A	1	H	2	131.0	2.81	4.96
182	1127	A	1	H	2	147.0	2.97	4.35
182	1127	A	1	H	3	3.0	3.03	3.73
182	1127	A	1	H	3	19.0	3.19	4.35
182	1127	A	1	H	3	35.0	3.35	5.08
182	1127	A	1	H	3	51.0	3.51	5.31
182	1127	A	1	H	3	67.0	3.67	5.96
182	1127	A	1	H	3	83.0	3.83	3.92
182	1127	A	1	H	3	99.0	3.99	5.23
182	1127	A	1	H	3	115.0	4.15	4.62
182	1127	A	1	H	3	131.0	4.31	6.04
182	1127	A	1	H	4	3.0	4.53	4.85
182	1127	A	1	H	4	19.0	4.69	3.92
182	1127	A	1	H	4	35.0	4.85	5.96
182	1127	A	1	H	4	51.0	5.01	6.27
182	1127	A	1	H	4	67.0	5.17	5.27
182	1127	A	1	H	4	83.0	5.33	5.46
182	1127	A	1	H	4	99.0	5.49	4.85
182	1127	A	1	H	4	115.0	5.65	5.81
182	1127	A	1	H	4	131.0	5.81	5.23
182	1127	A	1	H	4	147.0	5.97	3.50
182	1127	A	1	H	5	3.0	6.03	5.50
182	1127	A	1	H	5	19.0	6.19	7.19
182	1127	A	1	H	5	35.0	6.35	5.85
182	1127	A	1	H	5	51.0	6.51	7.46
182	1127	A	1	H	5	67.0	6.67	7.19
182	1127	A	1	H	5	83.0	6.83	6.15
182	1127	A	1	H	5	99.0	6.99	7.15
182	1127	A	1	H	5	115.0	7.15	6.42
182	1127	A	1	H	5	131.0	7.31	6.89
182	1127	A	1	H	5	147.0	7.47	3.46
182	1127	A	1	H	6	3.0	7.53	3.96
182	1127	A	1	H	6	19.0	7.69	8.19
182	1127	A	1	H	6	35.0	7.85	6.65
182	1127	A	1	H	6	51.0	8.01	6.77
182	1127	A	1	H	6	67.0	8.17	5.58
182	1127	A	1	H	6	83.0	8.33	6.89
182	1127	A	1	H	6	99.0	8.49	6.35
182	1127	A	1	H	6	115.0	8.65	5.58
182	1127	A	1	H	6	131.0	8.81	5.00
182	1127	B	1	H	1	3.0	0.03	1.08
182	1127	B	1	H	1	19.0	0.19	1.46
182	1127	B	1	H	1	35.0	0.35	1.31
182	1127	B	1	H	1	51.0	0.51	0.96
182	1127	B	1	H	1	67.0	0.67	1.73
182	1127	B	1	H	1	83.0	0.83	2.15
182	1127	B	1	H	1	99.0	0.99	2.46

Notes: NGR = natural gamma radiation. Only a portion of this table appears here. The complete table is available in **ASCII format.**

Table T12. Thermal conductivity measurements, Site 1127.

Leg	Site	Hole	Core	Type	Section	Interval (cm)	Depth (mbsf)	Thermal conductivity (W/[m·K])
182	1127	B	3	H	3	80.0	19.20	0.957
182	1127	B	3	H	3	80.0	19.20	0.927
182	1127	B	3	H	3	80.0	19.20	0.948
182	1127	B	4	H	3	72.0	27.55	0.848
182	1127	B	4	H	3	72.0	27.55	0.807
182	1127	B	4	H	3	72.0	27.55	0.841
182	1127	B	5	H	3	61.0	38.01	0.820
182	1127	B	5	H	3	61.0	38.01	0.801
182	1127	B	5	H	3	61.0	38.01	0.805
182	1127	B	6	H	3	82.0	47.72	0.877
182	1127	B	6	H	3	82.0	47.72	0.850
182	1127	B	6	H	3	82.0	47.72	0.846
182	1127	B	7	H	3	68.0	57.08	0.865
182	1127	B	7	H	3	68.0	57.08	0.857
182	1127	B	7	H	3	68.0	57.08	0.856
182	1127	B	8	H	3	68.0	66.58	0.542
182	1127	B	8	H	3	68.0	66.58	0.613
182	1127	B	8	H	3	68.0	66.58	0.596
182	1127	B	9	H	3	68.0	76.08	0.635
182	1127	B	9	H	3	68.0	76.08	0.589
182	1127	B	9	H	3	68.0	76.08	0.676
182	1127	B	10	H	3	75.0	84.54	0.449
182	1127	B	10	H	3	75.0	84.54	0.457
182	1127	B	10	H	3	75.0	84.54	0.457
182	1127	B	11	H	3	75.0	95.15	0.605
182	1127	B	11	H	3	75.0	95.15	0.606
182	1127	B	11	H	3	75.0	95.15	0.615
182	1127	B	12	H	3	75.0	103.89	0.586
182	1127	B	12	H	3	75.0	103.89	0.610
182	1127	B	12	H	3	75.0	103.89	0.408
182	1127	B	13	H	3	75.0	114.15	0.745
182	1127	B	13	H	3	75.0	114.15	0.735
182	1127	B	13	H	3	75.0	114.15	0.718
182	1127	B	14	H	3	62.0	122.67	0.792
182	1127	B	14	H	3	62.0	122.67	0.783
182	1127	B	14	H	3	62.0	122.67	0.790
182	1127	B	15	H	3	75.0	132.41	0.907
182	1127	B	15	H	3	75.0	132.41	0.863
182	1127	B	15	H	3	75.0	132.41	0.859
182	1127	B	16	H	3	54.0	142.44	0.852
182	1127	B	16	H	3	54.0	142.44	0.832
182	1127	B	16	H	3	54.0	142.44	0.873
182	1127	B	17	X	3	43.0	148.86	0.965
182	1127	B	17	X	3	43.0	148.86	0.930
182	1127	B	17	X	3	43.0	148.86	0.925
182	1127	B	18	X	3	59.0	158.49	0.857
182	1127	B	18	X	3	59.0	158.49	0.873
182	1127	B	18	X	3	59.0	158.49	0.857
182	1127	B	19	X	3	88.0	168.38	0.894
182	1127	B	19	X	3	88.0	168.38	0.887
182	1127	B	19	X	3	88.0	168.38	0.899
182	1127	B	20	X	3	66.0	177.76	0.995
182	1127	B	20	X	3	66.0	177.76	0.969
182	1127	B	20	X	3	66.0	177.76	0.982
182	1127	B	21	X	3	92.0	187.33	0.902
182	1127	B	21	X	3	92.0	187.33	0.878
182	1127	B	21	X	3	92.0	187.33	0.886
182	1127	B	22	X	3	84.0	197.24	0.972
182	1127	B	22	X	3	84.0	197.24	0.960
182	1127	B	22	X	3	84.0	197.24	0.952
182	1127	B	23	X	3	75.0	206.75	0.674
182	1127	B	23	X	3	75.0	206.75	0.646
182	1127	B	23	X	3	75.0	206.75	0.591

Note: Only a portion of this table appears here. The complete table is available in **ASCII format.**

Table T13. Discrete *P*-wave velocity from measurements using PWS1 and PWS2, Site 1127.

Leg	Site	Hole	Core	Type	Section	Interval (cm)	Depth (mbsf)	PWS 1 or 2	V_p (km/s)
182	1127	A	1	H	1	0.222	0.22	2	1.5625
182	1127	A	1	H	1	0.529	0.53	2	1.5653
182	1127	A	1	H	1	0.910	0.91	2	1.5738
182	1127	A	1	H	1	0.912	0.91	1	1.5739
182	1127	A	1	H	2	0.257	1.76	2	1.5569
182	1127	A	1	H	2	0.603	2.10	2	1.5738
182	1127	A	1	H	2	0.871	2.37	2	1.5597
182	1127	A	1	H	2	1.136	2.64	2	1.5653
182	1127	A	1	H	2	0.872	2.37	1	1.5710
182	1127	A	1	H	3	0.292	3.29	2	1.5695
182	1127	A	1	H	3	0.647	3.65	2	1.5611
182	1127	A	1	H	3	0.979	3.98	2	1.5681
182	1127	A	1	H	3	1.247	4.25	2	1.5583
182	1127	A	1	H	3	0.292	3.29	1	1.5739
182	1127	A	1	H	3	0.977	3.98	1	1.5710
182	1127	A	1	H	4	0.202	4.70	2	1.5639
182	1127	A	1	H	4	0.549	5.05	2	1.5667
182	1127	A	1	H	4	0.918	5.42	2	1.5528
182	1127	A	1	H	4	1.211	5.71	2	1.5555
182	1127	A	1	H	5	0.243	6.24	2	1.5583
182	1127	A	1	H	5	0.644	6.64	2	1.5569
182	1127	A	1	H	5	0.974	6.97	2	1.5431
182	1127	A	1	H	5	1.270	7.27	2	1.5528
182	1127	A	1	H	6	0.291	7.79	2	1.5667
182	1127	A	1	H	6	0.620	8.12	2	1.5431
182	1127	A	1	H	6	1.004	8.50	2	1.5404
182	1127	A	1	H	6	1.281	8.78	2	1.5514
182	1127	A	1	H	6	1.281	8.78	2	1.5514
182	1127	A	1	H	6	0.291	7.79	1	1.5717
182	1127	A	1	H	7	0.193	9.19	2	1.5852
182	1127	B	1	H	1	0.295	0.30	2	1.5653
182	1127	B	1	H	1	0.566	0.57	2	1.5781
182	1127	B	1	H	1	0.966	0.97	2	1.5710
182	1127	B	1	H	2	0.255	1.76	2	1.5766
182	1127	B	1	H	2	0.600	2.10	2	1.5738
182	1127	B	1	H	2	0.987	2.49	2	1.5653
182	1127	B	1	H	2	1.273	2.77	2	1.5710
182	1127	B	1	H	2	0.252	1.75	1	1.5760
182	1127	B	1	H	3	0.624	3.62	2	1.5695
182	1127	B	1	H	3	0.625	3.63	2	1.5738
182	1127	B	1	H	3	1.014	4.01	2	1.5681
182	1127	B	1	H	3	1.244	4.24	2	1.5710
182	1127	B	1	H	3	0.214	3.21	1	1.5760
182	1127	B	1	H	4	0.163	4.66	2	1.5639
182	1127	B	1	H	4	0.452	4.95	2	1.5695
182	1127	B	1	H	4	0.871	5.37	2	1.5583
182	1127	B	1	H	4	0.162	4.66	1	1.5703
182	1127	B	2	H	1	0.499	6.40	2	1.5769
182	1127	B	2	H	1	0.900	6.80	2	1.5794
182	1127	B	2	H	1	1.340	7.24	2	1.5745
182	1127	B	2	H	1	0.899	6.80	1	1.5759
182	1127	B	2	H	1	1.341	7.24	1	1.5660
182	1127	B	2	H	2	0.202	7.60	2	1.5638
182	1127	B	2	H	2	0.597	8.00	2	1.5891
182	1127	B	2	H	2	0.850	8.25	2	1.5915
182	1127	B	2	H	2	1.300	8.70	2	1.6243
182	1127	B	2	H	2	1.302	8.70	1	1.6470
182	1127	B	2	H	3	0.221	9.12	2	1.5997
182	1127	B	2	H	3	0.562	9.46	2	1.5959
182	1127	B	2	H	3	0.999	9.90	2	1.6545
182	1127	B	2	H	3	1.400	10.30	2	1.6890

Note: Only a portion of this table appears here. The complete table is available in **ASCII format.**

Table T14. Index properties measurements, Site 1127.

Leg	Site	Hole	Core	Type	Section	Top (cm)	Bottom (cm)	Depth (mbsf)	Bulk water content (%)	Dry water content (%)	Bulk density (g/cm³)	Dry density (g/cm³)	Grain density (g/cm³)	Porosity (%)	Void ratio
182	1127	B	1	H	1	89.0	91.0	0.89	40.2	67.3	1.62	0.97	2.68	63.8	1.76
182	1127	B	1	H	2	89.0	91.0	2.39	37.9	61.0	1.66	1.03	2.69	61.5	1.60
182	1127	B	1	H	3	89.0	91.0	3.89	38.1	61.6	1.66	1.03	2.68	61.8	1.62
182	1127	B	1	H	4	89.0	91.0	5.39	39.4	64.9	1.64	1.00	2.70	63.1	1.71
182	1127	B	2	H	1	59.0	61.0	6.49	37.4	59.7	1.67	1.05	2.67	60.9	1.56
182	1127	B	2	H	2	89.0	90.0	8.29	36.7	58.1	1.68	1.06	2.68	60.3	1.52
182	1127	B	2	H	3	89.0	91.0	9.79	32.9	49.0	1.76	1.18	2.73	56.6	1.30
182	1127	B	2	H	4	89.0	91.0	11.29	32.5	48.1	1.77	1.19	2.71	55.9	1.27
182	1127	B	2	H	5	79.0	81.0	12.69	30.7	44.3	1.80	1.25	2.71	54.0	1.17
182	1127	B	2	H	6	89.0	91.0	14.29	32.2	47.4	1.76	1.20	2.69	55.4	1.24
182	1127	B	2	H	7	28.0	30.0	15.18	31.5	46.0	1.78	1.22	2.69	54.7	1.21
182	1127	B	3	H	1	89.0	91.0	16.29	34.7	53.0	1.72	1.13	2.70	58.3	1.40
182	1127	B	3	H	2	89.0	91.0	17.79	35.6	55.2	1.71	1.10	2.71	59.4	1.46
182	1127	B	3	H	3	89.0	91.0	19.29	34.1	51.8	1.73	1.14	2.68	57.5	1.35
182	1127	B	3	H	4	89.0	91.0	20.79	32.6	48.3	1.76	1.19	2.69	55.9	1.27
182	1127	B	3	H	5	80.0	82.0	22.20	32.9	49.1	1.75	1.17	2.67	56.1	1.28
182	1127	B	3	H	6	20.0	22.0	22.70	33.5	50.3	1.74	1.16	2.68	56.8	1.32
182	1127	B	4	H	1	94.0	96.0	25.84	33.1	49.6	1.75	1.17	2.68	56.5	1.30
182	1127	B	4	H	3	90.0	92.0	27.73	33.6	50.6	1.73	1.15	2.65	56.7	1.31
182	1127	B	4	H	4	89.0	91.0	29.22	34.7	53.1	1.72	1.13	2.70	58.4	1.40
182	1127	B	4	H	6	93.0	95.0	32.26	33.2	49.6	1.74	1.17	2.68	56.5	1.30
182	1127	B	5	H	2	69.0	71.0	36.59	31.5	46.0	1.78	1.22	2.69	54.7	1.21
182	1127	B	5	H	3	69.0	71.0	38.09	33.2	49.6	1.76	1.18	2.74	57.0	1.33
182	1127	B	5	H	4	69.0	71.0	39.59	32.2	47.6	1.76	1.19	2.66	55.3	1.24
182	1127	B	5	H	5	69.0	71.0	41.09	32.3	47.6	1.76	1.19	2.69	55.6	1.25
182	1127	B	5	H	6	69.0	71.0	42.59	33.3	49.9	1.73	1.16	2.65	56.3	1.29
182	1127	B	5	H	7	20.0	22.0	43.10	32.0	47.0	1.77	1.20	2.69	55.3	1.24
182	1127	B	7	H	2	119.0	121.0	56.09	32.6	48.4	2.01	1.36	3.78	64.1	1.79
182	1127	B	7	H	3	69.0	71.0	57.09	31.5	46.1	1.77	1.21	2.65	54.4	1.19
182	1127	B	7	H	5	102.0	104.0	60.42	31.2	45.4	1.77	1.22	2.65	54.0	1.18
182	1127	B	7	H	6	49.0	51.0	61.39	31.9	46.7	1.76	1.20	2.64	54.6	1.20
182	1127	B	8	H	1	89.0	91.0	63.79	30.2	43.3	1.79	1.25	2.64	52.8	1.12
182	1127	B	8	H	3	89.0	91.0	66.79	31.8	46.7	1.77	1.21	2.68	54.9	1.22
182	1127	B	8	H	5	89.0	91.0	69.79	31.4	45.8	1.76	1.21	2.63	54.0	1.18
182	1127	B	9	H	1	89.0	91.0	73.29	31.5	45.9	1.78	1.22	2.71	54.8	1.21
182	1127	B	9	H	2	89.0	91.0	74.79	31.3	45.6	1.78	1.22	2.69	54.5	1.20
182	1127	B	9	H	3	89.0	91.0	76.29	31.4	45.8	1.77	1.22	2.67	54.4	1.19
182	1127	B	9	H	4	92.0	94.0	77.82	31.8	46.6	1.76	1.20	2.64	54.6	1.20
182	1127	B	10	H	2	89.0	91.0	83.18	31.2	45.4	1.78	1.22	2.67	54.2	1.18
182	1127	B	10	H	4	89.0	91.0	86.18	30.6	44.1	1.78	1.24	2.65	53.2	1.14
182	1127	B	10	H	6	89.0	91.0	89.18	31.7	46.4	1.76	1.20	2.65	54.6	1.20
182	1127	B	11	H	2	89.0	91.0	93.79	30.9	44.6	1.78	1.23	2.65	53.6	1.15
182	1127	B	11	H	4	89.0	91.0	96.79	29.7	42.2	1.80	1.27	2.65	52.2	1.09
182	1127	B	11	H	6	69.0	71.0	99.43	30.5	43.8	1.79	1.24	2.65	53.2	1.14
182	1127	B	12	H	1	59.0	61.0	101.49	29.5	41.7	1.81	1.28	2.67	52.1	1.09
182	1127	B	12	H	2	59.0	61.0	102.23	30.3	43.4	1.81	1.26	2.70	53.4	1.15
182	1127	B	12	H	3	59.0	61.0	103.73	30.7	44.4	1.79	1.24	2.68	53.8	1.16
182	1127	B	12	H	4	59.0	61.0	105.23	29.6	42.0	1.81	1.27	2.67	52.2	1.09
182	1127	B	12	H	5	59.0	61.0	106.73	30.5	43.9	1.79	1.24	2.66	53.3	1.14
182	1127	B	12	H	6	59.0	61.0	108.13	30.6	44.1	1.78	1.24	2.65	53.2	1.14
182	1127	B	12	H	7	29.0	31.0	108.88	30.6	44.0	1.78	1.23	2.63	53.0	1.13
182	1127	B	13	H	6	19.0	21.0	117.71	26.9	36.8	1.87	1.37	2.68	49.1	0.96
182	1127	B	14	H	1	19.0	21.0	120.09	33.9	51.3	1.74	1.15	2.73	57.8	1.37
182	1127	B	14	H	2	19.0	21.0	120.74	29.5	41.8	1.81	1.28	2.67	52.1	1.09
182	1127	B	14	H	3	19.0	21.0	122.24	31.3	45.6	1.78	1.22	2.68	54.4	1.19
182	1127	B	14	H	4	19.0	21.0	123.74	32.3	47.7	1.76	1.19	2.66	55.4	1.24
182	1127	B	14	H	5	19.0	21.0	125.24	28.4	39.6	1.83	1.31	2.66	50.7	1.03
182	1127	B	14	H	6	19.0	21.0	126.74	27.7	38.3	1.91	1.38	2.86	51.7	1.07
182	1127	B	16	H	1	47.0	49.0	139.37	30.3	43.4	1.79	1.25	2.66	53.0	1.13
182	1127	B	16	H	2	49.0	51.0	140.89	30.0	42.8	1.81	1.27	2.69	52.9	1.13
182	1127	B	16	H	3	54.0	56.0	142.44	29.3	41.4	1.82	1.29	2.68	52.0	1.09
182	1127	B	16	H	4	50.0	52.0	143.90	28.0	38.9	1.84	1.33	2.67	50.4	1.01
182	1127	B	17	X	1	69.0	71.0	149.09	28.5	39.8	1.83	1.31	2.66	50.9	1.04
182	1127	B	17	X	2	69.0	71.0	150.59	28.1	39.0	1.84	1.32	2.67	50.4	1.02
182	1127	B	17	X	3	69.0	71.0	152.09	34.4	52.3	1.73	1.13	2.70	58.0	1.38

Note: Only a portion of this table appears here. The complete table is available in **ASCII format.**

Table T15. Undrained shear strength measurements, Site 1127.

Leg	Site	Hole	Core	Type	Section	Interval (cm)	Depth (mbsf)	Maximum shear strength (kPa)	Peak (kPa)
182	1127	B	1	H	2	115.1	2.65	7.92	9.66
182	1127	B	1	H	3	114.8	4.15	11.88	14.49
182	1127	B	2	H	1	114.9	7.05	15.84	19.32
182	1127	B	2	H	2	105.1	8.45	13.14	16.03
182	1127	B	2	H	2	9.9	7.50	25.20	30.74
182	1127	B	2	H	3	120.1	10.10	7.74	9.44
182	1127	B	2	H	4	119.0	11.59	10.44	12.73
182	1127	B	2	H	5	110.2	13.00	13.23	16.14
182	1127	B	2	H	6	109.9	14.50	5.13	6.26
182	1127	B	3	H	1	94.9	16.35	10.17	12.40
182	1127	B	3	H	2	99.9	17.90	6.21	7.57
182	1127	B	3	H	3	100.0	19.40	9.63	11.75
182	1127	B	3	H	4	100.3	20.90	12.87	15.70
182	1127	B	3	H	5	63.1	22.03	16.47	20.09
182	1127	B	3	H	6	23.1	22.73	25.20	30.74
182	1127	B	4	H	1	100.1	25.90	7.92	9.66
182	1127	B	4	H	3	110.1	27.93	20.16	24.59
182	1127	B	4	H	4	105.3	29.38	11.61	14.16
182	1127	B	4	H	5	95.0	30.78	12.33	15.04
182	1127	B	4	H	7	64.1	33.47	9.09	11.09
182	1127	B	4	H	8	33.2	34.16	7.02	8.56
182	1127	B	5	H	1	109.9	35.50	5.31	6.48
182	1127	B	5	H	2	100.1	36.90	8.10	9.88
182	1127	B	5	H	4	100.2	39.90	13.05	15.92
182	1127	B	5	H	4	101.0	39.91	8.55	10.43
182	1127	B	5	H	5	114.9	41.55	6.93	8.45
182	1127	B	5	H	6	70.0	42.60	7.83	9.55
182	1127	B	5	H	7	28.1	43.18	12.60	15.37
182	1127	B	6	H	1	112.8	45.03	8.46	10.32
182	1127	B	6	H	2	111.0	46.51	12.51	15.26
182	1127	B	6	H	4	113.0	49.53	12.51	15.26
182	1127	B	6	H	4	109.9	49.50	10.89	13.28
182	1127	B	6	H	5	107.8	50.98	11.79	14.38
182	1127	B	6	H	6	117.2	52.57	7.83	9.55
182	1127	B	7	H	1	122.3	54.62	7.56	9.22
182	1127	B	7	H	2	93.3	55.83	8.55	10.43
182	1127	B	7	H	3	108.9	57.49	15.57	18.99
182	1127	B	7	H	4	132.5	59.22	12.15	14.82
182	1127	B	8	H	1	113.4	64.03	21.87	26.67
182	1127	B	8	H	2	132.6	65.73	9.00	10.98
182	1127	B	8	H	3	105.2	66.95	7.47	9.11
182	1127	B	8	H	4	130.3	68.70	16.56	20.20
182	1127	B	9	H	1	136.8	73.77	11.25	13.72
182	1127	B	9	H	2	130.7	75.21	7.38	9.00
182	1127	B	9	H	5	125.6	79.59	24.84	30.30
182	1127	B	9	H	5	128.9	79.62	17.91	21.84
182	1127	B	10	H	2	132.1	83.61	21.96	26.78
182	1127	B	10	H	4	110.0	86.39	13.41	16.36
182	1127	B	10	H	5	124.1	88.03	29.25	35.67
182	1127	B	10	H	6	125.1	89.54	20.61	25.14
182	1127	B	11	H	2	137.7	94.28	16.83	20.53
182	1127	B	11	H	3	122.5	95.63	26.37	32.16
182	1127	B	11	H	4	122.2	97.12	9.81	11.97
182	1127	B	11	H	6	61.7	99.36	20.52	25.03
182	1127	B	12	H	2	126.4	102.90	6.66	8.12
182	1127	B	12	H	3	109.6	104.24	9.09	11.09
182	1127	B	12	H	4	133.4	105.97	12.33	15.04
182	1127	B	12	H	6	88.8	108.43	10.17	12.40
182	1127	B	13	H	1	110.0	111.50	18.36	22.39
182	1127	B	13	H	2	100.0	112.90	20.61	25.14
182	1127	B	13	H	3	76.8	114.17	34.38	41.93
182	1127	B	13	H	4	70.7	115.54	40.86	49.83
182	1127	B	13	H	5	92.9	117.05	26.73	32.60

Note: Only a portion of this table appears here. The complete table is available in **ASCII format.**

Table T16. Summary of tool strings, intervals logged, and logging speeds, Hole 1127B.

	First pass		Second pass	
Tool string	Interval (mbsf)	Speed (m/hr)	Interval (mbsf)	Speed (m/hr)
Triple combo/LDEO-TAP	0-510.7 (QC)	945	510.7-0 (main)	550
FMS/sonic	512.6-100 (R)	275	512.6-0 (main)	275

Note: LDEO-TAP = Lamont-Doherty Earth Observatory temperature/acceleration/pressure tool, QC = quality control run, main = main logging run, FMS = Formation MicroScanner, R = repeat logging run.

Table T17. Differences between depths to seismic horizons and corrected depths.

Seismic horizons	Site 1127			Site 1129			Site 1131		
	Predicted intersection (mbsf)	ITT corrected depth (mbsf)	Difference (m)	Predicted intersection (mbsf)	Check-shot corrected depth (mbsf)	Difference (m)	Predicted intersection (mbsf)	Check-shot corrected depth (mbsf)	Difference (m)
Sequence 2, Horizon A	228	242	+14	133	143	+10	134	149	+15
Sequence 2, Horizon B	362	380	+18	271	283	+12	333	345	+12
Sequence 2, Horizon C	410	432	+22	403	410	+7	471	483	+12
Base of Sequence 2	452	476	+24	510	517	+7	521	529	+8
Base of Sequence 3	558			605			576	585	+9

Notes: Predicted intersection depths were derived using high-resolution site-survey seismic data stacking velocities. Corrected depths were based on check-shot data and interval transit-time (ITT) data.